Review

Structural optimization of carbon-based diatomic catalysts towards advanced electrocatalysis

Tianmi Tang, Zhenlu Wang, Jingqi Guan [*]

Institute of Physical Chemistry, College of Chemistry, Jilin University, 2519 Jiefang Road, Changchun 130021, PR China

ARTICLE INFO

ABSTRACT

As an extension of single-atom catalysts (SACs), diatomic catalysts (DACs) perfectly inherit the advantages of SACs but break some theoretical limitations of SACs due to the interaction between dual-atom sites. However, there are still challenges for the electrocatalytic applications of carbon-based DACs, such as difficult in controllable synthesis and identification of bimetallic dimer, hard to adjust the coordination environments of bimetallic sites, poor structural stability, and unclear reaction mechanisms. Here, we summarize controllable synthesis methods for the fabrication of DACs and introduce the characterization techniques in comprehending the geometrical configuration of bimetallic dimer, local electronic structure, coordination environments, and insights into reaction mechanisms by combining in situ characterization and theoretical investigation. Moreover, several important electrocatalytic applications of DACs, including for the hydrogen evolution reaction, oxygen evolution reaction, oxygen reduction reaction, CO_2 reduction reaction, and nitrogen reduction reaction are reviewed. To precipitate the future development of high-performance carbon-based DACs, we put forward several strategies to adjust the electronic structure for optimizing the electrocatalytic performances, including adjusting the electronic structure of bimetallic central atoms, regulating the local coordination environment of bimetallic central atoms, and tuning the base environment. Finally, future research directions of developing advanced carbon-based DACs for electrocatalytic application are proposed.

1. Introduction

With the development of industry and the increase of global population, the world is now standing at the crossroads of energy and a series of environmental pollution problems [1-4]. Therefore, it is an irresistible trend to explore and develop renewable energy storage and conversion technologies to replace fossil fuels with sustainable clean energy. Fuel cells, electrolytic cells and metal-air cells, CO_2 and N_2 fixation devices rely on electrocatalytic reactions such as hydrogen evolution reaction (HER), oxygen evolution reaction (OER), oxygen reduction reaction (ORR), carbon dioxide reduction reaction (CO_2RR) and nitrogen reduction reaction (NRR). Electrocatalysts are the core components of electrode materials in these devices [5-11]. At present, almost all commercial electrocatalysts are mainly precious metal materials (such as Pt, IrO_2, RuO_2, etc.) to reduce the overpotentials and accelerate the reactions, but the high price of precious metals, scarce resources and poor durability and other shortcomings seriously affect the development of energy storage and conversion devices [12-17]. Designing cheap, efficient and durable electrocatalysts is therefore central to the large-scale

use of such devices.

Single-atom catalysts (SACs) have been a hot topic in the field of heterogeneous catalysis in recent years. They have been intensively studied because of their 100% atom utilization rate, high selectivity and excellent catalytic activity [18-20]. Since there is a linear relationship between isolated single metal active sites in SACs and the catalytic reaction, it is difficult to achieve the optimal adsorption state of multiple reaction intermediates, which affects the selectivity of products. In addition, to maintain the single-atom configuration and avoid metal agglomeration, the loading capacity of metal species and the density of active sites are usually low, resulting in low catalytic activity. The interaction between single metal atoms and the carrier is relatively weak, resulting in the instability of the single-atom structure [21-23]. These defects of SACs limit their applications in catalytic fields. Subsequently, the further extension of SACs to diatomic catalysts (DACs) has attracted a lot of researchers. The DACs can effectively break through the aforementioned defects due to the interaction between diatomic metal sites. Different active sites provide rich adsorption modes for the reaction intermediates. The adjustment of electronic structure can

* Corresponding author.
  E-mail address: guanjq@jlu.edu.cn (J. Guan).

effectively adjust the adsorption energy and break through the linear relationship between the DACs and the catalytic reaction. In addition, diatomic catalysts can achieve high loads and provide more effective active sites. The introduced second metal can be the same metal or different metals to obtain homonuclear diatomic catalyst or heteronuclear diatomic catalyst. The most prominent characteristics of diatomic catalyst are the synergistic effect, distance enhancement effect and electron effect between diatoms. Diatomic catalysts not only exhibit the function of two single atoms, but also can effectively regulate the electronic structure of the active site, and improve the catalytic performance, which can be applied in many catalytic fields [24,25].

In diatomic catalysts, the distance between two metal atoms is very close, generally between 2 ~ 4 Å, and a strict coordination structure can be formed between them [26]. The active center coordination structure of this kind of diatomic catalyst has symmetry in space and distance. The other kind of two metal atoms in the adjacent position does not have symmetry, and the two metal coordination number is different [9,27-29]. As a new type of catalyst, active center regulation can effectively reduce reaction activation energy and improve catalytic activity [30]. As an important branch of diatomic catalysts, carbon-based diatomic catalysts are widely used in the field of electrocatalysis. Carbon-based diatomic catalysts with unique electronic structure and geometric configuration can be constructed because carbon-based materials have high conductivity, large specific surface area and modifiability. In 1980, Anson et al. synthesized a series of dimeric metal porphyrins, which showed that the four-atom brid-linked double cobalt surface porphyrins reduced oxygen to water, and demonstrated that the two metal centers were involved in the multi-electron control process [31]. Strasser et al. used chemical adsorption/desorption and ^{57}Fe Mössbauer spectroscopy techniques to quantitatively analyze the volume and surface active site density of single/bimetallic Fe/N doped carbon, and the related turnover frequency, showing that bimetallic (Fe, Mn)-N-C can effectively catalyze ORR [32]. On this basis, more and more researches have been conducted on diatomic catalysts in recent years. Sun et al. synthesized a nitrogen-doped carbon support diatomic catalyst (Zn/CoN-C) with Zn-Co atomic pair structure by using a competitive complexing strategy. In the Zn/CoN-C catalyst, the electronic structure of the active site is regulated by the co-coordination of Zn and Co with N. The O-O bond was extended from 1.23 Å to 1.432 Å after adsorption of O_2 at this site, which reduced the dissociation energy barrier and increased the catalytic activity of ORR [33]. In diatomic catalysts, the synergistic effect comes from the hybrid coupling of electron orbitals with each other or the spatial position effect between two metal atoms. The synergistic effect between two sites can adjust the local electronic structure, optimize the adsorption/desorption energy of reaction intermediates, reduce the reaction energy barrier, accelerate electron transfer, and optimize the hybrid of electron orbitals between two metal atoms, thus lowering the energy barrier of the rate-determining step [34-36].

In this review, we mainly introduced the synthesis methods and characterization techniques of diatomic catalysts and focused on the regulation strategies of diatomic catalysts. By regulating the central metal atoms of diatomic catalysts, homonuclear and heteronuclear diatomic catalysts were formed, and the coordination environment of the base plane and central metal atoms of diatomic catalysts was regulated, thus promoting electrocatalytic HER, OER, ORR, CO_2RR and NRR. In addition, the key factors to improve the catalytic performance of diatomic catalysts were proposed. Finally, the existing limitations of diatomic catalysts were analyzed, and the future development direction of diatomic catalysts was prospected.

2. Synthesis of diatomic catalysts

As an extension of single-atom catalyst, diatomic catalyst has attracted wide attention due to its high metal loading capacity and synergistic interaction between metals in addition to the 100% atomic utilization ratio, strong interaction with substrate and abundant surface

sites. However, due to the tendency of aggregation of metal atoms in the process of bimetallic catalyst synthesis or subsequent processing, the key to prepare highly dispersed diatomic catalysts is to prevent the aggregation of atoms and enhance the interaction between metal atoms and support. The synthesis methods reported so far mainly include atomic layer deposition (ALD), high temperature pyrolysis, hydrothermal synthesis, and wet chemistry.

ALD is a technique that gas phase precursors pass alternately into the reactor and chemically adsorb and react on the deposition substrate to form a deposition film. When the precursors reach the surface of the substrate, they will chemically adsorb and react on the surface. The ALD reactor needs to be cleaned with inert gas between the precursor pulses. It can be seen that whether the precursor material can chemically adsorb on the surface of the deposited material is the key to achieve ALD [37-39]. The surface reaction of ALD is self-limiting, and repeated over and over again to form the desired film [40]. The advantages of this synthesis method include precise control of layer thickness. Homogeneous and conformal films can be obtained, which could penetrate porous materials with high surface area and have surface chemical selectivity. However, the synthesis of diatomic catalyst using ALD technology is usually carried out at high temperature, which would lead to catalyst sintering [41-44].

High temperature pyrolysis is the most common method for preparing diatomic catalysts. The target diatomic catalyst is generally obtained by pyrolysis of suitable precursors in the atmosphere of NH_3, N_2 or Ar at high temperature. Under the condition of high temperature, the metal atoms can form covalent bonds with the support, promoting the combination between the metal and the support, and improving the stability of the catalyst. Metal Organic Frameworks (MOFs) are common precursors for the synthesis of diatomic catalysts by pyrolysis method. In the process of high temperature pyrolysis, organic carbon can be converted into graphitized carbon, while nitrogen, sulfur or oxygen in MOFs can form coordination with metal to stabilize metal atoms. In addition, MOF materials have uniformly distributed metal nodes and skeleton, which can effectively avoid the agglomeration of metal atoms. The most typical one is that the N element in MOFs can form very stable M−N coordination bonds with metal ions, which effectively improves the thermal and chemical stability of diatomic catalysts. Therefore, it is widely used to synthesize diatomic catalysts because of its simplicity and low cost [8,45-47].

Hydrothermal synthesis refers to the synthesis method that takes water or organic solution as the reaction medium under the conditions of 80 ~ 1000 °C and 1 MPa ~ 1 GPa [48]. In subcritical and supercritical hydrothermal conditions, hydrothermal reactions can be used to replace some high-temperature solid reactions because the reaction is carried out at the molecular level, which can improve reactivity. At present, many new synthesis routes have been developed for hydrothermal synthesis, such as direct method, guide agent method, template method, complexing agent method, organic solvent method, microwave method and high temperature and high-pressure synthesis technology. Wet chemical method includes chemical liquid deposition method, electrochemical deposition method, and sol–gel method, where chemical reactions take place in the liquid phase. Wet chemistry method is often used to prepare metal-anchored single-atom catalysts with low metal loading to reduce the chance of metal agglomeration. In addition, the support should be rich in oxygen-containing functional groups, which is conducive to metal anchoring [49]. However, in the synthesis of carbon-based DACs, two or several synthesis techniques are often used, and the following chapter will be introduced from bottom-up and top-down two categories.

2.1. Bottom-up method

Bottom-up synthesis technique refers to the method in which the precursors of binuclear metal complexes are adsorbed, reduced, and confined in vacancy to form diatomic structure. Hu et al. prepared PtNi

diatomically anchored nitrogen-doped carbon-based catalysts (PtNi-NC) using atomic layer deposition technique. The PtNi-NC catalyst showed excellent HER activity with a low overpotential (η_{10} = 30 mV) in acidic media [50]. Sun et al. synthesized a Pt-Ru dimer catalyst with A-B bimetallic dimer structure using ALD technology, in which Pt-Ru bonding configuration was found (Fig. 1a). The hydrogen evolution activity of Pt-Ru dimer is much higher than that of commercial Pt/C catalysts and is quite stable during electrocatalysis [28]. Fan et al. formed W source and Mo source into a pair of W-Mo species by hydrothermal treatment, which were anchored in partially reduced graphene oxide (p-RGO), freeze-dried, and then treated in NH_3/Ar gas at 800 °C to obtain W_1Mo_1-NG DAC. The catalyst showed excellent HER activity [51]. Liu et al. mixed copper phthalocyanine (CuPc) and manganese phthalocyanine (MnPc) together with nitrogen and sulfur co-doped carbon materials by ball mill. After pyrolyzing and etching, a diatomic catalyst (Cu,Mn)/NSC was obtained. (Cu,Mn)/NSC showed excellent catalytic activity in oxygen reduction, and the half-wave potentials ($E_{1/2}$) in alkaline and acidic media were 0.93 V and 0.78 V, respectively [52]. Zhang et al. synthesized a hetero-paired atomic-site catalyst (Ni/Fe − N/O − C) by a wet chemistry method, where carbon black was activated, Ni^{2+} and Fe^{2+} were captured and adsorbed, and metal ions were then fixed to carbon support through pyrolysis and acid leaching (Fig. 1b). Ni/Fe − N/O − C exhibited better stability than mono-metal catalysts and showed CO selectivity of more than 80% over a wide potential range (−1.4 ~ − 1.7 V) for the CO_2RR [53]. Lu et al. took a binuclear Ni complex as the precursor and used an in-situ synthesis strategy to anchor Ni_2 pairs uniformly on nitrogen-doped carbon

nanotubes. The binuclear Ni complex precursor could effectively fix the Ni_2 diatomic sites after pyrolysis, and the uniformly distributed diatomic Ni_2 catalyst (Ni_2-NCNT) was synthesized by this strategy in a controllable manner (Fig. 1c). Ni_2-NCNT showed excellent catalytic activity, selectivity and stability in the reduction of CO_2 to CO, and the partial current density of CO production could reach 76 mA cm^{-2} [54]. Zhou et al. successfully prepared a diatomic Ag_2/graphene (Ag_2-G) catalyst. In the preparation, π-π interaction was used to adsorb the binuclear molecules with aromatic hydrocarbons to graphene, which was then pyrolyzed at programmed temperature. During the pyrolysis process, the aromatic groups were graphitized. The catalyst can reduce CO_2 to CO at high potential (-0.25 V), and the Faraday efficiency (FE) reached 93.4% [55]. Wang et al. prepared a diatomic palladium catalyst (Pd_2 DAC) by anion replacement deposition precipitation method. The catalyst showed excellent CO_2RR activity, with FE_{CO} up to 98.2%, much better than Pd_1 SAC, and maintained good stability [56]. Yao et al. successfully synthesized a well-defined and homogeneous binuclear Ni catalyst. To protect diatomic Ni during the synthesis process, organic bisphosphine ligand modified diatomic $Ni_2(dppm)_2Cl_3$ clusters were designed. Subsequently, $Ni_2(dppm)_2Cl_3$ clusters were immersed into porous carbon derived from zeolite imidazolate framework (ZIF). The organophosphorus ligands were then removed by pyrolysis, and a nitrogen-doped carbon-based binuclear nickel catalyst (Ni_2/NC) was obtained. The catalyst showed excellent CO_2RR performance and FE_{CO} was up to 94.3% [57]. By using bottom-up strategy to prepare diatomic catalysts, it is generally necessary to synthesize the precursors of binuclear complexes with precise structure and control the pyrolysis temperature,
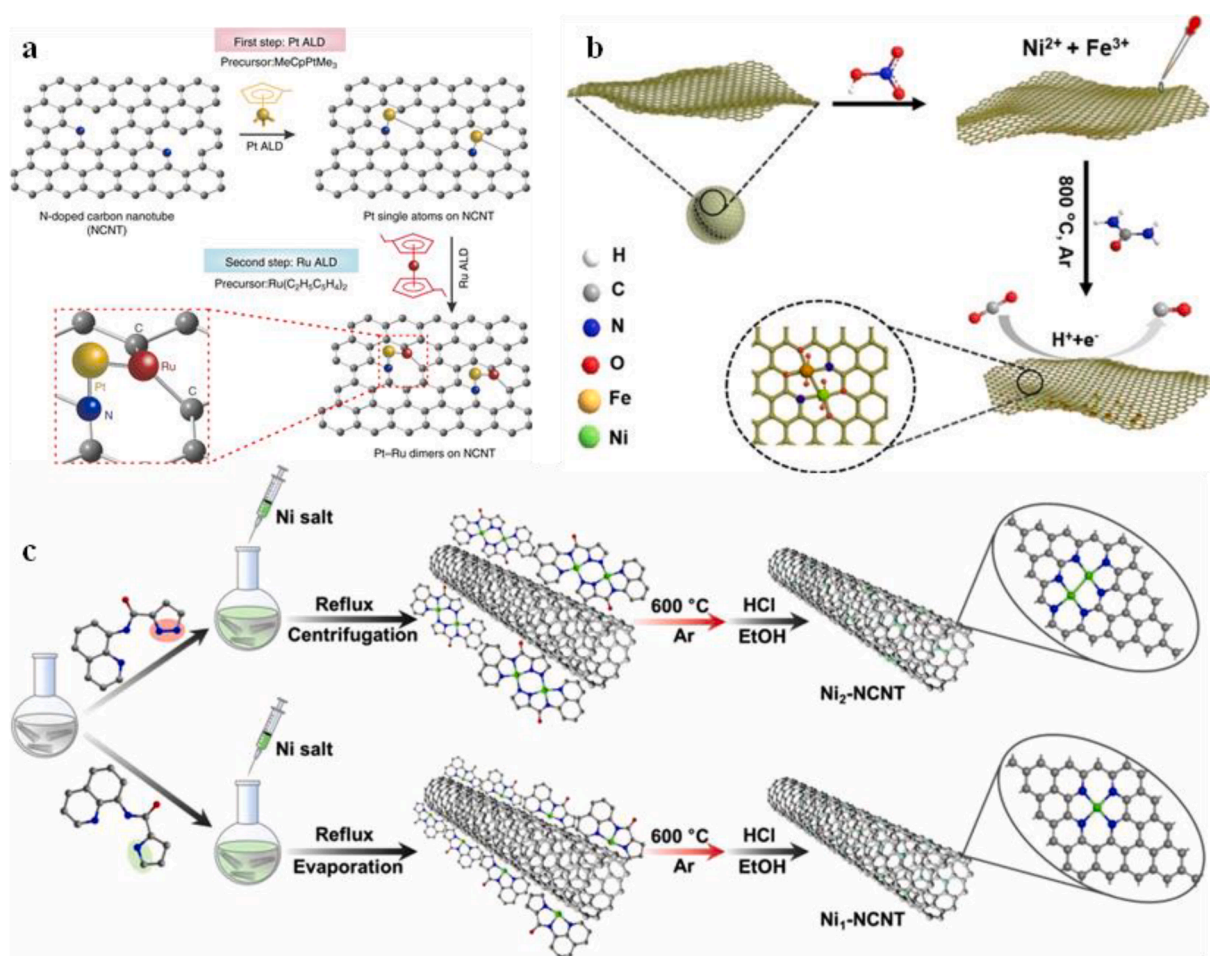

Fig. 1. (a) Synthetic illustration of Pt–Ru dimers on N-doped carbon nanotubes by ALD. (b) Synthetic illustration of dual-atom M − N/O − C catalysts. (c) Synthetic illustration of Ni_2-NCNT DAC and Ni-NCNT SAC. (a) Reproduced with permission.[28] Copyright 2021, Nature Portfolio. (b) Reproduced with permission.[53] Copyright 2021, Wiley-VCH Verlag GmbH & Co. KGaA. (c) Reproduced with permission.[54] Copyright 2022, Elsevier B.V.

which can obtain diatomic catalysts and effectively avoid metal agglomeration.

2.2. Top-down method

In top-down synthesis technology, massive metal or metal nanoparticles are used as a precursor, then metal bonds are broken, and atomically dispersed metal dimers are anchored on the substrate to form diatomic catalysts. Generally, this method involves high temperature pyrolysis. Carbon-based pore structure with large specific surface area provides an ideal substrate for diatomic loading, which has sufficient reaction sites and can fully improve the reactant transfer efficiency. In addition, carbon material, as a conductive material, can reduce the impedance of the system and improve the transmission efficiency of electrons, to improve the adsorption of reactants and promote the smooth progress of catalytic reactions. Shi et al. prepared a novel N-bridge Fe-Cu diatomic carbon nanocages (Fe, Cu DAs-NC) electrocatalyst using a synergistic multi-step strategy of cavity restriction-pore extension-oriented deposition. In this strategy, the steric hindrance effect can prevent metal ion aggregation during thermal decomposition. Under alkaline and acidic conditions, Fe, Cu DAs-NC showed enhanced ORR catalytic activity, and the $E_{1/2}$ was 0.94 V and 0.80 V, respectively [58]. Zheng et al. prepared an atomically dispersed ZnN_4 and CoN_4 co-supported nitrogen-doped carbon catalyst (ZnCo-NC-II) using a two-step strategy of cavity confinement and post-adsorption using a MOF engineering. ZnCo-NC-II showed obvious ORR activity in alkaline and acidic media with $E_{1/2}$ of 0.86 and 0.79 V, respectively [59]. Zheng et al. synthesized a FeCu-NC catalyst containing bimetallic CuN_4/FeN_4 sites using ZIF's surface restraint strategy. The $E_{1/2}$ of FeCu-NC in ORR reached 0.87 V [60]. Lee et al. synthesized a paired bimetallic atomic site catalyst in nitrogen-doped carbon using a packaging-substitution strategy (Fig. 2a). By regulating the d-orbital energy level, the catalytic ORR activity of Ru-Co diatomic catalyst was significantly higher than that of Ru-Fe and Ru-Ni diatomic catalysts. The $E_{1/2}$ and TOF were 0.895 V and 2.424 s^{-1}, respectively [61]. Cao et al. synthesized Mn-N-C by one-pot pyrolysis method, which was then adsorbed Fe and N sources by a two-solvent method. Fe-Mn-N-C material was finally obtained by pyrolysis (Fig. 2b), in which Fe-Mn was double-anchored to nitrogen-doped porous carbon (FeN_4-MnN_3). Fe-Mn-N-C exhibited excellent ORR activity with $E_{1/2}$ of 0.79 V and 0.93 V at acidic and alkaline conditions, respectively and ultra-low H_2O_2 yield [62]. Cao et al. oxidized and polymerized aniline in an aqueous solution of carbon black and Ni^{2+} to obtain the precursor Ni-PANI@C's, which was then pyrolyzed at 1000 °C to obtain Ni-N@C catalyst after pickling. The catalyst showed high selectivity and activity for reducing CO_2 to CO [63]. The spatial confinement method is a commonly used strategy in controlled synthesis. The diatomic precursors are encapsulated into porous materials, and then the atoms are uniformly dispersed on the carrier after pyrolysis. Niu et al. synthesized a series of homonuclear and heteronuclear diatomic catalysts using this method. Taking Fe-Cu diatomic catalyst as an example, the catalyst showed good ORR activity and stability [64]. By using this method, diatoms with clear structure, uniform dispersion and abundant coordination number can be obtained.
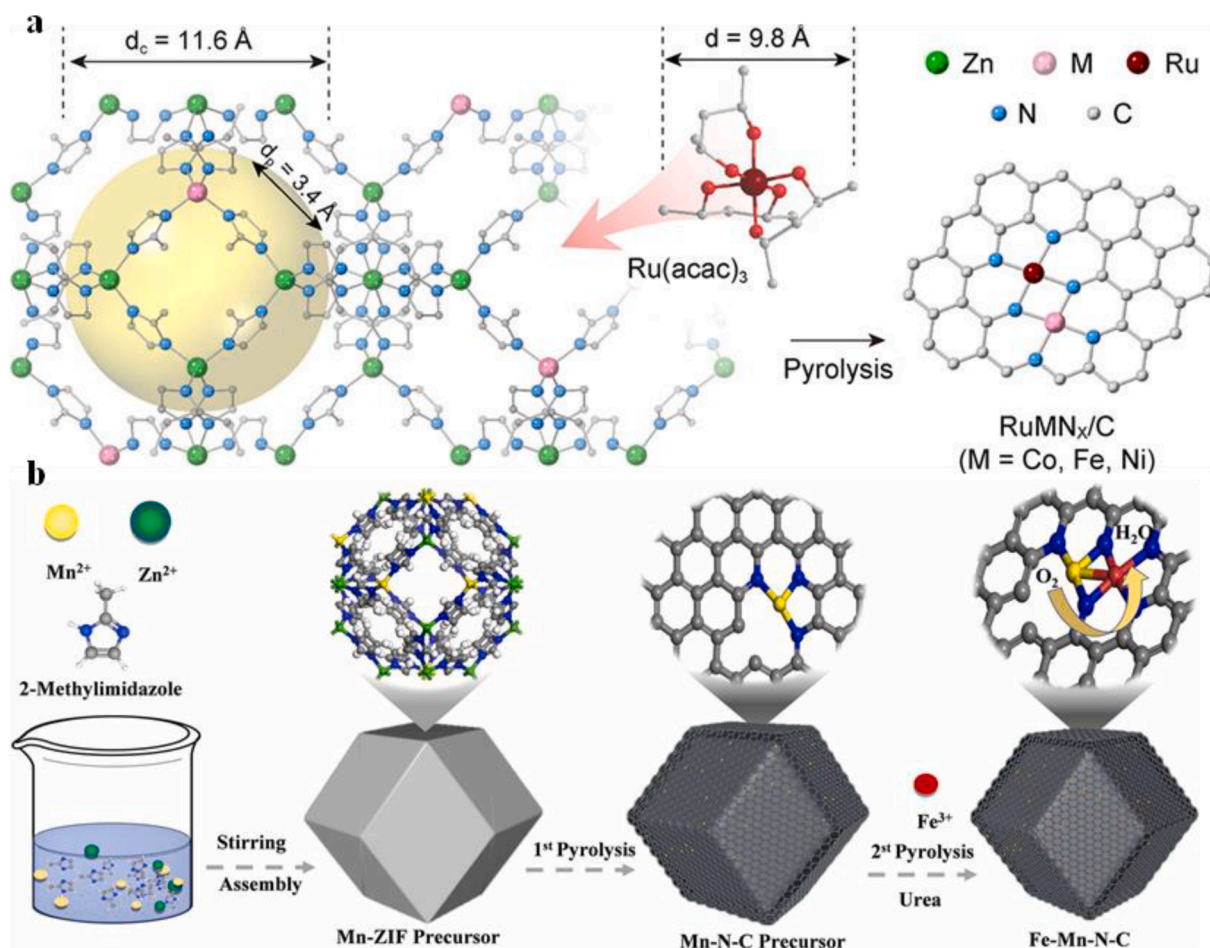

Fig. 2. (a) Synthetic illustration of $RuMN_x/C$. (b) Synthetic illustration of dual-atomic Fe-Mn-N-C.(a) Reproduced with permission.[61] Copyright 2022, American Chemical Society. (b) Reproduced with permission.[62] Copyright 2022, Elsevier B.V.

3. Characterization techniques of diatomic catalysts

At present, a large number of advanced instruments and characterization techniques have been developed, which provide great help to determine the structure of isolated metal atoms [65-67]. Methods used to characterize diatomic catalysts mainly include aberration-corrected high-angle annular dark field scanning transmission electron microscopy (HAADF-STEM), energy dispersive spectroscopy (EDS), electron energy loss spectroscopy (EELS) atomic spectra, X-ray absorption structure (XAS), X-ray photoelectron spectroscopy (XPS), Fourier transform infrared spectrum (FTIR) and Raman spectrum, and density functional theory (DFT). These characterization techniques can be used to obtain the local structure information of the atomic scale for further understanding diatomic catalysts. In this section we will focus on electron microscopy, XAS, in situ infrared spectrum, in situ Raman spectrum and DFT.

3.1. Electron microscope technology

Aberration-corrected scanning transmission electron microscopy (AC-STEM) is a characterization technique with atomic resolution, by which isolated atoms on a carrier can be directly observed. HAADF-STEM image presents different light and dark regions according to the difference of atomic number, and the spatial position and distribution information of metal atoms on the carrier can be observed. Combined with EELS and EDS, they are used for precise structural analysis and phase identification. Sun et al. prepared a bimetallic Pt-Ru dimer catalyst. The dimer structure was clearly observed according to different contrasts in the aberration-corrected HAADF-STEM, suggesting that the

dimer consisted of two elements (Fig. 3a-b) [28]. Qiao et al. synthesized uniformly dispersed NiCu DACs (NiCu-NC) on nitrogen-doped graphene. Uniformly dispersed bright spots of varying brightness on the carbon matrix were observed, which are smaller than 2 Å in size. In addition, EELS and EDS images also confirmed that nickel and copper elements were uniformly dispersed on the nitrogen-doped carbon matrix (Fig. 3c-f) [68].

3.2. XAS technology

X-ray absorption spectra have the advantages of high flux, and large and adjustable energy span, which can be used to obtain the average information of local atomic structure and chemical state of selected atomic species. XAS spectra have two main regions: X-ray absorption near-edge spectra (XANES) and extended X-ray absorption fine structure (EXAFS) spectra, through which the chemical valence, coordination environment and binding mode of individual atoms can be obtained. The XANES level is located at the edge of 50 to 1000 eV and is often used to detect the chemical states of atoms, while the EXAFS level is in the edge range of 50 eV and is often used to determine the coordination number, coordination distance, and coordination type of atoms. The existence of a single atom can be determined by combining morphological information and structural characteristics. In addition, EXAFS wavelet transform (WT) can be used to analyze the peaks with similar bond lengths in R space to obtain more reliable results. Wu et al. used XAS to understand the coordination environment of CoCu-DASC. In Fig. 3(g-k), the Co k-edge of CoCu-DASC was between Co foil and CoO, indicating that the chemical valence state of Co atom was between 0 and + 2, and the chemical valence state of Cu atom was also between 0 and
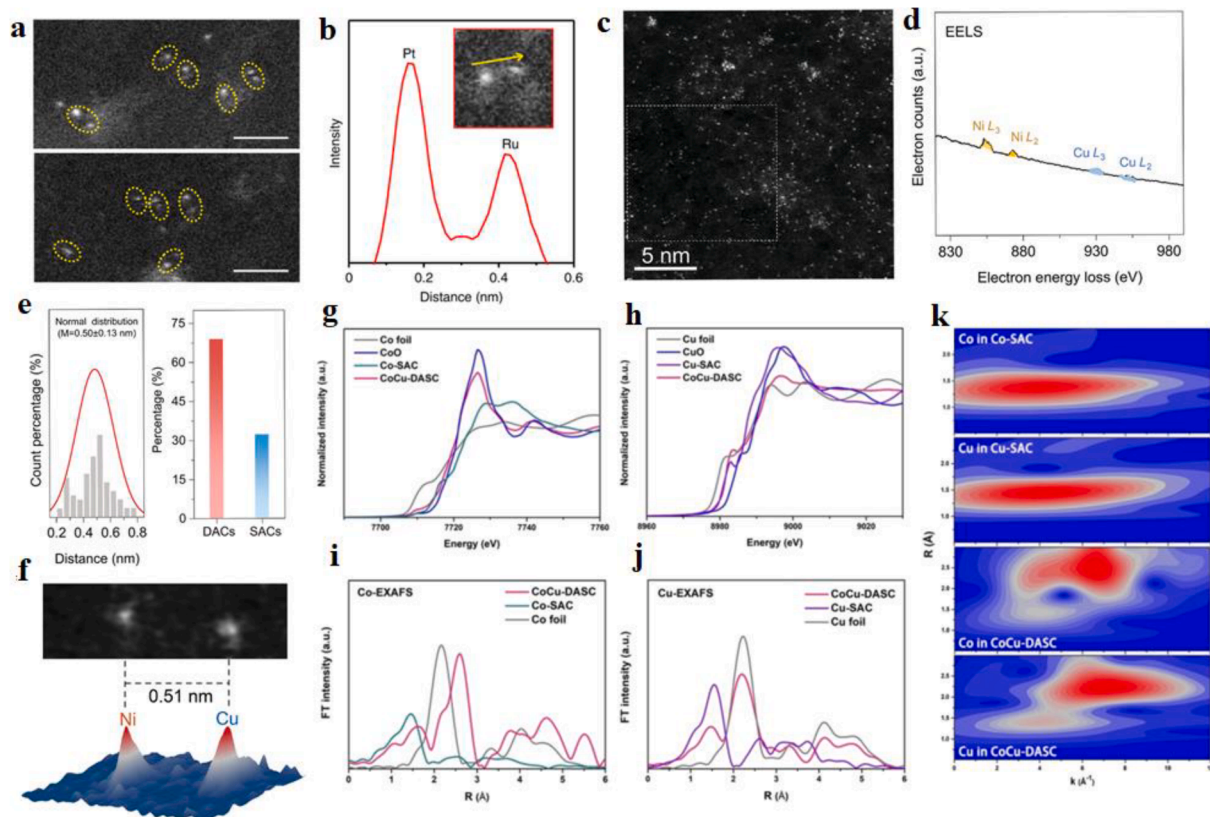

Fig. 3. (a) HAADF-STEM images of Pt–Ru dimers/NCNTs (bar: 1 nm). (b) The intensity profile obtained on one individual Pt–Ru dimer. (c) HAADF-STEM image and (d) EELS of NiCu-NC. (e) Histogram of the observed inter-metal distance and percentage. (f) Magnified HAADF-STEM image of a NiCu atomic pair and the corresponding 3D intensity profile. (g, h) Normalized Co and Cu K-edge XANES spectra. (i, j) FT-EXAFS spectra. (k) Wavelet transforms for the k²-weighted EXAFS signals. (a) Reproduced with permission.[28] Copyright 2021, Nature Portfolio. (c-f) Reproduced with permission.[68] Copyright 2022, Walter de Gruyter GmbH. (g-k) Reproduced with permission.[69] Copyright 2022, Wiley-VCH Verlag GmbH & Co. KGaA.

+ 2. In the Co EXAFS spectra, the peaks were observed at 1.45 Å and 2.57 Å, corresponding to the Co-N and Co-Cu bonds respectively. In the Cu EXAFS spectra, the Cu-N and Cu-Co bonds were observed at 1.47 Å and 2.20 Å, indicating that an atomic pair structure was formed between Co and Cu. EXAFS WT analysis further demonstrated that Co and Cu atoms were anchored onto conducting carbon in an atomically dispersed form [69]. Hu et al. used XAS to prove that PtNi diatoms were formed in PtNi-NC and Pt and Ni were coordinated with four N atoms [50].

3.3. In situ infrared spectrum and in situ Raman spectrum

In situ infrared spectroscopy can be used to monitor the interaction between the molecular probe and the catalyst surface in real time, obtain the vibration intensity and frequency changes of the probe, and obtain the information of reactants, target products, electrode surface bonding and intermediates at the molecular level. In in situ Raman spectroscopy, monochromatic incident light is excited to the electrode surface modulated by the potential of the electrode to measure the scattering of Raman spectral signals. In situ technique is of great significance to the study of electrocatalytic reaction mechanism regulating the electronic structure of catalysts and the newly formed bonding mode. Hou et al. prepared a two-site indium-nickel catalyst (InNi DS/NC) anchored to carbon nitride with a 90% FE_{CO} in CO_2RR. In situ attenuated total reflection surface-enhanced infrared absorption spectroscopy (ATR-SEIRAS) experiments were used to monitor the changes in reaction intermediates during the electrochemical reaction (Fig. 4a, b), where the
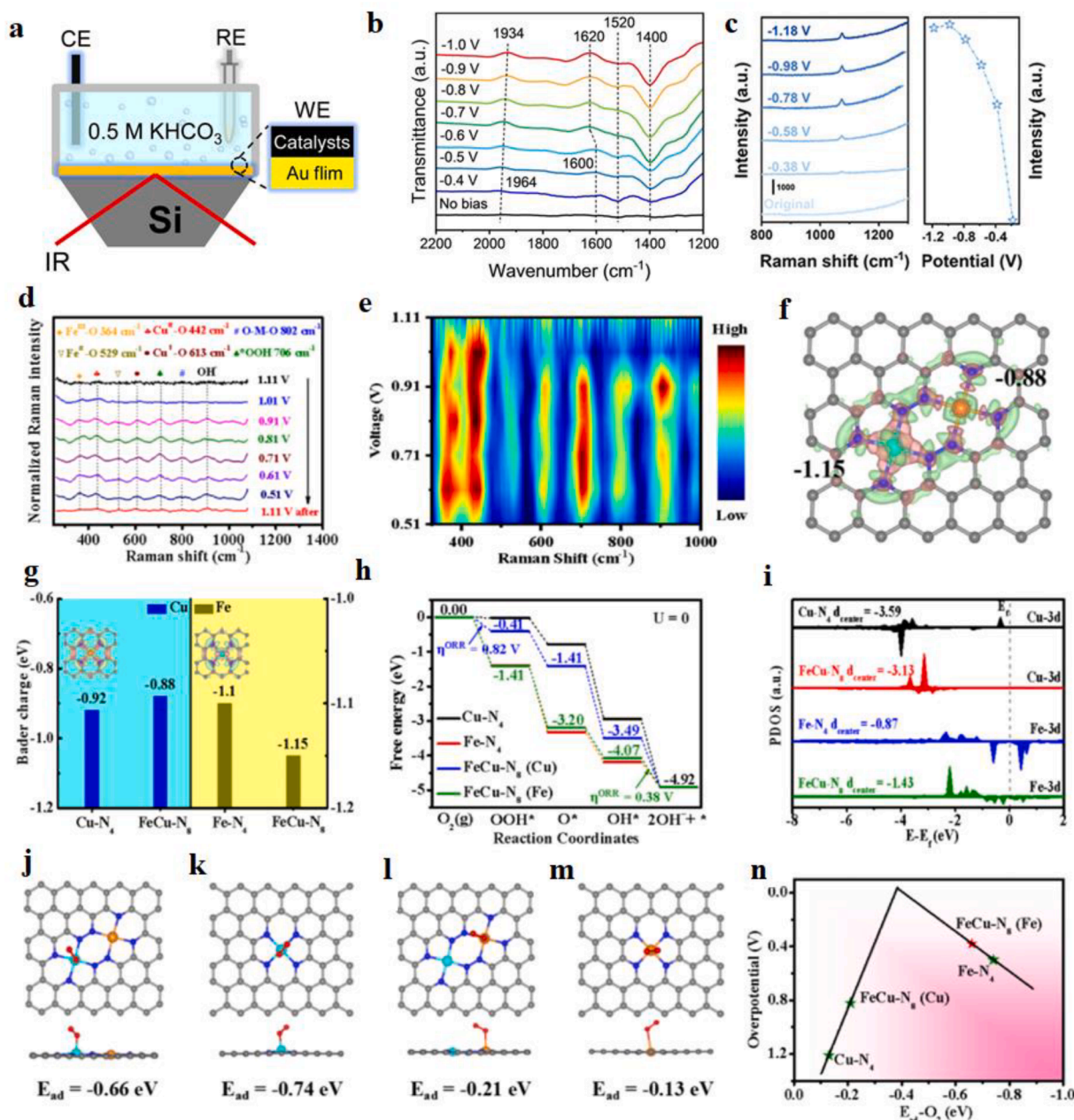

Fig. 4. (a) Schematic diagram of the in situ ATR-SEIRAS experimental setup. (b) In situ ATR-SEIRAS spectra of InNi DS/NC. (c) In situ Raman spectra of CuNi-DSA/CNFs. (d) In-situ Raman spectra of Fe, Cu DAs-NC recorded. (e) The corresponding 2D Raman intensity plot of voltage converted. (f) The charge density polarization plots. (g) Bader charges. (h) Free-energy diagram of ORR. (i) PDOSs of Fe-3d and Cu-3d orbitals. (j–m) Oxygen adsorption energy (E_{ad}) on different Fe atomic sites in (j) $FeCu-N_8$, (k) $Fe-N_4$, and on Cu atomic sites in (l) $FeCu-N_8$ and (m) $Cu-N_4$ models. (n) The volcano plot of overpotential versus E_{ad}-O_2 for the different structures. (a, b) Reproduced with permission.[70] Copyright 2022, Wiley-VCH Verlag GmbH & Co. KGaA. (c) Reproduced with permission.[71] Copyright 2022, Wiley-Blackwell. (d-n) Reproduced with permission.[58] Copyright 2022, Elsevier B.V.

peaks were corresponded to linearly bonded CO (CO_L) and no bridging CO was observed. In addition, the peaks near 1620, 1520 and 1400 cm^{-1} were corresponded to the OH deformation of adsorbed H_2O, the COO stretching vibration of adsorbed CO_3^{2-} group and the C-O stretching of *COOH intermediate, respectively. The peak intensity at 1400 cm^{-1} increased with decreasing potential, which was attributed to the increase of intermediate *COOH on the electrode surface [70]. Zhu et al. synthesized CuN_4 and NiN_4 bimetallic sites (CuNi-DSA/CNFs) on carbon nanofibers. The Faraday efficiency of CO_2 reduction to CO was up to 99.6%. In situ Raman spectroscopy was used to study the formation process of reaction intermediates in CO_2RR. According to the peak location, *COOH intermediates were formed at the active site, and the variation of *COOH peak intensity with potential indicated that *COOH intermediates were aggregated in the CuNi-DSA (Fig. 4c) [71].

Shi et al. studied the intermediates and structural changes of N-bridged Fe and Cu diatomic electrocatalysts (Fe, Cu DAs-NC) in the ORR using in-situ Raman technology. No significant Raman peak was observed at the potential of 1.11 V, because the reaction did not take place. When the potential was 1.01 V, two peaks were observed at 442 cm^{-1} and 529 cm^{-1} for Cu^{II}-OH and Fe^{II}-OH, respectively. With the change of potential, new peaks corresponding to Cu^I-O and Fe^{III}-O appear, indicating that Cu^{II}/Fe^{II} is transformed into Cu^I/Fe^{III} during ORR. In addition, the O-M—O vibration characteristics of Cu and Fe were also observed, indicating that the main active sites of ORR are Fe and Cu. In the process of potential change from 1.11 to 0.51 V, the O-O tensile vibration peak strength of *OOH increased gradually, indicating that the oxygen intermediates were aggregated (Fig. 3d, e) [58]. Monitoring the changes of atomic and electronic structures in diatomic catalysts can better understand the active sites and reaction mechanisms in the actual electrocatalytic process, so as to better design efficient catalysts.

3.4. Theoretical simulations

In recent years, the first principles of density functional theory (DFT) have been widely applied in the field of electrocatalysis, which is beneficial to the design of catalyst and the study of reaction mechanism at the molecular level. The theoretical calculation can not only explain the experimental results, but also predict the reaction energy and activation energy barrier from thermodynamics and kinetics to clarify the reaction mechanism and kinetics. Since the d-band configuration of the metal center determines the adsorption behavior of the reactants at the active site, precise regulation of the electronic configuration of diatomic catalysts can significantly improve the catalytic activity. Theoretical study showed that the introduction of Cu into Fe atoms can change the position of the d-band center of Fe atom, thus strengthening the effect of d-orbital. Zheng et al. prepared FeCu-NC catalyst with CuN_4/FeN_4 sites using a surface confinement strategy. Theoretical calculations showed that electrons transfer from FeN_4 sites to *OH intermediates in the CuN_4/FeN_4 system accelerated the desorption process of *OH intermediates [60].

Shi et al. prepared N-bridged iron and copper diatomic carbon nanocages (Fe, Cu DAs-NC) electrocatalysts using a multi-step collaborative synthesis strategy. DFT calculations were used to construct and optimize the N-bridged Fe-Cu diatomic pair structure model, in which Fe and Cu atoms were coordinated with four N atoms, and N-bridged Fe-Cu diatomic pair structure was separated by bridge N atoms, in which Fe and Cu were coordinated with four N atoms. According to the polarization charge density map, electrons transfer from iron to copper atoms in the bridge diatomic structure. The Bader charge analysis structure is consistent with the result of charge density polarization, which indicates that adjacent metal atoms play an important role in regulating the electronic structure. By calculating the energy barrier in the ORR on different sites, it was confirmed that the rate-determining step (RDS) on the $FeCu-N_8(Fe)$is *OH + e⁻ → OH⁻, on which the theoretical potential is 0.38 V, lower than that of Fe-N_4 interchange active site (η = 0.50 V) (Fig. 4f-m). DFT calculations confirmed that the polarization of the

electronic structure between the bridged FeN_4 and CuN_4 groups could regulate the adsorption free energy of the reactants and intermediates at the bimetallic sites, which enhanced the ORR catalytic activity of Fe-Cu diatomic system [58].

4. Adjusting the electronic structure of diatomic catalysts to optimize the electrocatalytic performance

Carbon-based materials are good carriers of anchor bimetallic atoms, whose electrocatalytic performance can be adjusted by doping heteroatoms, among which nitrogen atoms with high electronegativity and similar size to carbon atoms are usually introduced into carbon matrix to form N-C bond [72,73]. The metal atoms can be fixed by heteroatom or base surface environment, during which the electronic structure of metal atoms will be changed, and the catalyst with M−N−C structure is obtained. In addition, supported diatomic catalysts can also be synthesized by directly introducing atomic dimers to carbon-based materials. The strong bonding of the active site and the interaction with carbon support give diatomic catalysts high efficiency and stability of electrocatalysis. A suitable diatomic catalyst can be constructed by regulating the electronic structure of carbon-based diatomic catalyst. In this section we will regulate the electronic structure of diatomic catalysts from three aspects (bimetallic central atoms, local coordination environment of bimetallic central atoms, and carbon-based environment) for efficient catalysis of various reactions, including HER, OER, ORR, CO_2RR, and NRR.

4.1. Adjusting the electronic structure of bimetallic central atoms

Compared with single metal center, double metal centers have dual function, and there are synergies between them. By adjusting the types and proportions of double metal centers, the electronic structure, and the bonding strength between them can be adjusted. The active sites of diatomic catalysts can be divided into the same metal sites and different metal sites. By adjusting the electronic structure of bimetallic atoms, it can be used to catalyze different reactions.

4.1.1. Homonuclear diatomic sites

Catalysts with the same metal central atomic sites are equivalent to single-atom catalysts in which the single atom is replaced by the double atoms, and the atomic load and the number of active sites are increased [74,75]. The d electrons of the two metal atoms cooperate with each other, and thus the catalytic performance of DACs is obviously better than that of SACs [76]. In addition, catalysts with the same metal central atomic sites can provide symmetrical adsorption sites for reactant molecules due to the same d electron structure, which can enhance the thermodynamic stability [77]. Lu et al. synthesized graphene-loaded Pt_2 dimers (Pt_2/graphene) in an atom-by-atom load sequence using atomic layer deposition. The activity of Pt_2/graphene is 17 times higher than that of Pt_1/graphene in ammonia borane (AB) hydrolysis for hydrogen production. Moreover, it showed good stability under reaction conditions and inert atmosphere below 300 ℃. DFT calculations showed that the high activity of Pt_2/graphene was due to the low adsorption energy of adsorption molecules on Pt_2 dimer [77]. Li et al. synthesized supported Pd_2 diatomic catalyst by anion replacement deposition and precipitation technology [56], showing 98.2% FE_{CO} at −0.85 V vs. RHE, and good stability (Fig. 5a-e) in the CO_2RR. DFT calculations showed that the excellent catalytic performance of Pd_2 diatomic catalyst was due to the existence of the dimer Pd_2 active sites rather than the influence of the surrounding environment. In the CO_2RR, the RDS was the transformation of CO_2 into COOH*, and the energy barrier of the dimer Pd_2 active site was 1.28 eV, lower than that of the single-atom Pd site. In addition, although the RDS energy barrier at Pd NP/C active site was lower, the CO* desorption process needs to cross a large energy barrier (1.54 eV), resulting in CO poisoning, which is not conducive to the reaction. The excellent catalytic performance at the dimer Pd_2 active sites
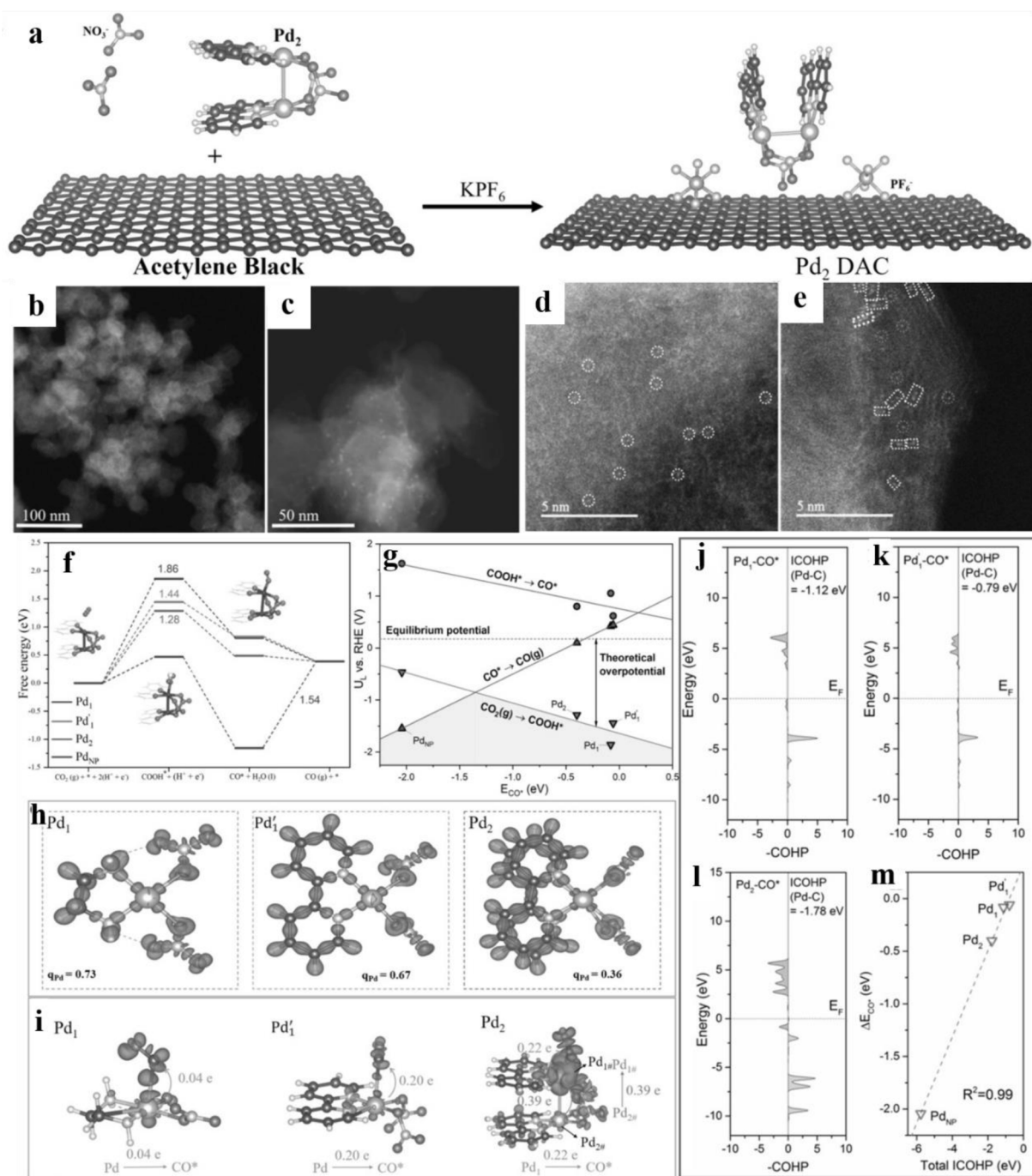
Fig. 5. (a) The preparation strategy for Pd_2 DAC. AC-HAADF-STEM of (b) C support, (c) Pd NP/C, (d) Pd_1 SAC, and (e) Pd_2 DAC. (f) Free energy profile of CO_2RR. (g) U_L as a function of adsorption energy of CO^* (ΔE_{CO^*}). (h) Charge density difference. (i) Charge density differences for CO^* adsorption states and corresponding charge transfer. Calculated pCOHP diagram of (j) Pd_1-CO^*, (k) Pd_1'–CO^* and (l) Pd_2-CO^*. (m) Correlation between the total ICOHP and ΔE_{CO^*}. Reproduced with permission.[56] Copyright 2021, Wiley-VCH.

is due to the moderate intensity of CO^* adsorption between Pd_2 sites, which is conducive to the activation of CO_2 into $COOH^*$ and the desorption of CO^*. In addition, it is also attributed to electron transfer of Pd atom at the active site of dimerization of Pd_2 (Fig. 5f-m).

In addition to the supported homonuclear dimerization, the diatomic catalysts coordinated with nitrogen have been widely studied. Zhou et al. synthesized a diatomic Ag_2/graphene catalyst (Ag_2-G) with AgN_3-AgN_3 active site [55]. The catalyst showed good electrocatalytic performance of CO_2RR, and the FE_{CO} was up to 93.4%, and the stability was over 36 h (FE_{CO} = ~90%). Theoretical calculations showed that C and O of CO_2 reacted with two Ag at the AgN_3-AgN_3 site to stabilize the CO_2

adsorption intermediate and reduce the energy barrier between CO_2 and the reaction intermediate *COOH. In addition, the free energy of *CO to form *COH (2.61 eV) is much higher than that of *CO to release CO (0.16 eV), thus showing high CO selectivity in the CO_2RR.

In addition to precious metals, transition metals such as Fe, Co, Ni and Cu are a good choice to coordinate with N to form diatomic catalysts. Xiong et al. synthesized Fe_2-cluster anchored N-doped carbon (Fe_2-N-C) using pyrolysis strategy [78]. The catalyst has excellent catalytic ORR activity with a $E_{1/2}$ of 0.78 V (vs. RHE), and shows long-term stability under acidic conditions. The experimental and theoretical results showed that the catalytic performance of Fe_2-N-C is better than that of

Fe$_1$-N-C and Fe$_3$-N-C. Although Fe$_2$-N-C (3.10 eV) and Fe$_3$-N-C (3.17 eV) are conducive to the adsorption of O$_2$, Fe$_2$-N-C has more catalytic active sites. According to XAFS spectra, Fe$_2$ clusters exhibited a low oxidation state in the Fe$_2$-N-C structure, and there was a strong bonding hybridization between Fe 3d and O 2p, which is conducive to enhancing electron transfer and activating O$_2$ molecule. Xie et al. obtained a planar catalyst with Fe$_2$N$_6$ structure by controlling the dispersion and heating degree of FeN$_4$ heme molecules on a highly graphitized carbon substrate for migration and coupling [79]. The catalyst had excellent catalytic activity for oxygen reduction with positive E$_{1/2}$ up to 0.84 V and a small Tafel slope (82 mV dec^{-1}), indicating that it had fast kinetics in catalytic ORR process. In addition, Fe$_2$N$_6$ structure can maintain excellent stability in catalytic ORR process. In situ XAS measurements showed that the planar Fe$_2$N$_6$ structure can improve the high intrinsic activity and accelerate ORR kinetics. In addition, in the ORR process, oxygen adsorption on the Fe$_2$N$_6$ structure, transformation of intermediates and product desorption all led to the stretching or compression of Fe-Fe coordination bonds and the changes in Fe-Fe shells (Fig. 6a-c). The O of the oxidized intermediate on the planar Fe$_2$N$_6$ structure was adsorbed on both sides of the two Fe atoms, which is conducive to the breakage of O = O bond and the dissociation of the oxidized intermediate. Compared with Fe$_2$N$_6$, intermediate O was usually adsorbed at the end of FeN$_4$, which is not conducive to O = O bond breakage. In addition, the distance between two adjacent Fe atoms in Fe$_2$N$_6$ structure was shortened with

the decrease of applied voltage, which indicated that the synergy between two adjacent Fe atoms can regulate the adsorption and dissociation of oxygen-containing species and accelerate the ORR dynamics. In the ORR process, O$_2$-Fe^{3+}-Fe^{2+} can finally be converted to Fe^{2+}-Fe^{2+}, indicating that the oxidation degree of Fe can be induced to decrease by adsorbed oxygen intermediates (Fig. 6d-f). The reason why the planar Fe$_2$N$_6$ structure has excellent catalytic performance of ORR may be that the large specific surface area provides abundant active sites, and the optimization of adsorption and desorption energy and the strong energy of O = O bond fracture improve the kinetics of ORR and inhibit side reactions.

Fe$_2$ dimers can not only catalyze ORR, but also catalyze CO$_2$RR with good selectivity and activity. When adjacent metal atoms coordinate with nitrogen anchored on the carbon substrate as the CO$_2$RR active site, two CO$_2$ molecules can be simultaneously fixed on this site, which is conducive to the C-C coupling to produce C$_2$ or C$_{2+}$ products. Zhou et al. used theoretical calculations to study the CO$_2$RR selectivity on 3d transition metal dimer anchored to porous N-doped carbon sheets [80]. When Fe$_2$-dimer was fixed in C$_2$N monolayer, it showed high activity and selectivity of C$_2$H$_5$OH and other C$_1$/C$_2$. The reaction activity and product selectivity can be improved by controlling the coupling strength of metal and substrate. The excellent CO$_2$RR activity of the limited dimer catalyst on carbon was attributed to the simultaneous adsorption of two CO$_2$ molecules, the prevention of CO desorption, and the excellent C-C
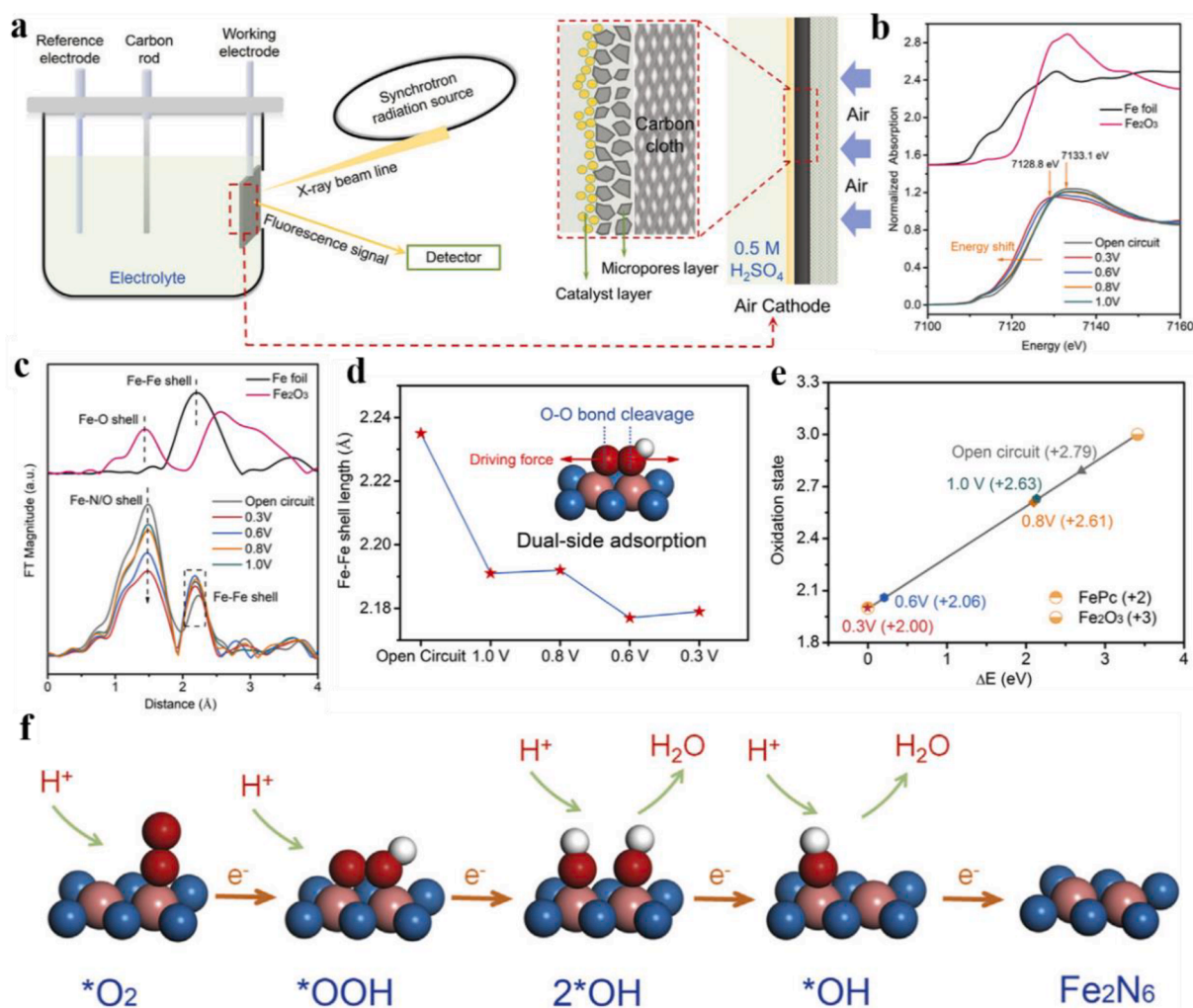

Fig. 6. (a) Schematic of the operando XAS setup. (b) Operando XANES spectra and (c) corresponding FTs of Fe K-edge EXAFS oscillations of planar-like Fe$_2$N$_6$ structure at different applied potentials in 0.5 M H$_2$SO$_4$. (d) Fe-Fe shell length calculated from operando EXAFS spectra. (e) Fitted average oxidation state of Fe in the planar-like Fe$_2$N$_6$ structure according to operando XANES spectra. (f) Proposed ORR reaction pathways on the planar-like Fe$_2$N$_6$ structure. Reproduced with permission.[79] Copyright 2020, Elsevier Inc.

coupling pathway. Han et al. designed a bimetallic iron site catalyst on a nitrogen-doped carbon matrix (Fe$_2$-N-C), which showed good catalytic activity and CO selectivity. The FE$_{CO}$ exceeded 80%, and the conversion rate can reach 26,637 h^{-1} [81]. DFT calculations showed that the orbital coupling of diatomic iron sites reduces the band gaps of antibonding and bonding states in the adsorption of *CO, which is conducive to the adsorption of reaction intermediates and improves the catalytic activity of catalysts.

Although Fe-N-C catalysts have higher ORR activity than Co-N-C catalysts, the latter has better stability. Xing et al. synthesized ZnCo-ZIF precursors by precisely regulating the atomic-scale structure of the

bimetallic organometallic skeleton, and obtained a binuclear catalyst with Co$_2$N$_x$C$_y$ structure through pyrolysis [82]. The catalyst showed good catalytic ORR activity with initial potential and E$_{1/2}$ of 0.92 V and 0.79 V, respectively. The maximum value of wavelet transform (WT) was observed by XAS, which was caused by the shortening of the Co-Co distance (2.12 Å), indicating the presence of bimetallic Co-Co clusters. Theoretical calculations were used to construct the model of various configurations, showing that the catalyst had Co$_2$N$_5$ structure. The optimal ORR path on Co$_x$N$_y$ structure was determined by DFT calculations, that is, O$_2$ → *O$_2$ → *OOH → *O → *OH → H$_2$O. The calculated results showed that the OH adsorbed on Co$_2$N$_5$ structure is favorable for
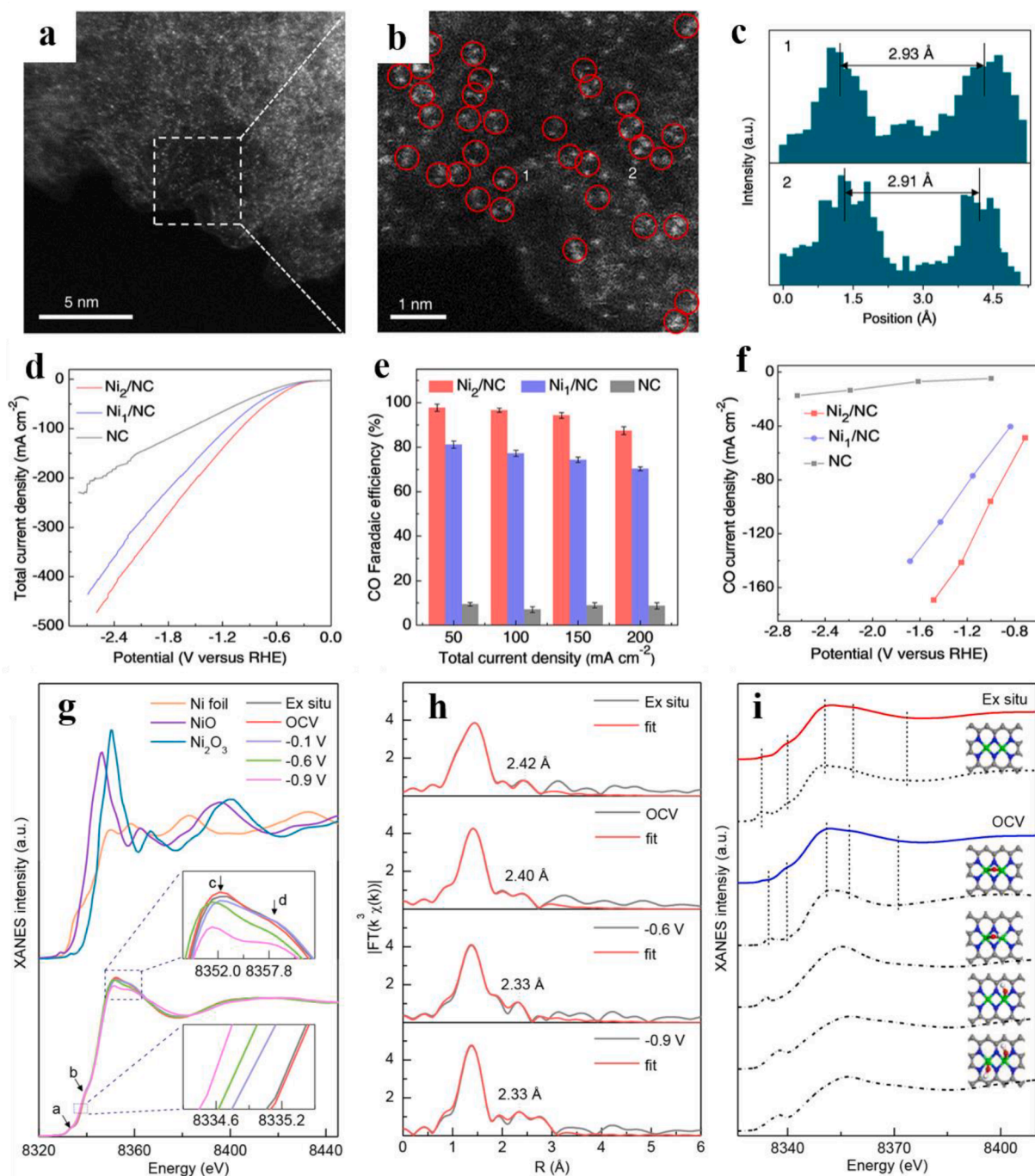

Fig. 7. (a, b) HAADF-STEM image (a) of Ni DSC (enlarged in b). (c) Intensity profiles obtained on the zoomed areas 1 and 2 in (b). (d) LSV curves. (e) FE$_{CO}$. (f) CO current density on the Ni$_2$/NC, Ni$_1$/NC, and NC catalysts. (g) Operando XANES spectra at the Ni K-edge. (h) Least-squares curve-fitting analysis of operando EXAFS spectra at the Ni K-edge. (i) Comparison between the Ni K-edge XANES experimental spectra (solid lines) and the theoretical spectra (dashed lines) calculated with the depicted structures (insert). Reproduced with permission.[57] Copyright 2021, American Chemical Society.

the conversion of *OH into H_2O. When $Co_2N_5(OH)$ is the active site, no thermodynamic barrier is needed to overcome at each step of the reaction at U = 0 V or 0.52 V. Therefore, the binuclear site reduces the thermodynamic barrier and improves the intrinsic ORR activity.

Bimetallic nickel site catalysts show good selectivity in catalyzing CO_2RR. Cao et al. synthesized a Ni_2 cluster catalyst by one-pot method, in which the nickel content was to 1.067% (Ni-N@C1) [63]. HAADF-STEM and EXAFS results showed that there were diatomic Ni_2 sites in the Ni-N@C1. Ni-N@C1 exhibited good CO_2RR catalytic activity and CO selectivity at low load. The FE_{CO} exceeded 95% at −0.6 V ~ -1.0 V, and the current density reached 37.2 A mg^{-1} at −1.1 V. Yao et al. synthesized nitrogen-doped carbon materials with binuclear nickel (Ni_2/NC and Ni DSC) by pyrolysis of MOF precursors containing $Ni_2(dppm)_2Cl_3$ clusters . The distribution of diatomic Ni_2 sites can be observed through HAADF-STEM images, and the distance between adjacent Ni atoms is about 2.9 Å (Fig. 7a-c). Ni_2/NC showed good activity and CO selectivity in catalytic CO_2RR, and the FE_{CO} reached 94.3% (j = 150 mA·cm^{-2}). Ni_2/NC showed a high CO geometric current density during the catalytic process. When the voltage is −1.25 V, the current density can reach 141 mA cm^{-2} (Fig. 7d-f). Ni_2/NC catalyst had high reaction rate and charge transfer capacity and maintained good durability. The structure of Ni_2-N_6 in Ni_2/NC catalyst was revealed by XAS spectra, and the dynamic evolution of active site Ni_2-N_6 was revealed during CO_2RR process. The oxygen intermediate was adsorbed on Ni_2-N_6 to form O-Ni_2-N_6, which is the real active site. In addition, the interaction between adjacent Ni increased with the increase of voltage in the reaction (Fig. 7g-i). DFT calculations revealed that the conversion of CO_2 to COOH* is the RDS for CO_2RR and the Gibbs free energy (ΔG = 0.77 eV) on the O-Ni_2-N_6 active site was significantly lower than that on Ni_2-N_6 active site (ΔG = 1.35 eV).

Some researchers studied the catalytic effect of two kinds of transition metal atoms immobilized on carbon materials on the CO_2RR performance by theoretical calculations. Sun et al. studied the catalytic CO_2RR on the first transition metal dimer immobilized on phthalocyanine sheets, in which Mn dimer showed the best selectivity for reducing CO_2 to CH_3OH [83]. The reaction process is CO_2 → COOH* → CO* → CHO* → CH_2O* → CH_3O* → CH_3OH, and the RDS is the conversion of CO_2 to COOH*. Mn dimer can significantly reduce the activation energy, and the overpotential is 0.84 V. The catalytic performance is improved because COOH* is conducive to the bonding of reaction intermediate and dimer Mn, forming bridge adsorption Mn-C-O-Mn. This structure is also conducive to metal adsorption π-back bonding, conducive to the conversion of C-terminal and O-terminal adsorbent, reducing the energy required for methanol desorption. Chen et al. investigated the catalytic effect of several transition metal dimers loaded on the porous C_2N layer (M_2@C_2N), and found that Cu_2@C_2N has excellent selectivity of CH_4 and C_2H_4 in catalytic CO_2RR [84]. There is strong hybridization in Cu 3d and N 2p orbitals, and thus Cu_2@C_2N structure is very stable. The best way to selectively generate CH_4 is CO_2 → HCOO* → HCOOH* → H_2COOH* → H_2CO* → H_2COH* → CH_2* → CH_3* → CH_4, and the RDS is HCOO* → HCOOH*. The Gibbs free energy is + 0.23 eV, and the limiting potential is −0.23 V. In addition, the best way to generate C_2H_4 is CO_2 → COOH* → CO* → COCO* → HCOCO* → C_2OH* → C_2H * → C_2H_2* → C_2H_3* → C_2H_4, where CO* → COCO* is the RDS with Gibbs free energy of 0.76 eV.

The electrocatalytic NRR activity of a series of single and double transition metals anchored on C_2N with uniform hole distribution was investigated. Jiang et al. fixed Cr, Mn, Fe, Co and Ni on C_2N (TM-C_2N) in the form of single and double atoms [85]. DFT calculations showed that Mn_2-C_2N has the optimal catalytic NRR performance, and the minimum potential is −0.23 V. The strong coupling between Mn and N and the porous properties of Mn_2-C_2N catalyst make the catalyst have good stability, and the introduction of bimetal atoms makes the electron rearrangement, optimizes the electronic structure, and improves the catalytic performance. Zhou et al. studied a series of transition metal atom-anchored C_2N electrocatalysts by theoretical calculations, among

which Mo_2@C_2N showed the best catalytic activity and NH_3 selectivity in the NRR [86]. The reaction process is N_2 (g) → N_2* → *N_2H → *N-NH_2 → *N-NH_3 → *N-NH_3 (g) → *NH → *NH_2 → NH_3 → NH_3 (g), and the RDS is *NH → * NH_2 with Gibbs free energy of 0.41 eV. According to the calculation of transition state, the energy barrier of 0.51 eV for *NH formation can be obtained. Huang et al. anchored metal dimers on the two-dimensional expanded phthalocyanine (Pc) framework, in which the homonuclear dimers Ti_2-PC and V_2-PC had a small negative limiting potential of −0.75 V and −0.39 V in the catalytic NRR, respectively [87]. The potential determination step (PDS) is NH_2* → NH_3*. Furthermore, $H_5O_2^+$ as a protic solvated proton donor can significantly reduce the activation energy barrier of PDS (0.38 eV and 0.35 eV).

4.1.2. Heteronuclear diatomic site

As diatomic catalysts with different metal centers, the asymmetric sites can directly regulate the electronic structure and affinity of d-band. The two different metal sites play a double role and synergistic effect, and many different adsorption geometry configurations will appear in the reaction process. For example, one reactant molecule can be bonded to two metal sites, or two reactant molecules can be bonded to two metal sites. In addition, by adjusting the interaction between the active site and the reaction intermediates, the catalytic performance can be improved. In this section, we mainly discuss the influence of different metal center atomic sites on the catalytic performance of ORR, OER, HER, CO_2RR and NRR.

4.1.2.1. Water splitting. Water splitting is an efficient strategy to produce hydrogen energy with high weight energy density and zero carbon emission [88-91]. Electrochemical water splitting consists of hydrogen evolution at the cathode and oxygen evolution at the anode. Theoretically, water splitting requires a 1.23 V thermodynamic energy barrier, but in practice, slow kinetics and high overpotential at cathode/anode are the main obstacles of large-scale application of water splitting [92]. Therefore, it is necessary to fabricate high-performance catalysts to improve reaction kinetics and reduce HER/OER overpotentials.

Noble metal platinum-based materials show good performance in catalyzing cathode HER. With the rise of diatomic catalysts, a second metal atom can be introduced into the single-atom catalyst to adjust the electronic structure of the catalyst, so that it can show better catalytic HER activity. In 2017, Yu et al. accurately grafted Pt atoms at Fe-N_4 site by bridging oxygen molecules to obtain a new active Pt_1-O_2-Fe_1-N_4 site (Fig. 8a-f) [93]. The modified active site showed excellent HER catalytic activity (η_{10} = 60 mV) under acidic conditions, which was significantly better than RuO_2 catalyst. Theoretical calculations showed that the modified active site promoted proton adsorption and reduction kinetics. Pt_1@Fe-N-C catalyst exhibited low ΔG_{H*} value (0.16 eV) at pH = 14 (Fig. 8g-i). Sun et al. synthesized a bimetallic Pt-Ru dimer by atomic layer deposition technology. The catalytic hydrogen evolution activity of the catalyst was significantly higher than that of commercial Pt/C catalyst, and the overpotential was as low as 19.6 mV [28]. XAS spectra and theoretical calculations showed that Pt-Ru bonds existed in the diatomic catalyst. Pt-Ru dimer can be converted from metal to semiconductor by adsorption, resulting in unoccupied orbitals. With the increase of hydrogen adsorption in Pt(3H)Ru(2H), ΔG_H is close to 0 (0.01 eV). The adjustment of electronic structure of Pt-Ru dimer significantly improved the catalytic activity of HER.

In addition to noble metal diatomic catalysts, O-coordination W-Mo dimer on N-doped graphene reported by Yang et al. showed good HER activity (η_{10} = 24 mV). In the bimetallic DAC (W_1Mo_1-NG), heteronuclear W-Mo bimetals were fixed at NG vacancies, and W and Mo were bonded to oxygen [51]. The W-O-Mo-O-C configuration was formed by strong covalent bond interaction, involving the tetrahedron of oxygen bridge [WO_4] and the octahedron of distorted MoO_6. In the bimetallic W-Mo dimer, the electronic structure was adjusted, and the delocalized electrons facilitated the adsorption of H to accelerate the kinetics of HER
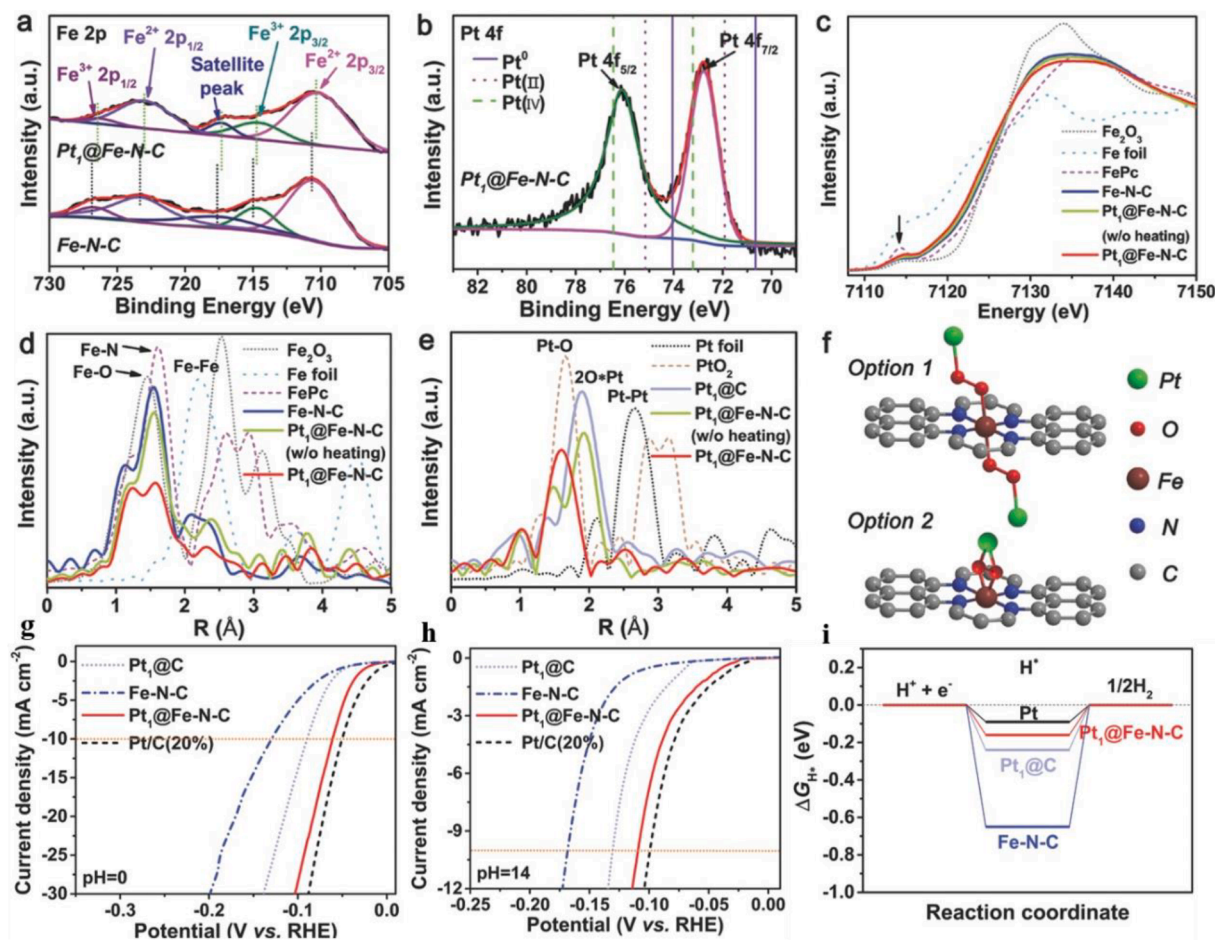
Fig. 8. (a, b) XPS spectra of Fe 2p and Pt 4f. (c) Normalized XANES and (d) FT-EXAFS data of Fe. (e) FT-EXAFS data of Pt. (f) Proposed schematic diagram of Pt_1-O_2-Fe_1-N_4-C_{12} as the active moiety of $Pt_1@Fe$-N-C. (g) HER polarization curves. (h) HER polarization curves. (i) Free energy ΔG_{H^*} of H* adsorption. Reproduced with permission.[93] Copyright 2017, Wiley-VCH.

and enhance the catalytic activity. DFT calculations showed that the W-O-Mo-O-C configuration has the best synergistic effect. W-Mo heteronuclear dimers show strong covalence and weak ionic properties, while Mo_2-NG and W_2-NG homonuclear dimers show strong ionic properties due to the rich electrons around the coordination atoms, while the electrons in the metal center are depleted by the coordination O site. As a result, there is a strong binding energy with H, which is not conducive to HER.

The anodic OER is a complex four-electron transfer process, which needs to overcome a high energy barrier and shows a slow kinetics. Therefore, the key to improve the efficiency of overall water splitting is to find an efficient catalyst to reduce the OER energy barrier and improve the OER kinetics [94-96]. At present, the research on OER catalyst mainly focuses on alkaline media, and the research shows that bimetal catalysts are generally more active than single metal catalysts. The addition of trace iron to pure NiO_x and CoO_x significantly increased their OER activity [97]. Hu et al. obtained Co-Fe diatomic catalyst (Co-Fe-N-C) by introducing iron onto the synthetic nitrogen doped carbon dispersed by cobalt atoms. In-situ XAS showed that the dimer Co-Fe structure was formed in the catalyst, and this structure was the active site of OER, which maintained good stability in the OER process. The catalytic activity of the catalyst was significantly higher than that of Co-N-C. At $\eta = 300$ mV and 350 mV, the turnover frequency (TOF) was greater than 1 s^{-1} and about 12 s^{-1}, respectively [98]. Duan et al. reported an Fe-Ni dual-site catalyst supported on microporous carbon. DFT calculations showed that the reaction intermediates OH* and O* wee simultaneously activated at the active Fe-Ni bimetallic sites, and the

adjacent active sites of different metals regulated the energy barrier of the RDS and accelerated the OER kinetics [99].

Compared with noble metal, non-noble metal Co site has weak binding with oxygen intermediates, and electron-absorbing nitrogen-containing carbon material will reduce the oxygen adsorption on the weak metal site, resulting in poor catalytic activity. Chen et al. designed an IrCo-N-C catalyst with asymmetric $IrCoN_5$ structure, which showed enhanced OER and ORR activity, with a $E_{1/2}$ of 0.911 V and an η_{10} of 330 V. The asymmetric $IrCoN_5$ structure effectively adjusts the d orbital occupancy of Co, making Co-O have the best affinity [100]. Table 1 shows the performance comparison of carbon-based diatomic catalysts for water splitting.

4.1.2.2. Orr. In energy storage technology, metal-air battery has been widely concerned because of its high energy density and high safety, where ORR is the core component [103-106]. In addition, polymer electrolyte membrane fuel cells (PEMFC) have been widely used as electrochemical devices in portable and stationary power systems and automotive engines [107]. As the cathode, ORR involves a multi-electron transfer process and has a high energy barrier, resulting in slow kinetics. The excellent ORR catalyst should have active sites for O_2 cleavage, excellent electronic and geometric structure conducive to O_2 diffusion and can maintain long-term stability. Current studies show that Pt and Pd catalysts are the best catalysts in the catalytic ORR. However, the high cost of precious metal catalysts, CO poisoning, and vulnerable reaction intermediates in the battery operating environment, which limit the large-scale commercial applications in metal-air

Table 1

Comparison of water splitting performance on carbon-based diatomic catalysts.

Catalyst	Reaction	Active site	Electrolyte	Overpotential at 10 mA cm^{-2} [mV]	Tafel slope [mV dec^{-1}]	Ref.
W_1Mo_1-NG	HER	W-O-Mo-O-C	0.5 M H_2SO_4	24	30	[51]
W_1Mo_1-NG	HER	W-O-Mo-O-C	1 M KOH	67	45	[51]
Pt_1@Fe-N-C	OER	Pt_1-O_2-Fe_1-N_4	1 M KOH	60	38	[93]
Fe–NiNC-50	OER	FeNi- N_6	1 M KOH	340	54	[101]
Pt_1@Fe-N-C	OER	Pt_1-O_2-Fe_1-N_4	1 M KOH	310	62	[93]
Co-Fe-N-C	OER	Co–Fe	1 M KOH	321	40	[98]
IrCo–N–C	OER	$IrCoN_5$–Co	0.1 M KOH	330	79	[100]
CoNi-SAs/NC	OER	CoNi- N_6	0.1 M KOH	340	58.7	[102]

batteries and PEMFC [108]. Therefore, current research focuses on diatomic metal catalysts to replace precious metals Pt and Pd, including precious metal-non-precious metals and double non-precious metals.

Compared with SACs, DACs have synergistic effect, which is beneficial to catalytic reactions. The structure of the d orbitals can be affected by the difference of local d electron density and the asymmetry of atomic coordination in heteronuclear DACs. The configuration of the spin d orbitals of non-precious metals can change in the local coordination environment, while the d orbitals of precious metals have high

limitation and weak interaction with the intermediates produced in the reaction process. Therefore, noble metal-non-precious metal diatomic catalysts would show good catalytic performance. Yao et al. synthesized a locally distributed atomic Pt-Co nitrocarbon-based catalyst, which showed excellent ORR activity and stability, with $E_{1/2}$ of 0.96 V and a mass activity of 45.47 A mg^{-1} [109]. The bimetallic IrCo-N-C catalyst synthesized by Chen et al. showed good catalytic ORR activity with $E_{1/2}$ of 0.911 V. The bimetallic interaction improves the activity of the catalyst [100]. Sun et al. prepared a heteronuclear diatomic precious
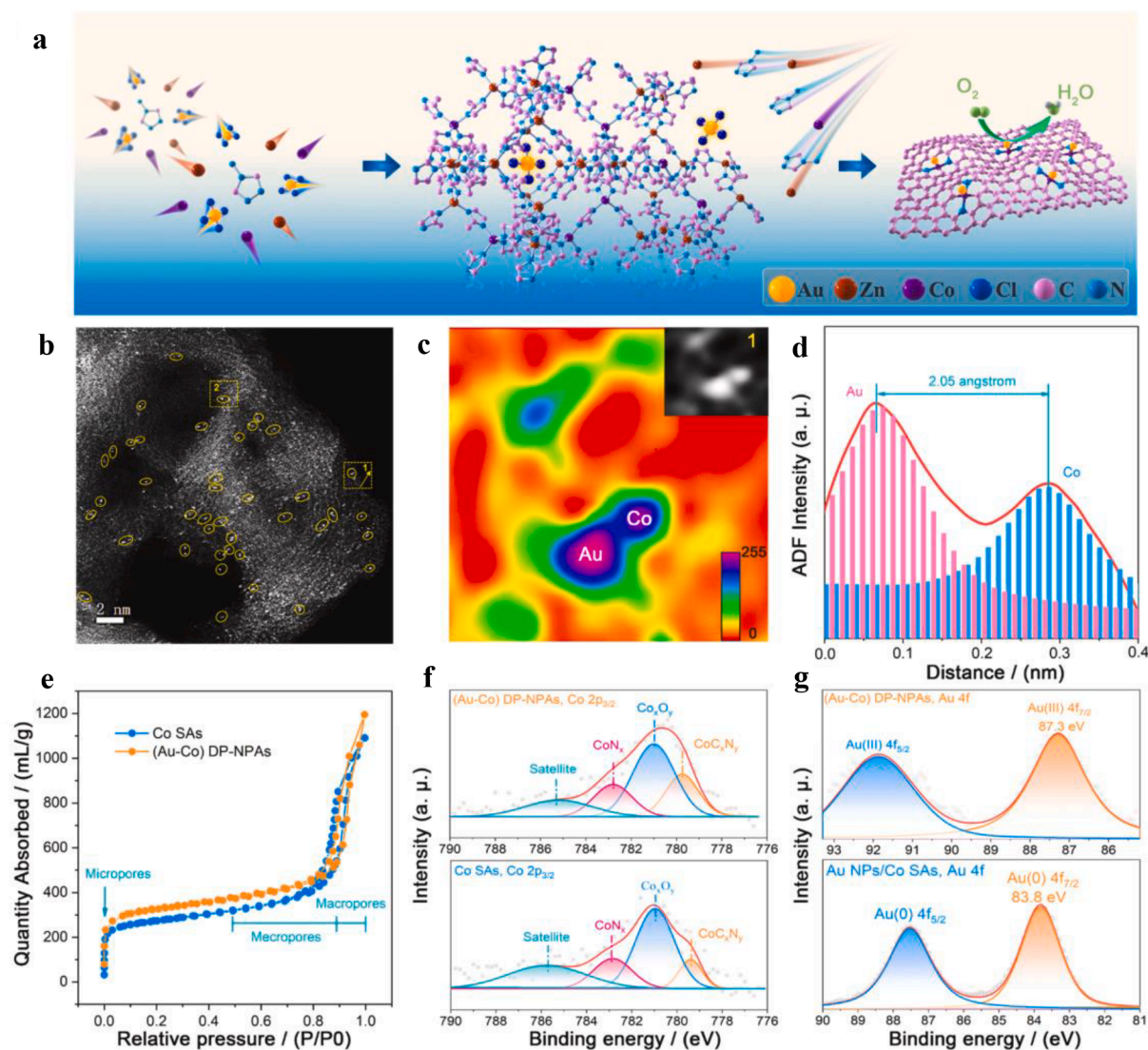

Fig. 9. (a) Schematic illustration of (Au-Co) DP-NPAs. (b) Aberration corrected-HAADF-STEM image. (c) The colored raster graphic of region 1 in Fig. b. (d) The intensity profile along the arrow in region 1 of Fig. b. (e) N_2 absorption–desorption isotherms. (f) and (g) XPS spectra. Reproduced with permission.[110] Copyright 2021, Elsevier B.V.

non-precious (Au-Co) DP-NPA catalyst by hydrothermal and pyrolysis techniques (Fig. 9a) [110]. The catalyst showed excellent ORR activity with $E_{1/2}$ of 0.82 V. The peak power density of PEMFC can reach 360 mW·cm^{-2}. From Fig. 9b-g, there is isolated bimetals at the edge of carbon matrix of (Au-Co) DP-NPA with Co and N coordination, and gold is trivalent. XAS and theoretical calculation results show that the active site of ORR is Co-N$_2$C$_2$ structure with axial connection to Au atom. When *OH is adsorbed to Co atom, it will cause a coordinated change of symmetry of neighboring Au atoms, which will make the anti-bond spin orbital reach a low energy level and improve the ORR activity. The improved ORR kinetics of DP-NPA catalyst is attributed to the robust

coupling between the totally occupied d orbital (Au) and the spin d orbital (Co).

The synergistic effect of metal sites in diatomic non-noble metal catalysts can cause charge redistribution and d-band center shift. According to Sabatier's principle, a good catalyst should have a medium bond with an atom or molecule, and too strong for desorption of the product and too weak for activation of the reactant might take negative effect in electrocatalytic reactions [111]. Strasser et al. used chemisorption/desorption and ^{57}Fe Mossbauer spectroscopy techniques to study the surface adsorption sites of M−N−C materials. They demonstrated that the nonmetallic diatomic (Fe,Mn)-N-C catalyst exhibited
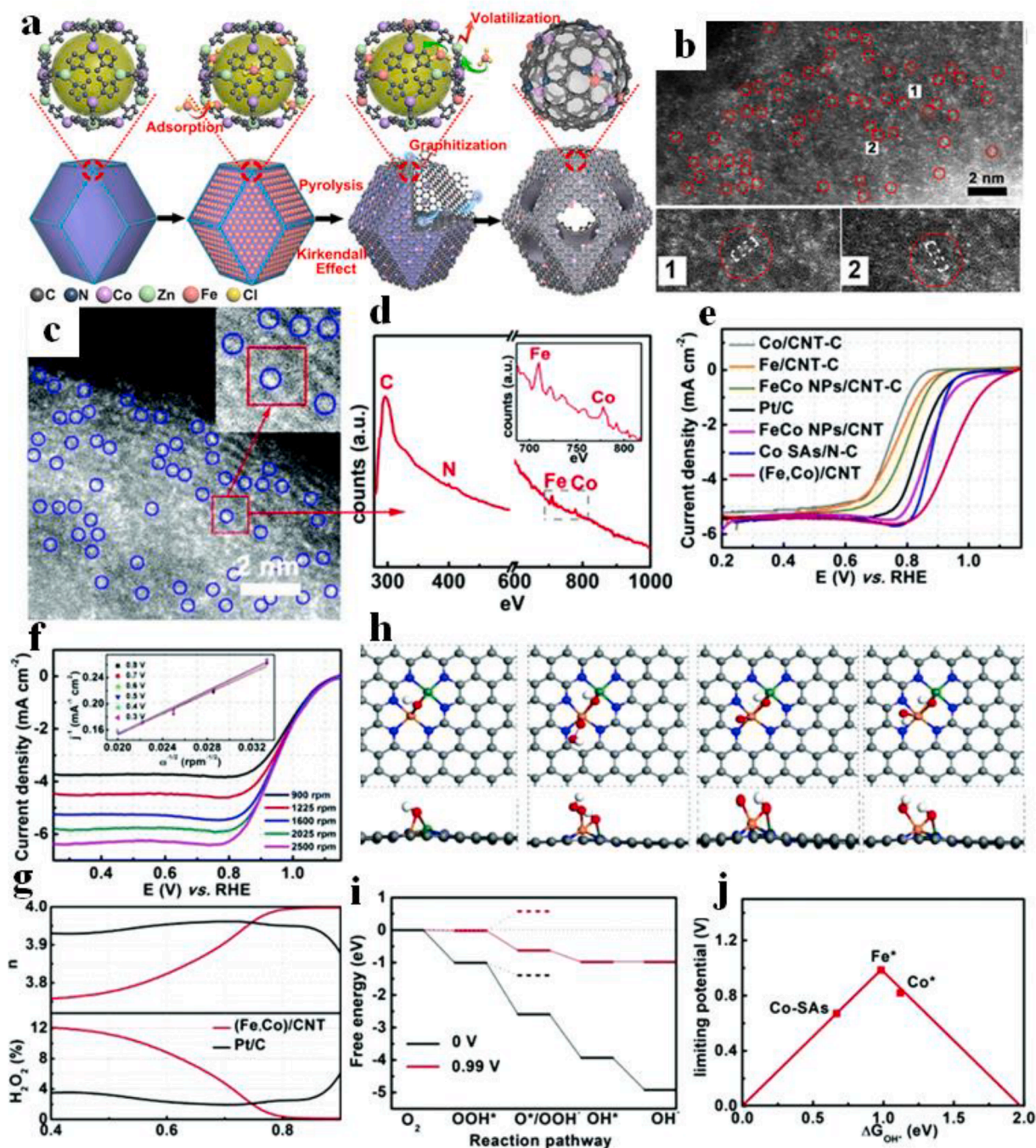

Fig. 10. (a) Preparation of (Fe,Co)/N-C. (b) Magnified HAADF-STEM of (Fe,Co)/N-C. (c) Magnified HAADF-STEM images of the (Fe,Co)/CNT. (d) The EEL spectrum. (e) RDE polarization curves. (f) Tafel plots. (g) Electron transfer number (n) and H$_2$O$_2$ yields vs. potential. (h) Geometric structures of the intermediates. (i) The free energy diagram. (j) Volcano plot. (a-b) Reproduced with permission.[112] Copyright 2017, American Chemical Society. (c-j) Reproduced with permission.[113] Copyright 2018, The Royal Society of Chemistry.

good activity in catalytic ORR. The synergistic interaction of Fe and Mn regulated the internal electronic structure and facilitated ORR [32]. Wu et al. designed a dual-site Fe-Co hollow carbon material ((Fe,Co)/NC) by a host–guest approach, in which Co nodes were controlled to bond with adsorbed Fe sites in the metal–organic framework (MOF) (Fig. 10a, b). In addition, the adsorbed Fe ions can adjust the electronic structure and geometric configuration of the carbon carrier, which is beneficial to improve the mass transfer rate. (Fe,Co)/NC had excellent ORR activity in acidic medium with $E_{1/2}$ of 0.863 V and E_{onset} of 1.06 V. Theoretical calculations showed that the strong bonding of O_2 at Fe-Co double sites increases the O-O bond length from 1.23 Å to 1.40 Å, and the O-O bond becomes easy to break. The dissociation energies of $O_2 \rightarrow O$ (0.25 eV) and $OOH \rightarrow OH$ (0.02 eV) are significantly lower than those of Fe/NC and Co/NC catalysts. The O atom dissociated on the (Fe,Co)/NC has two adsorption sites, which is conducive to the formation of stable products. The conversion of adsorbed OH to H_2O is the RDS in the ORR, and the activation barrier at the Fe-Co double site is 0.26 eV, which is lower than those of single-site catalysts [112]. In a subsequent study, Wu et al. introduced Fe-Co double sites in N-doped carbon nanotubes by controlling the connection of iron ions to cobalt nodes in the Zn/Co bimetallic MOF. HAADF-STEM images and EEL spectra indicated that Fe and Co coexisted in the (Fe,Co)/CNT (Fig. 10c, d). The structure of $FeCoN_6$ in (Fe,Co)/CNT was revealed by EXAFS spectroscopy. The unique internal electronic structure, coordination location and deformed porphyrin structure of Fe-Co bond all significantly affect the ORR performance. Compared with Fe/Co-CNT, the bimetallic (Fe,Co)/CNT catalyst showed higher catalytic activity with $E_{1/2}$ of 0.954 V, E_{onset} of 1.15 V, and TOF of 0.105 s^{-1}. On the surface of (Fe, Co)/CNT, all the steps of ORR are exothermic (U = 0 V) at the Fe site. The ultimate potential of the exothermic process is 0.99 V, which is higher than that of the Co site (0.82 V). The results showed that the catalytic performance on Fe site is better than that on Co site in the (Fe,Co)/CNT catalyst. In addition, the linear relationship between ΔG_{OOH*} and ΔG_{OH*} leads to a theoretical limiting potential of 0.99 V, indicating that the active site is the Fe site in the $FeCoN_6$ structure. In the two-electron reduction pathway, the reduction of OOH* to OOH^- is an exothermic reaction, but at 0.99 V, it requires an absorption energy of 0.60 eV. All (Fe,Co)/CNT catalysts showed high selectivity in the catalytic four-electron ORR pathway (Fig. 10e-j) [113].

Bedford et al. used phenol formalde-hyde resin (PFR) spheres and NH_4Cl to enhance the active site of the reactants and prepared an atomically dispersed CoFe-NC. The CoFe-N_x sites were evenly distributed on the surface and inner wall of N-doped microporous carbon, so that the active sites can be fully contacted by the reactants. XAS results showed that the coordination of Fe and Co with nitrogen in the CoFe-NC catalyst is N_3Co-FeN_3. Theoretical calculation showed that N_3Co-FeN_3 is the active site of ORR, which showed excellent catalytic performance. The N_3Co-FeN_3 coordination structure rearranges the charge of the surrounding atoms, and the synergistic action of the double active sites weakens the oxygen–oxygen double bond and promotes the reactant activation. The strong molecular orbital interaction between the dimer Co-Fe and the substrate makes the oxygen containing substances have suitable adsorption energy on N_3Co-FeN_3, promoting the ORR [114]. Sun et al. synthesized an iron-cobalt-nitrogen-carbon material (f-FeCoNC) by solvothermal and pyrolysis strategies using formamide (FA) as C and N sources. The results of XAS spectra confirmed that the structure of f-FeCoNC contained Fe-Co dimer, and the structure of active site was deduced to be FeN_3-CoN_3 according to the coordination numbers of Co-N (2.8), Co-Fe (0.7), Fe-N (3.2) and Fe-Co (1.1). The catalyst showed excellent ORR activityunder alkaline conditions, with E_{onset}, and $E_{1/2}$ of 0.89 V, and the limiting current density of 5.75 mA cm^{-2} [115].

In addition to Co, Ni is Fe-like element in the periodic table and has similar physical properties, and therefore, it can produce synergistic effects with Fe in specific environments. Sun et al. synthesized a diatomic catalyst with FeNi-N_6 structure using a modified wet chemical

carbonization strategy. The $E_{1/2}$ of FeNi-N_6 catalyst is higher than that of single-atom Fe-N_4 and 20 wt% Pt/C catalyst, and the TOF (0.43 e site^{-1} s^{-1}) is much higher than that of Fe-N_4 (0.11 e site^{-1} s^{-1}). XAS showed that the active site structure of the synthesized FeNi-N_6 bimetallic catalyst is FeNi-N_6, in which Fe and Ni are coordinated with four N, and Fe is a trivalent state and Ni is a bivalent state. The local structure of FeNi-N_6 was verified by theoretical calculations, and the total coordination energy of single metal coordinated to three nitrogen atoms (1.44 eV) is lowered that single metal coordinated to four nitrogen atoms, indicating that the former structure is more stable. DFT calculation results showed that FeNi-N_6 is more favorable than Fe-N_4 and Fe_2-N_6 in the catalytic ORR. During the ORR process, the Bader charges of Fe, Ni and N in the FeNi-N_6 structure all changed, indicating that the whole structure site of FeNi-N_6 is involved in the catalytic process to regulate the thermodynamics and kinetics of ORR [116]. Liu et al. synthesized a porous nitrogen-doped carbon skeleton with atomically dispersed Fe and Zn diatoms (Fe-Zn-SA/NC), and EELS and XAFS results showed that there were isolated Fe-Zn pairs, which were bonded to six pyridine N. The Fe-Zn-SA/NC catalyst had excellent ORR catalytic activity in the whole pH range. The $E_{1/2}$ in 0.1 M $HClO_4$, 0.1 M KOH and 0.1 M PBS was 0.78, 0.85 and 0.72 V, respectively. Theoretical calculations showed that the low energy barrier of Fe-Zn-N_6 active site is conducive to improving the ORR activity. In addition, the porous nitrogen doped carbon skeleton provides more loading sites for the active sites to accelerate the electron transfer rate and improve the kinetics [117].

Zn porphyrin structure exists in the carbonic anhydrase with tetra coordination structure. Because the electronegativity of Zn is less than that of Fe and Co, when Zn and Co form atomic pairs, the outermost layer of Zn is more likely to lose electrons. The interaction of electronic structure can make the structure more optimized, which is conducive to the adsorption and desorption of reaction intermediates. Sun et al. used a competitive complexation strategy to introduce uniformly dispersed Zn/Co bimetallic sites (Zn/CoN-C) on N-doped carbon (Fig. 11a-d). The lattice defects (Fig. 11e) were due to the coordination of metal atoms with nitrogen. XAS results proved the existence of $ZnCoN_6$ structure in the Zn/CoN-C. Theoretical calculations showed that the O-O bond becomes longer (1.23 Å → 1.43 Å) after the adsorption of O_2 on the structure, which is easy to break, thus reducing the dissociation energy barrier. When $ZnCoN_6$ structure adsorbs *OH, the ORR path is $O_2 \rightarrow$ *O_2 → *OOH → *O → *OH → H_2O, and each step is a downhill reaction, and thus this process is a very stable exothermic process. Under alkaline conditions, the theoretical oxygen reduction overpotential on $ZnCoN_6$ is 0.335 V, which is lower than that of ZnN_4 (0.436 V) and CoN_4 (0.391 V) (Fig. 11f-n). The experimental results showed that the catalyst exhibited excellent ORR activity under acidic ($E_{1/2}$ = 0.796 V) and alkaline ($E_{1/2}$ = 0.861 V) conditions. In situ XANES analysis indicated that Co was the active center during ORR [33]. Table 2 shows the ORR performance comparison of carbon-based diatomic catalysts.

4.1.2.3. Co₂rr. The conversion of CO_2 into economically valuable chemicals and fuels by electrocatalysis can achieve sustainable development to a certain extent and promote the development of carbon cycle in closed technologies [20]. At present, electrocatalytic CO_2RR is inefficient in energy due to large overpotential and low selectivity and yield. Due to high molecular stability of CO_2, it is difficult to reduce two-electron CO_2RR to CO and HCOOH, six-electron CO_2RR to CH_3OH, eight-electron CO_2RR to CH_4 and the 12-electron CO_2RR to C_2H_5OH [122,123]. In addition, the equilibrium potential of electrocatalytic CO_2RR to various products in water environment is within the range of HER (±0.2 V), and thus the competitive HER seriously affects the selectivity of products. Therefore, it is urgent to develop high efficiency, low energy, high selectivity, and stable catalysts for the electrocatalytic CO_2RR. SACs have 100% of atom utilization, adjustable active centers, and high catalytic activity. DACs not only possess the characteristics of SACs, but also have the advantages of the synergy between adjacent
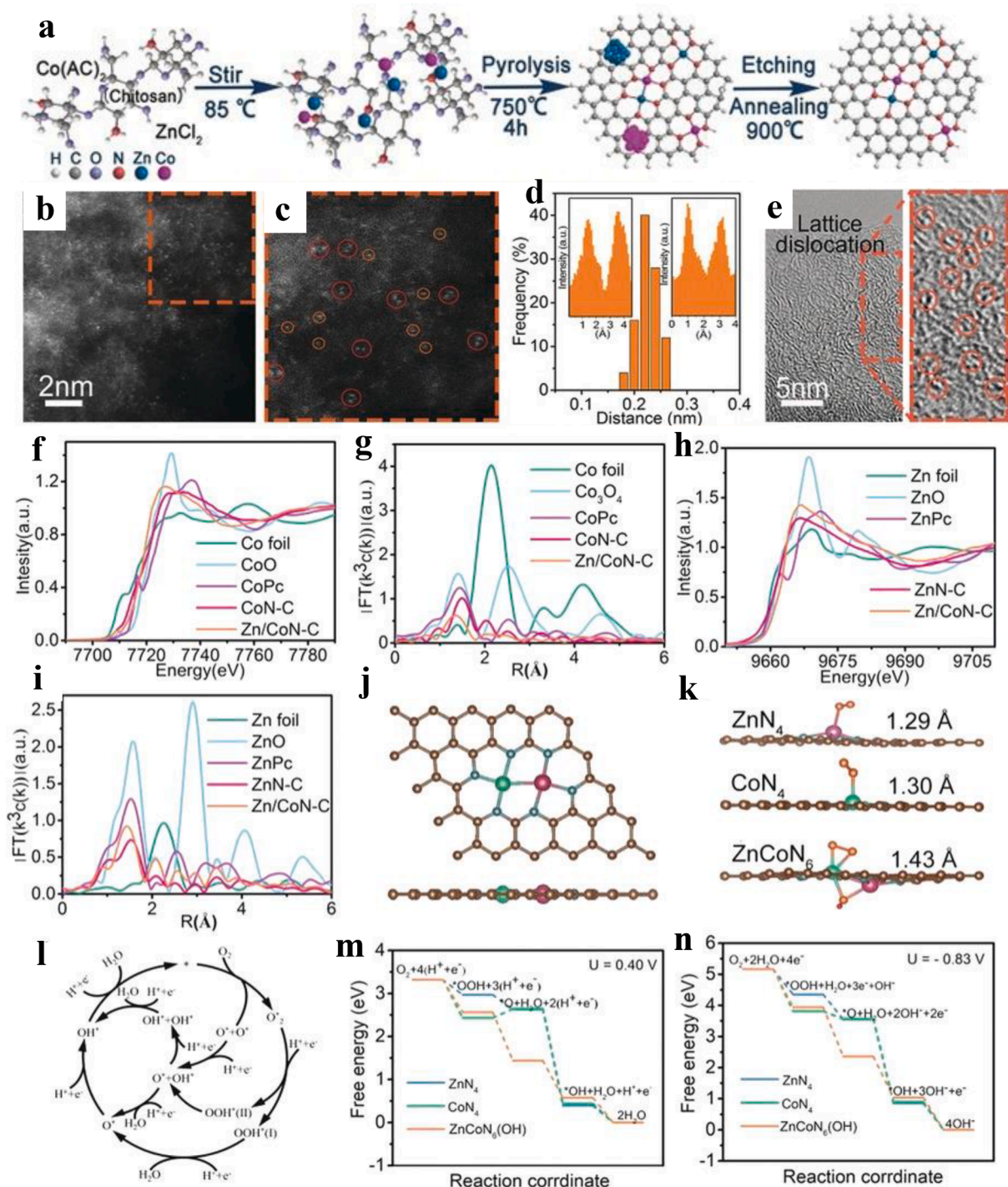
Fig. 11. (a) Illustration of the formation of Zn/CoN-C. (b) HAADF-STEM image and (c) enlarged image of the Zn/CoN-C. (d) Statistical Zn-Co distance. (e) HRTEM of Zn/CoN-C. (f) Co K-edge XANES and (g) FT-EXAFS spectra. (h) Zn K-edge XANES and (i) FT-EXAFS spectra. (j) Relative position of Zn, Co, and N for the Zn/CoN-C (k) Optimized geometry of O_2 adsorption configuration. (l) Free-energy profiles in acidic conditions. (m, n) Free energy diagram under acidic and alkaline conditions at U = 0.40 and U = 0.83 V, respectively. Reproduced with permission.[33] Copyright 2019, Wiley-VCH Verlag GmbH & Co. KGaA, Weinheim.

metal sites [124-126]. The selectivity of catalytic CO_2RR can be improved by adjusting the coordination surroundings of active sites.

At present, DFT has been widely used to study the mechanism of CO_2RR. Lu et al. constructed diatomic FeCo-NC and single-atom Fe/Co-NC models, and found that the diatomic structure was stable, and the catalytic activity was higher than single-atom Fe/Co-NC due to the appropriate interaction between the diatomic center and N coordination. CO_2 can only be reduced to CO through the two-electron pathway on single-atom Fe/Co-NC catalysts, and the high limit potential (−1.22

$\sim$ − 1.67 V) inhibits further reduction, while on the diatomic FeCo-NC, CO_2 can be reduced to methanol and methane by 6-electron and 8-electron pathways, and the RDS is *CO→*CHO. The CO intermediate can assist the reaction and reduce the reaction energy. The limit potential of methanol and methane formation is − 0.64 V. The essence of improving structural stability and catalytic activity is that the diatomic active center can provide greater spin polarization and multi-electron transfer ability, which is conducive to the CO intermediate as an electronic and geometric auxiliary agent in the CO_2RR [127]. Shi et al. used theoretical

Table 2
Comparison of ORR performance on carbon-based diatomic catalysts.

Catalyst	Active site	Electrolyte	Onset potential E_{onset} [V]	Half-wave potential $E_{1/2}$ [V]	Ref.
CoNi-SAs/NC	CoNi- N_6	0.1 M KOH	0.88	0.76	[102]
Fe–NiNC-50	FeNi- N_6	0.1 M KOH	0.86	0.75	[101]
IrCo–N–C	IrCoN$_5$–Co	0.1 M KOH	1.00	0.911	[100]
Fe$_2$–N–C	Fe$_2$–N_6	0.1 M KOH	–	0.905	[78]
A-CoPt-NC	Co–Pt@N_8V_4	0.1 M KOH	–	0.96	[109]
Fe − Se/NC	Fe − Se	0.1 M KOH	1.05	0.925	[118]
(Fe,Co)/CNT	FeCo-N_6	0.1 M KOH	1.15	0.945	[113]
(Zn, Co)/NSC	ZnCo/NC(OH)	0.1 M KOH	1.07	0.845	[119]
Zn/CoN-C	ZnCoN$_6$(OH)	0.1 M KOH	1.004	0.861	[33]
f-FeCoNC900	Fe(N_3)–Co(N_3)	0.1 M KOH	1.05	0.89	[115]
f-FeCoNC900	Fe(N_3)–Co(N_3)	0.1 M HClO$_4$	0.87	0.81	[115]
Co/Zn–NCNF	CoZnN$_6$	0.1 M HClO$_4$	0.997	0.797	[120]
FeCoN$_5$–OH	FeCoN$_5$–OH	0.1 M HClO$_4$	1.02	0.86	[121]
FeNi–N_6–C	FeNi–N_6	0.1 M HClO$_4$	–	~0.8	[116]
(Zn, Co)/NSC	ZnCo/NC(OH)	0.5 M H$_2$SO$_4$	0.93	0.70	[119]

calculations to construct models with diatomic metal sites on monolayer carbon nitride, and found that RuCu@g-CN and RuFe@g-CN have lower limiting potentials in CO$_2$RR. At a certain potential, the selectivity of CH$_4$ is significantly higher than that of H$_2$, which is due to the different affinity of different metal atoms to O and C, and the synergistic effect on the adsorption sites, thus improving the catalytic activity [128].

Lu et al. used theoretical calculations to reveal the formation of methanol and methane via multi-electron CO$_2$RR processes on Cu/Fe-NC with a diatomic central site [129]. The Cu/Fe-NC and Ni/Fe-NC models were constructed and the bond lengths were optimized. The results showed that the diatomic Cu-Fe interacts strongly with the adjacent N, and the distance between Cu-Fe is 2.39 Å. The interconnection between them is conducive to the adsorption and electron transfer of the bimetallic active site. The formation energy (E_f) of Ni/Fe-NC (-1.10 eV) and Cu/Fe-NC (-0.90 eV) is less than zero, indicating that they have good thermodynamic stability. In addition, the dissolution potentials (U_{diss}) of different metals were greater than the working potentials of CO$_2$RR, indicating that the electrochemical CO$_2$RR processes at these active sites exhibited stable resistance to dissolution (Fig. 12a-d). Fig. 12e-h shows the path diagram and free energy diagram of CO$_2$ reduction to C1 product on Cu/Fe-NC, where CO$_2$ can be reduced to CO and HCOOH through the two-electron pathway, methanol through the six-electron pathway, and methane through the eight-electron pathway. The limiting potential of CO$_2$RR to HCOOH (-0.42 V), CH$_3$OH (-0.51 V) and CH$_4$ (-0.51 V) is significantly higher than that of CO (-1.18 V), and the strong adsorption capacity of CO improves the selectivity. In the diatomic site, Fe acts as the active site and Cu acts as the activity promoter, which not only improves the activity of Fe but also enhances the adsorption capacity, which is conducive to the occurrence of multi-electron paths.

Compared with C1 product, the reduction of CO$_2$ to C2 product is relatively difficult and the main catalysts include Cu-based catalysts and their derivatives. In addition, nitrogen doped carbon materials with bimetallic sites are conducive to the catalytic reaction due to the synergistic interaction between metals. To find a catalyst with low limiting potential and high activity for the reduction of CO$_2$ to C2 products, Singh et al. discussed the limiting potential and C-C coupling processes for the formation of C$_2$H$_4$ and C$_2$H$_5$OH from CO$_2$RR on 21 DACs with stable structures. To realize the binding of the second CO in the geometric structure of DAC, *CO should be formed first, which then undergoes a series of hydrogenation processes or combines with the second CO to finally obtain C1 and C2 products (Fig. 12i-j). Six diatomic sites with high activity and low limiting potential, Cr-Cu (0.58 V), Mn-Cu (0.75 V), Co-Co (0.45 V), Co-Ni (0.78 V), Co-Cu (0.65 V) and Ni-Cu (0.80 V), were screened by comparing the limiting potential and the energy barrier of C-C coupling. These catalysts showed excellent thermal

stability and almost negligible structural deformation (Fig. 12k) [130]. An et al. used DFT calculations to study seven homonuclear and heteronuclear diatomic catalysts (M$_2$@C$_2$N) loaded onto C$_2$N, and found that the N$_2$M$_2$N$_2$ active site and the C$_2$N substrate play a significant synergistic role in activating C = O bond in CO$_2$. The Fe-Fe, Fe-Co, Fe-Ni and Fe-Cu diatomic sites tend to form C$_2$H$_4$, while the Cu-Co, Cu-Ni and Cu-Cu sites favor the formation of CH$_4$. *CO + *CO co-strength favors the reduction of CO$_2$ to C2. In addition, the results showed that C affinity is conducive to C-C coupling and the formation of C$_2$H$_4$, while C and O affinity favors the formation of CH$_4$ [131].

The plane and conjugated carbon structures of MOF derivatives are advantageous to the long-range electron delocalization and adjacent non-bonding metal atoms coupling, thus affecting the charge distribution of the active center, and optimizing the free energy barrier. Jiang et al. used atomization strategy to anchor single-atom Fe and Ni onto MOF-derived nitrogen-doped carbon (Fe$_1$-Ni$_1$-N-C). The microstructure of Fe$_1$-Ni$_1$-N-C shows polyhedral morphology, and Ni and Fe are uniformly dispersed, and the atomic distance is around 4.1 Å, which indicates that there are single atom pairs in Fe$_1$-Ni$_1$-N-C. Due to the long-range electron interaction between atomic pairs, Fe$_1$-Ni$_1$-N-C showed FE$_{CO}$ of 96.2% in the CO$_2$RR. DFT calculation results showed that Ni can activate the surrounding Fe single atom by non-bonding interaction, reduce the energy barrier of COOH* intermediate, and accelerate the process of CO$_2$RR (Fig. 13a-f) [132]. Zhao et al. obtained a nitrogen-coordinated isolated diatomic Ni-Fe catalyst (Ni/Fe-N-C) by pyrolysis of iron and nickel co-doped MOF precursor [133]. The average valence state of Ni is between 0 and + 2, and the 3d and 4p orbitals of Ni are hybridized. The distortion of D$_{4h}$ symmetry in Ni/Fe-N-C is due to M−N coordination (1.30 Å) and M−M coordination (2.06 Å), confirming the existence of Ni-Fe coordination. The structure of the active site was deduced to be N$_3$-Fe-Ni-N$_3$ by theoretical simulations. Ni/Fe-N-C catalyst showed more than 90% FE$_{CO}$ in a wide potential range (-0.5 - −0.9 V), and the FE$_{CO}$ was up to 98% at −0.7 V. Only 1% of the initial selectivity lost after 30 h. The Tafel slope of Ni/Fe-N-C (96 mV dec^{-1}) revealed that the RDS is the formation of surface *COOH intermediate. According to the Gibbs free energy diagram, the CO$_2$(g) → COOH* (0.47 eV) and CO* → CO(g) (0.27 eV) energy barriers of COOH* and CO* co-adsorbed on Ni/Fe-N-C catalysts are lower than those on bare Ni/Fe-N-C and monmetallic Ni/Fe catalysts. In the CO$_2$RR, the strongly bonded CO* will first passivate the Fe-Ni double site, and then the reaction occurs at the Fe site. The competitive HER was inhibited in the Ni/Fe-N-C catalyst. Although the Ni-N-C catalyst also showed a good inhibitory effect on HER, the Ni-N-C catalyst blocked the reaction in the first proton-coupled electron transfer step in the CO$_2$RR. Therefore, the Ni/Fe-N-C catalyst had higher CO$_2$RR selectivity than the single-atom Fe-Ni catalyst (Fig. 13g-k). Therefore, the synergistic effect of Ni-Fe
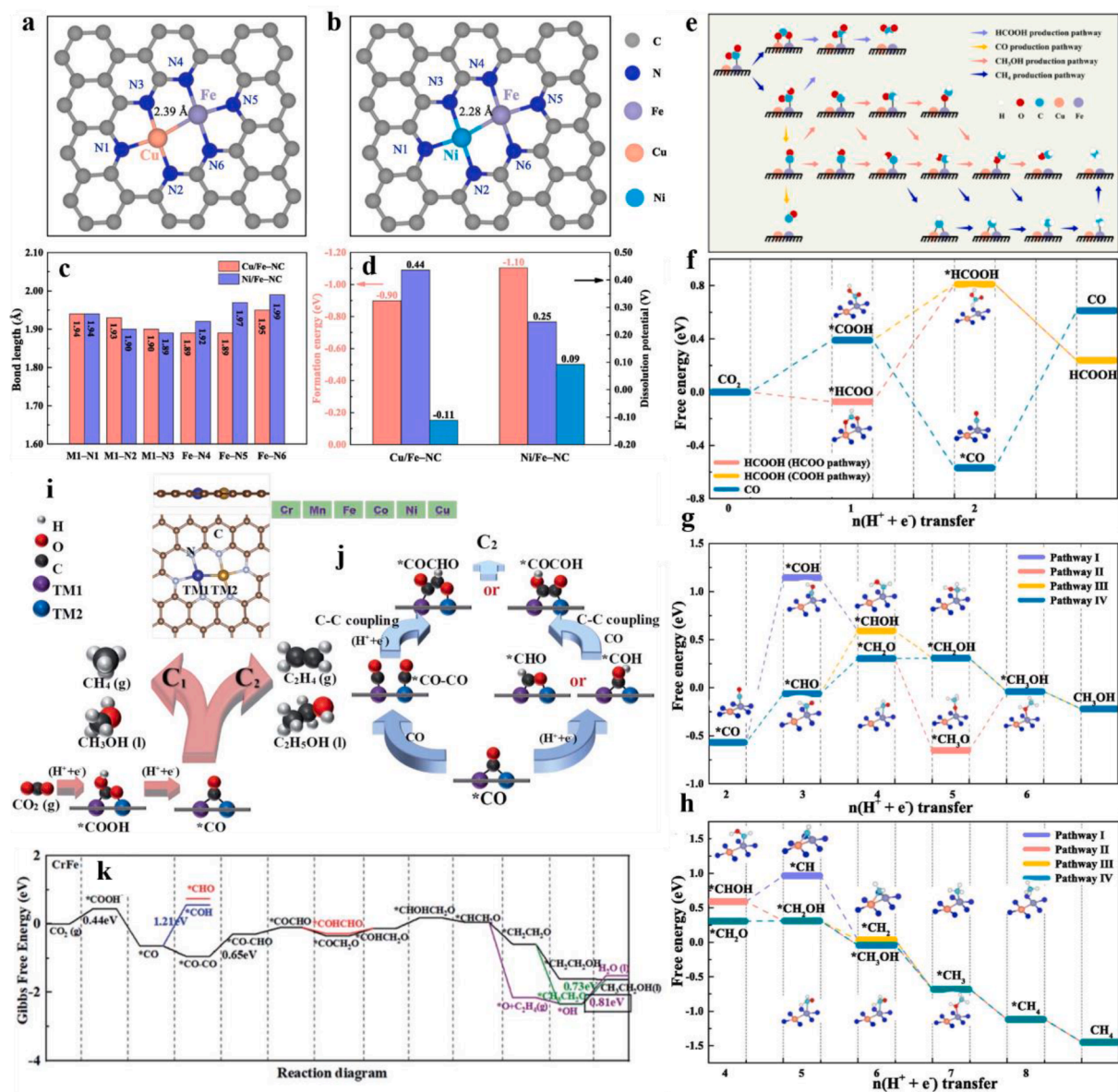
Fig. 12. Optimized structures of (a) Cu/Fe-NC, and (b) Ni/Fe-NC. (c) Bond lengths of M − N in Cu/Fe-NC and Ni/Fe-NC. (d) Formation energy and dissolution potential. (e) Detailed pathways of CO$_2$RR. Free energy diagram of CO$_2$RR to (f) CO and HCOOH, (g) CH$_3$OH, and (h) CH$_4$. (g) Geometric structure of N-graphene based DACs and general process of CO$_2$ reduction to various C1 and C2 products. (h) Two general pathways from *CO to C2 related adsorbed intermediates. (i) The reaction diagrams for CO$_2$ reduction. (a-h) Reproduced with permission.[129] Copyright 2021, Elsevier B.V. (i-k) Reproduced with permission.[130] Copyright 2020, The Royal Society of Chemistry.

bimetallic sites reduces the energy barrier for forming COOH* intermediates and desorbing CO and can effectively inhibit the process of HER.

In diatomic catalysts, the introduction of bimetallic atoms leads to electron rearrangement, which optimizes the adsorption energy of reaction intermediates. Ni-based and Cu-based single-atom catalysts have lower energy barriers for the CO desorption in the catalytic CO$_2$RR, but they usually have higher initial potentials. He et al. used MOF to assist the controllable preparation of nitrocarbon-rich materials with Ni/Cu bimetallic sites (Ni/Cu − N − C). The catalyst showed excellent selectivity in catalyzing CO$_2$RR, and the FE$_{CO}$ was higher than 95% (−0.39 - −1.09 V). Theoretical calculation results showed that Ni-N and Cu-N sites optimize the electronic structure and bandgap width, and then increase the electrical conductivity. The introduction of Cu single atom promotes the interaction between *COOH intermediate and Ni site, reduces the energy barrier of the reaction process, and is conducive to the formation of CO [134]. Lu et al. used competitive complexation to

synthesize atomically dispersed Ni-Zn bimetallic site catalysts. The coordination of heteronuclear atoms can optimize the d-state of metal atoms and adjust the position of d-band center and Fermi level, which is beneficial to the electron interaction at the interface, reduce the reaction energy barrier, facilitate the adsorption of reaction intermediates, and accelerate the reaction kinetics. The experimental results showed that the Ni-Zn bimetallic catalyst had high FE$_{CO}$ (>90%) in the range of −0.5 - −1.0 V [135]. Table 3 shows the performance comparison of carbon-based diatomic catalysts for the CO$_2$RR.

4.1.2.4. Nrr. Nitrogen mainly exists in the atmosphere in the form of gaseous state, which plays an important role in modern agriculture and chemical industry. However, the stable N≡N triple bond is difficult to activate. In the biological world, nitrogen can be converted to ammonia through nitrogen fixation. The Haber-Bosch process was proposed to convert nitrogen and hydrogen gas to ammonia in industry under high
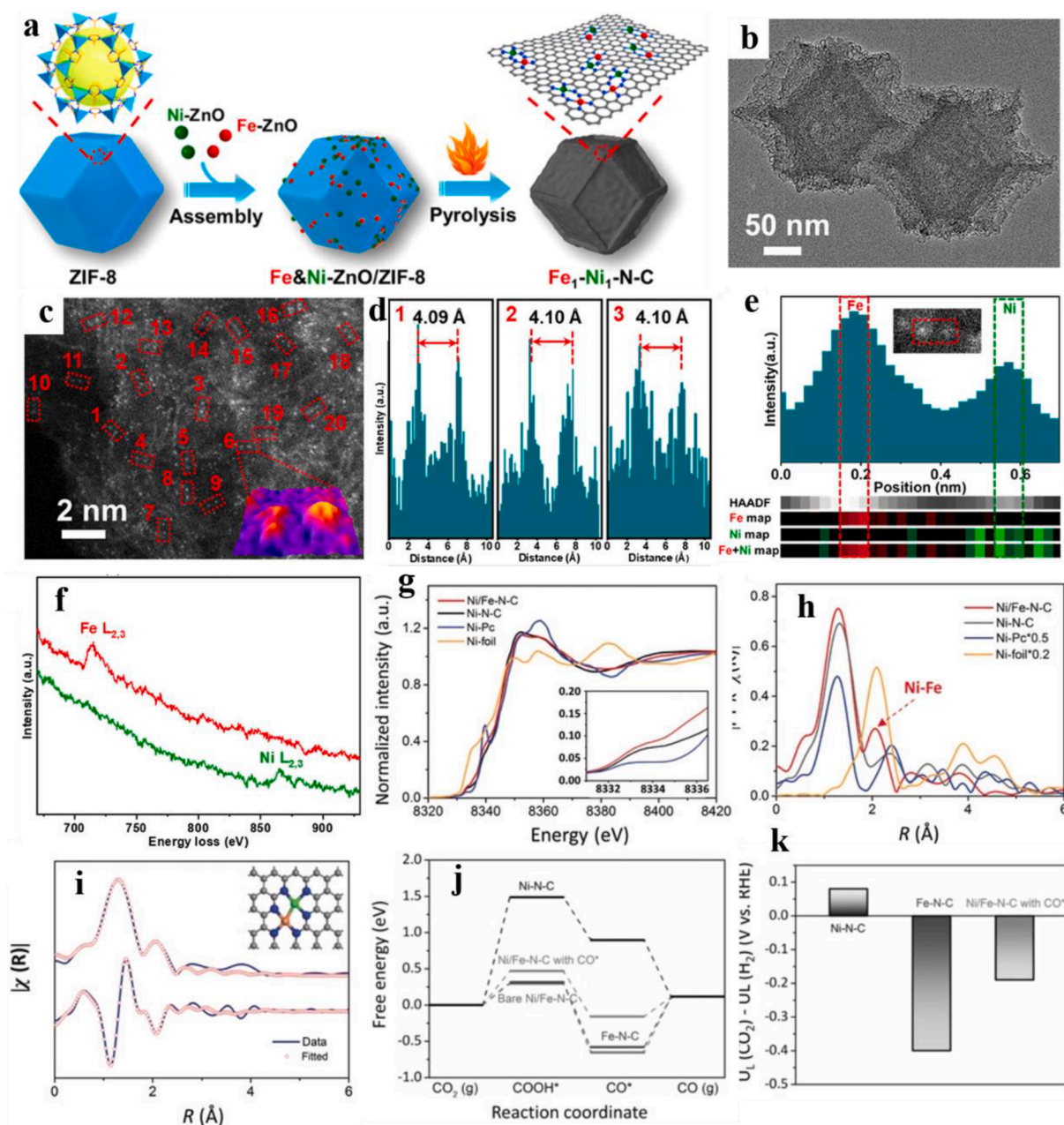
Fig. 13. (a) Schematic illustration for construction of Fe₁-Ni₁-N-C. (b) TEM. (c) HAADF-STEM. (d) Line-scanning intensity profiles obtained from the region 1–3 highlighted in panel c. (e) Simultaneously acquired HAADF-STEM image intensity profile accompanied by atomic-resolution EELS mapping of the Fe − Ni pair presented in panel e. (f) EELS spectra extracted from two atomic positions highlighted in red and green in panel e. (g) Ni K-edge XANES spectra. (h) FT-EXAFS spectra at R space. (i) The first two shell (Ni-N, Ni-Fe) fittings of the FT-EXAFS spectra for Ni/Fe-N-C. (j) Calculated free energy diagrams. (k) Difference in limiting potentials for CO₂ reduction and H₂ evolution. (a-f) Reproduced with permission.[132] Copyright 2021, American Chemical Society. (g-k) Reproduced with permission.[133] Copyright 2019, Wiley-VCH Verlag GmbH & Co. KGaA, Weinheim.

Table 3
Comparison of CO$_2$RR performance on carbon-based diatomic catalysts.

Catalyst	Active site	Electrolyte	Product	FE (%)	TOF (s^{-1})	Ref.
Ni/Fe–N–C	Fe/Ni–N₄	0.5 M KHCO₃	CO	98	2.1	[133]
Ag₂-G	AgN₃-AgN₃	0.5 M KHCO₃	CO	93.4	30	[55]
Pd₂DAC	PdN₂O₂	0.05 M KHCO₃	CO	98.2	–	[56]
Fe₂–N–C	Fe₂–N₆	0.5 M KHCO₃	CO	80	7.4	[81]
Ni/Cu–N–C	N₄Ni/CuN₄	0.5 M KHCO₃	CO	99.2	1.1	[134]
Fe/Cu–N–C	N₄Fe–CuN₃	0.5 M KHCO₃	CO	99.2	1.4	[136]

temperature and pressure. The harsh conditions consume a lot of energy, and a lot of carbon monoxide emits. Inspired by natural biological nitrogen fixation, more and more people pay attention to the electrocatalytic NRR with mild conditions. The current challenge of electrocatalytic NRR is to design efficient and economical catalysts to activate inert molecular nitrogen. SACs play a great role in improving the performance of NRR due to their 100% atom utilization efficiency and unique coordination structure. For example, Ru [137,138], Mo [139], Fe [140-142], Au [143], Cu [144] and Ag [145] have been used in electrocatalytic NRR. However, to break N≡N bond, the catalyst needs strong N_2 adsorption energy and low activation energy of the first proton-coupled electron transfer step [144,146]. In addition, HER is very competitive in the reaction, and most protons and electrons are inclined to HER, which makes it difficult to improve the Faraday efficiency of NRR [147].

To solve these problems, highly active and durable catalysts have been purposefully synthesized. An ideal NRR catalyst requires strong adsorption of N_2^* and weak adsorption of NH_2^*. Therefore, a catalyst with two active sites can meet the above conditions by adsorption from the strong side of N. Compared with SACs, DACs have variable active centers and can adsorb reactants and intermediates with different configurations and energies. Luo et al. synthesized a nitrogen-coordinated iron and molybdenum diatomic catalyst (FeMo@NG) with a well-defined location using template sacrifice method [148]. The catalyst exhibited a typical graphene-like sheet morphology, and no nanoparticles were observed (Fig. 14a-b). The low-voltage spherical aberration-corrected transmission electron microscopy (LVACTEM) image showed single metal atoms anchored to the N-doped graphene, which appear brighter than C atoms (Fig. 14c). As shown in Fig. 14 d, FeMo dimer was successfully synthesized in the FeMo@NG. The FeMo@NG catalyst exhibited excellent nitrogen catalytic selectivity and kinetics by regulating the electron configuration and geometry in the presence of FeMo dimer species. The NRR catalytic performance of MoFe@NG was evaluated by LSV in Ar and N_2. At low voltage, the response current density curve in N_2 was higher than that in Ar, and with the increase of potential, competitive HER dominated the electrochemical reaction. The LSV curve showed that the diatomic MoFe@NG catalyst was more favorable to catalyzing NRR than the monatomic Fe@NG and Mo@NG catalysts, showing the highest yield of 14.95 $\mu g \cdot h^{-1} mg^{-1}$ at -0.4 V and 41.7% FE at -0.2 V (Fig. 14e-i). The NRR
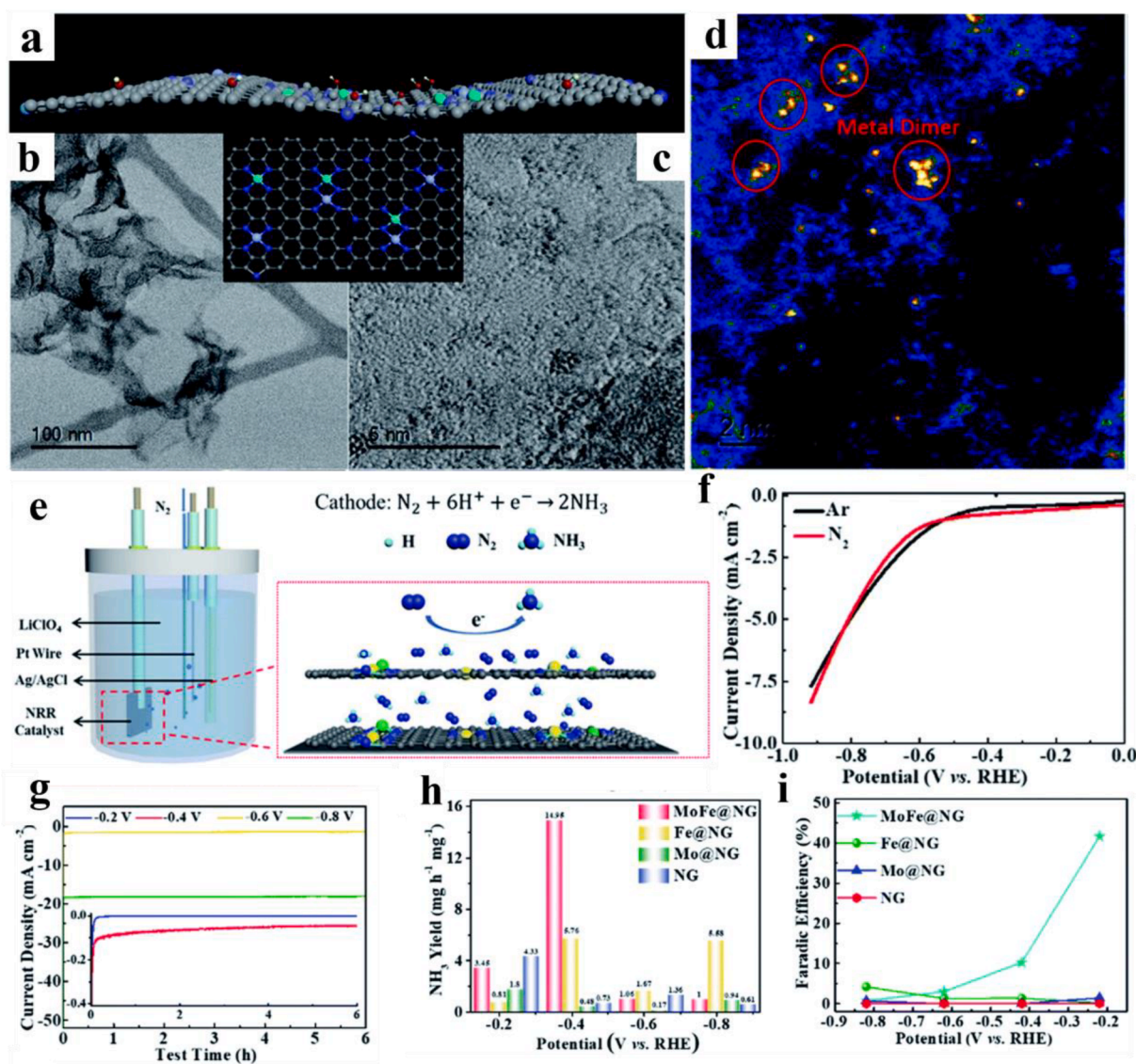

Fig. 14. (a) Schematic illustration of the MoFe@NG. (b) TEM image. (c) LVACTEM image; and (d) HAADF-STEM images. (e) Schematic illustration of the electrocatalytic reactor for N_2 conversion to NH_3. (f) LSV curves. (g) Chronoamperometric curves. (h) NH_3 yield rates and (i) the faradaic efficiencies on MoFe@NG, Fe@NG, Mo@NG, and NG at different potentials. Reproduced with permission.[148] Copyright 2019, The Royal Society of Chemistry.

path at FeN_4, MoN_4 and $FeMoN_6$ sites was simulated by theoretical calculations. The adjacent Fe and Mo atoms played an important role in the polarization and activation of N_2. The Gibbs free energy is -0.14 eV, much higher than that on FeN_4 (-0.84 eV) and MoN_4 (-2.39 eV). $FeMoN_6$ site can weaken the reaction intermediate NN*, which is conducive to continued hydrogenation. The reaction on $FeMoN_6$ takes place through an alternating mechanism, where *NNH converting to *NNH_2 and *HNNH has the same ΔG (-1.2 eV), while the ΔG of *HNNH → *$HNNH_2$ (-1.32 eV) is lower than that of *NNH_2 → *N (-0.74 eV), implying that $MoFeN_6$ is more suitable for the alternating pathway. At $FeMoN_6$, the dissociation of NH_3 is the RDS (0.906 eV), which is much lower than the energy barrier of the RDS of N_2 activation at FeN_4 (1.634 eV) and the RDS of NH_3 generation at MoN_4 (2.036 eV). These results suggest that MoFe@NG with FeMo dimer species can effectively catalyze NRR by using distal binding, alternate mechanism, and dissociation pathways.

For the activation of inert N_2 molecules, the electronic structure of the active site needs to be optimized by rationally designing NRR catalysts. Due to the good electrocatalytic performance of Zn and Fe SACs and the different electronegativity between them, Zn can give the outer electrons to Fe in Zn-Fe diatomic configuration, thus optimizing the electronic structure of Fe and making Fe site have excellent catalytic activity. Cheng et al. reported a diatomic catalyst Zn/Fe-N-C anchoring isolated bimetallic Zn-Fe sites on a nitrogen-doped carbon substrate [149]. In the Zn/Fe-N-C catalyst, Zn and Fe existed in the form of atoms. According to the HAADF-STEM image, bright Zn and Fe were evenly distributed on the whole material, with an average distance of 2.24 Å (Fig. 15a-d). Zn/Fe-N-C catalysts showed high NRR activity with the maximum yield of NH_3 of 30.5 µg·h^{-1} mg^{-1}, high selectivity with FE of 26.5%, and high stability. DFT study showed that the active site of Zn/Fe-N-C catalyst was $ZnFeN_6$, on which N_2 was adsorbed in the end-face adsorption mode with relatively low energy, and Fe atom acted as the active site. The difference in charge density of *NN intermediate is since N≡N exhibits higher elongation due to the electron donation of Zn in Zn/Fe-N-C coordination. Due to the synergistic action between Zn and Fe, the d-band center of Fe in Zn/Fe-N-C is closer to the Fermi level. In addition, compared with single-atom Fe-N-C (1.27 eV) and Zn-N-C (1.78 eV) catalysts, the Gibbs free energy of the first proton-coupled electron transfer step on the Zn/Fe-N-C (0.79 eV) is the lowest (Fig. 15e-g). Therefore, the configuration of $ZnFeN_6$ atoms is conducive to the fixation and activation of nitrogen, thus promoting the NRR.

In addition to experiments, efficient catalytic NRR structures can be screened out with the help of theoretical calculations. The synergistic effect of dual active sites can break through the activity of single metal sites, and an asymmetric adsorption site can be formed by pairing the 3d, 4d, and 5d elements with the main group metals. Wang et al. investigated NRR by constructing doner-recipient pairs of bimetallic sites. Twenty-eight M_1M_2/g-C_3N_4 heteronuclear DACs were selected to evaluate their NRR performance [150]. After optimizing their structures, FeMo, TiMo, MoW and NiMo dimers were selected as promising NRR catalysts. Further studies showed that FeMo/g-C_3N_4 had stable structure and showed high NRR activity and selectivity. The limit potential was only -0.23 V in NRR, but a very high limit potential (-0.79 V) was observed for competitive HER. The synergistic effect of bimetal not only acts as an active site, but also provides a suitable reaction environment for NRR by regulating the electronic structure. This strategy can also be extended to other substrate environments, such as graphene, providing directions for efficient preparation of NRR catalysts. Using the design principles of descriptors, Huang et al. constructed a series of DACs with stable structures on 2D expanded phthalocyanine (Pc) using DFT calculations. The competitive HER significantly affected the selectivity and activity of NRR. TiV-, VCr- and VTa-Pc DACs inhibited HER effectively, and the limiting potentials were -0.74, -0.85 and -0.47 V, respectively [87]. Nitrogen-doped graphene is often used as a carrier for electrocatalysts due to its high carrier density, mobility and low resistance, and the N-doping site facilitates the binding of metal atoms for controlled synthesis. Based on the above advantages, Jiang et al.

constructed transition metal TM dimer onto N-doped graphene to study the effect of bimetallic active sites on the catalytic performance of NRR. The results of DFT study showed that under the synergistic action of suitable diatoms, the adsorption configuration of reaction intermediates could be adjusted to improve the activity, among which VFe-N-C showed the best catalytic activity of NRR with the limit potential of -0.36 V because the electrostatic interaction between the positively charged transition metal and the proton in the diatomic configuration inhibits HER and improves the selectivity of NRR [151]. Du et al. constructed catalysts with asymmetric bimetallic dimers using theoretical calculations. DFT calculations showed that the Mo-Ru, Mo-Co, Mo-W, Mo-Fe, and Fe-Ru dimers can reduce the free energy barrier of the initial step of NRR, and the initial potentials were as low as -0.17, -0.27, -0.28, -0.36 and -0.39 V, respectively. In addition, the by-product H_2 in NRR is well inhibited since N_2 is highly polarized and weakened by unidirectional charge transfer on the asymmetric bimetallic dimer structure, and N≡N bond accepts different electrons from the asymmetric structure. In addition, the interaction between bimetals can change the d-band center of metal atoms, thus regulating the adsorption strength of reaction intermediates, which is conducive to the NRR [152]. Jia et al. used DFT to study the catalytic ability of NRR by anchoring heteronuclear FeM and NiM (M = Ti, V, Cr, Mn, Fe, Co, Ni and Cu) dimers to graphdiyne (GDY) monolayer and found that heteronuclear diatomic FeCo@ and NiCo@GDY catalysts had higher activity and selectivity than homonuclear Fe_2@GDY and Co_2@GDY [153], which may be attributed to the regulation of the d band by heteronuclear atoms. The above results show that the asymmetric environment and the support play an important role in DACs, which can provide help for further theory and experiment. Table 4 shows the DFT-predicted NRR performance on carbon-based diatomic catalysts.

4.2. Regulating the local coordination environment of bimetallic central atoms

The enhanced chemical interaction between adjacent atoms and the adjustable electronic environment of DACs can further improve the intrinsic activity and stability of electrocatalytic reactions and effectively prevent the aggregation of individual species. Compared with SACs, DACs can be regulated in a larger range, and thus the regulation of electronic structure and coordination environment can be maximized to improve atomic utilization and catalytic activity. The coordination environment and type of the active site will restrict the diversity and efficiency of catalytic reactions to a certain extent. By adjusting the coordination structure of the active site, catalysts with high electrocatalytic activity can be designed to a certain extent. In carbon-based diatomic catalysts, metal atoms usually coordinate with nitrogen, and the coordination number of nitrogen affects the distribution of electrons at the active site, thus affecting the catalytic efficiency. In addition to N, oxygen atom is also coordinated with bimetal atoms to form a bridge dimer. In the synthesized carbon-based materials, bimetallic atoms usually coordinate with six N atoms, presenting a *para*-link. By controlling the synthesis conditions, Han et al. synthesized a diatomic iron site catalyst with two irons in orthogonal positions coordinating with six N (Fe_2-N_6-C-o) [81]. The well-dispersed pairs of atoms are clearly seen by HAADF-STEM, corresponding to the bimetallic Fe, and their mean distance is 2.37 ± 0.31 Å (Fig. 16a-f). XPS analysis showed that N in Fe_2-N_6-C-o is mainly pyridine nitrogen and pyrrole nitrogen, which is different from the synthesized para diatomic iron site catalyst (Fe_2-N_6-C-p). There is more graphite nitrogen in Fe_2-N_6-C-p, because H_2 can change the N species in the synthesis process. In the annealing process, pyridine nitrogen and pyrrole nitrogen are unstable, which are prone to etch. The results of XAS analysis showed that the corresponding peak of Fe-Fe was observed, which indicates that dimer iron rather than iron nanoparticles were formed in the Fe_2-N_6-C-o. In addition, the valence state and charge analysis showed that Fe has different valence states in Fe_2-N_6-C-o and Fe_2-N_6-C-p, and the former is higher than the latter,
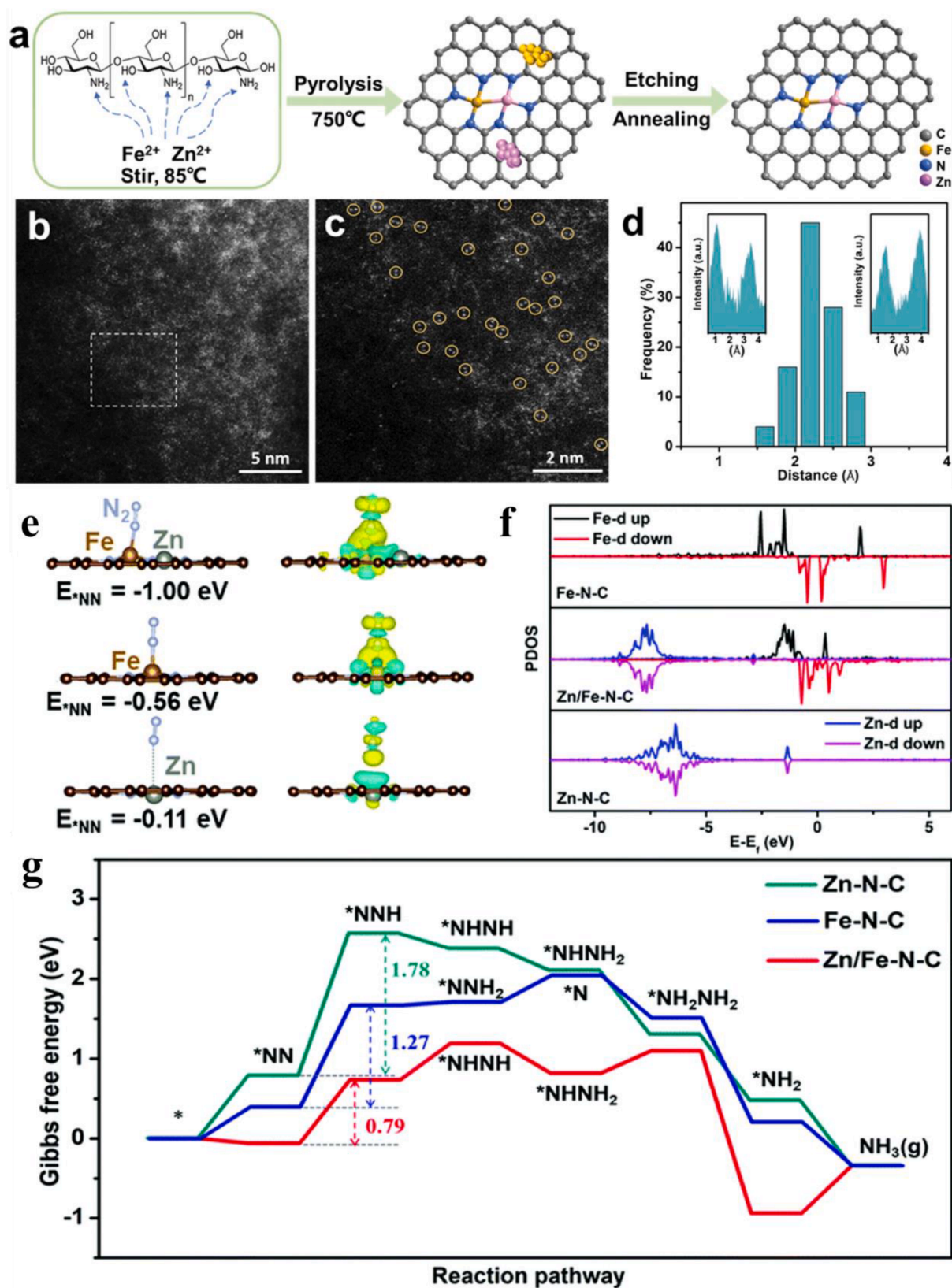
Fig. 15. (a) Synthetic illustration of Zn/Fe–N–C. HAADF-STEM image (b) and enlarged image (c) of Zn/Fe–N–C. (d) Statistical Zn–Fe distance in the observed diatomic pairs. (e) Optimized geometry and the charge density difference of the N_2-adsorbed configuration via the end-on mode. (f) Projected density of states (PDOS). (g) Gibbs free energy profiles. Reproduced with permission.[149] Copyright 2020, The Royal Society of Chemistry.

Table 4

DFT-predicted NRR performance on carbon-based diatomic catalysts.

| Systems	Best sample	Theoretical limiting potential U_L[V]	Pathway	PLS	Ref.
TM$_2$@C$_2$N (TM = Ti, Mn–Co, Cu, Mo, Ru–Ag, Ir–Au)	Mo$_2$@C$_2$N	−0.41	Distal	*NH → *NH$_2$	[86]
TM − N − C (TM = Ti, V, Mo, Mn and Fe)	VFe − N − C	−0.36	Distal	NNH* → NHNH*	[151]
M1M2@NG (TM = V-Cu)	VCr@NG	−0.24	Mixed	*NH$_2$ → *NH$_3$	[154]
TM$_2$@C$_2$N (TM = Cr–Ni)	Mn$_2$@C$_2$N	−0.23	Enzymatic	*NH–*NH$_2$ → *NH$_2$–*NH$_2$	[85]
TM$_2$@graphdiyne (TM = Mn–Ni)	Co$_2$@graphdiyne	−0.43	Distal	*NH$_2$ → *NH$_3$	[155]
Fe$_2$@C-DV/G, N-DV/G, g-C$_3$N$_4$, GDY	Fe$_2$@g-C$_3$N$_4$	−0.32	Enzymatic	*N$_2$ → *N$_2$H	[156]
TM$_1$TM$_2$@N-doped porous graphene	FeRh@N-doped porous graphene	−0.22	Distal	*N$_2$ → *N$_2$H	[157]
M$_1$M$_2$N$_6$-NG	MoRuN$_6$-NG	−0.17	Enzymatic	*N$_2$ → *N$_2$H	[152]
M$_2$-phthalocynine (Pc) or MM′-Pc	V$_2$-Pc	−0.39	Mixed	*NH$_2$ → *NH$_3$	[87]
M$_1$M$_2$-XG (X = C, N, O, P, S)	TiV-CG	−0.30	Enzymatic	*NH$_2$-NH$_3$ → *NH$_3$	[158]
TM$_2$@C$_2$N (TM = Sc–Zn, Y–Cd, La–Au)	Cr$_2$@C$_2$N	−0.50	Enzymatic	*N$_2$ → *N$_2$H	[159]
FeM@ GDY (M = Ti–Cu)	FeCo@ GDY	−0.44	Distal	*NH$_2$ → *NH$_3$	[153]
NiM@GDY (M = Ti–Cu)	NiCo@GDY	−0.36	Distal	*N-N → *N-NH	[153]
TM$_2$N$_4$@graphene	Fe$_2$N$_4$@graphene	−0.32	Distal	*N$_2$ → *NNH	[160]
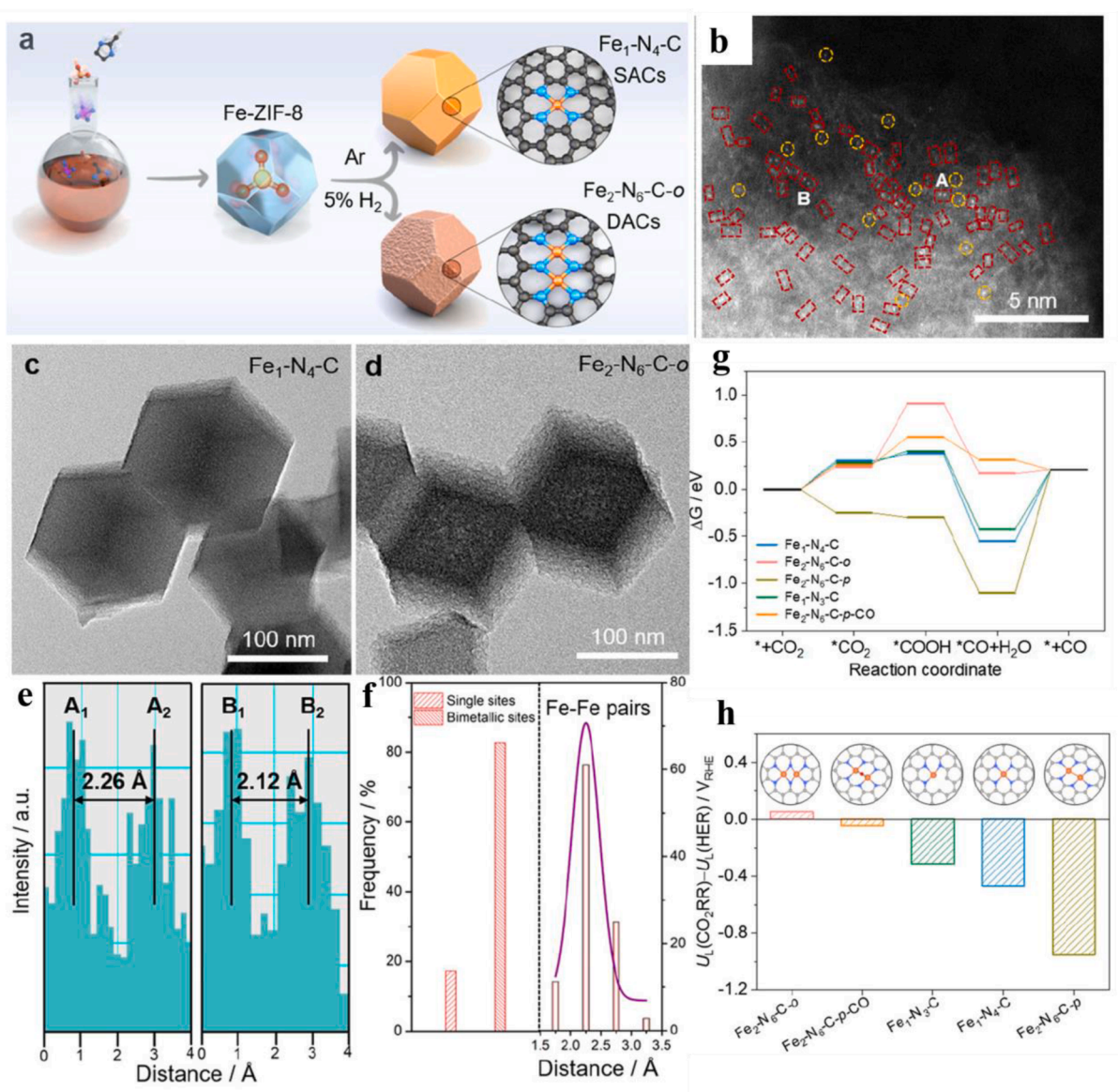
Fig. 16. (a) Schematic of the preparation process. (b) HAADF-STEM image (c) and (d) TEM image of Fe$_2$ − N$_6$ − C-o. (e) Intensity profiles obtained on the two sites in areas A and B in Fig. b. (f) Statistical study of the single and dual Fe sites and the Fe − Fe distance in Fig. b. (g) Free energy diagram of CO$_2$RR. (h) Difference in theoretical limiting potential for CO$_2$RR and HER. Reproduced with permission.[81] Copyright 2022, American Chemical Society.

indicating that different coordination environments will affect the valence states. In different Fe-N coordination environments, Fe_2-N_6-C-o diatomic electrocatalysts showed the best catalytic CO_2RR activity and stability and could achieve more than 80% FE_{CO} over a wide range of applied potentials, and turnover frequency as high as 26,637 h^{-1}. The DOS diagram showed that the d-band center moves down in Fe_2-N_6-C-o. Due to the 3d orbital coupling between the diatomic Fe, the orbital energy level decreases and the electron delocalization is caused. In addition, due to the interaction between the orbitals, the band gap between the antibonding and bonding states in Fe_2-N_6-C-o narrows down, which is beneficial to the desorption of *CO since co-adsorption at two sites provides additional active centers. Compared with different structures, the barrier in the RDS on Fe_2-N_6-C-o is the lowest, and the orthogonal bit structure has the highest selectivity for the CO_2RR (Fig. 16g-h). Thus, the synergistic effect between the unique orthogonal Fe_2-N_6 makes the catalyst have remarkable intrinsic activity, selectivity and durability.

By adjusting the coordination number of bimetal and nitrogen in DACs, the catalysts with different catalytic activities can be obtained. Besides the conventional coordination with six nitrogen atoms, M_1N_4-M_2N_3, M_1M_2-N_5, M_1M_2-N_4 and M_1M_2-N/O coordination structures can also be formed. He et al. synthesized Fe-Cu diatomic catalysts with N_4Fe-CuN_3 structure. In the synthesis process, the active site structure was precisely controlled by minimizing and ordering the spatial distance of metal precursors. Fe/Cu-N-C showed excellent selectivity in CO_2RR, and the FE_{CO} was more than 95% in a wide potential range (-0.4 - −1.1 V). At −1.1 V, the turnover frequency was as high as 5047 h^{-1}. Theoretical calculations revealed that the synergistic effect of N_4Fe-CuN_3 accelerates the charge transfer and effectively regulates the center position of d band, optimizing the formation energy of *COOH intermediate and the desorption energy of *CO [136]. Chen et al. constructed a diatomic IrCo-N-C catalyst with active site $IrCoN_5$ structure, which is an excellent bifunctional catalyst. In ORR, the $E_{1/2}$ was 0.911 V, while in OER, the η_{10} was 330 mV. Theoretical calculations showed that Ir changes the d orbital energy level of Co, making it rearrange in the direction of spin polarization, which is conducive to accepting oxygen electrons, forming strong Co-O, and speeding up the reaction kinetics [100]. Xing et al. successfully designed a configuration of a binuclear site catalyst (Co-N-C-10) with Co_2N_5 configuration using a bimetal-organic frame-self-regulation strategy. The catalytic activity is 12 times higher than that of traditional SAC with CoN_4 active site. According to the calculation and analysis of DFT, the pre-adsorbed OH at Co_2N_5 can promote the conversion of *OH intermediates into water. At U = 0.52 V, there is no thermodynamic barrier at the Co_2N_5(OH) site, implying that ORR can be spontaneous [82].

For ORR, when more ligands bond with Fe, the adsorption orbital of reactant O_2 will be reduced. In DACs, not only the energy level of the central metal affects the catalytic activity, but also the geometric configuration of the active site significantly affects the catalytic reaction. The geometrical configuration of the reactive site plays a key role in the oxygen adsorption position and O-O bond length. In general, oxygen is inclined to adsorb to the bridge-cis structure at diatomic sites, which favors the 4e⁻ ORR pathway, where O-O bond is weaker and more likely to break. Xing et al. constructed an Fe-Co diatomic central site model and introduced a proactive absorbed electron-absorbing OH ligand as an energy level regulator to controllably regulate the electronic structure and geometry of the active site, which is conducive to promoting the desorption of intermediates in ORR and weakening the O-O bonding ability. The charge density difference and Mulliken charge analysis displayed that the Fe electron density at $FeCoN_5$ site increased, and the DOS showed that the d band center of Fe in the double site shifted upward compared with the single site, both of which indicated that the ORR intermediates were absorbed more strongly at the dual-site. The adsorption free energy of *OH at $FeCoN_5$ site was −0.3774 eV (U = 0 V), indicating that $FeCoN_5$-OH site could be spontaneously formed during ORR. When OH is spontaneously adsorbed at the dual-

site, the electron density at the Fe site in $FeCoN_5$-OH decreases, suggesting that electrons are not easily lost at the $FeCoN_5$-OH site, and the electron occupation of the bond orbital in the lower energy state is more stable. The positive shift of the redox potential at the $FeCoN_5$-OH site resulted in an increase in ORR activity. In addition, the $FeCoN_5$ site in the plane can also spontaneously adsorb OH, which is conducive to the ORR. XAS spectroscopy further indicated the presence of the diatomic sites of $FeCoN_5$ (Fig. 17a-f). In situ XAS fitting results showed a decrease in the electron density of Fe at the double site (Fig. 17g-h). In addition, according to the moving direction of energy at different potentials in Fig. 17i-l, the average valence state of Fe site increased due to the axial connection of Fe with O/OH during ORR. By comparing the results of single-site and dual-site catalysts, Fe was oxidized more slowly on the $FeCoN_x$/C catalyst, which can provide more active sites for ORR, indicating that dual-site $FeCoN_x$ has a site-blocking effect. The experimental results showed that the $FeCoN_x$/C catalyst had excellent ORR activity with E_{onset} of 1.02 V and $E_{1/2}$ of 0.86 V, and good stability [121]. In addition to the N-coordination, metal atoms can also coordinate with oxygen to adjust the coordination environment. Zhang et al. designed a catalyst with Ni/Fe-N_2O_4 site (Ni/Fe-N/O-C), which showed excellent CO_2RR activity with TOF of 460 s^{-1} and more than 80% FE_{CO} in −1.4 - −1.7 V. The adjustment of the local environment and electronic structure of the active site reduced the energy barrier of *COOH formation [53].

4.3. Tuning the base environment of carbon-based materials

The creation of defect sites on the support plays an important role in trapping central metal atoms since the lattices of the support often inhibit the anchoring of adjacent metal atoms. It is of great significance to fabricate defective carbon-based diatomic catalysts by optimizing the structure of the support. Graphene has a high density of defects. The defects can not only activate electrochemical reactions, but also provide unique positions for anchoring metal atoms. Yao et al. reported a novel atomic Co-Pt carbon/nitrogen-based catalyst (A-CoPt-NC) using defects in the base plane during the synthesis process. XANES spectra showed that single-atom Co/Pt was coordinated with N/C. HAADF-STEM images showed that the metal ions were atomically distributed, but the distribution was uneven, and they were mainly distributed in the vacancy of graphite layer. Amorphous carbon is unstable and easily oxidized to form vacancy in the activation process. Due to lattice defects, the combined action of suspended carbon and nitrogen bond can capture single-atom Co and Pt (Fig. 18) [109]. The A-CoPt-NC catalyst showed high ORR activity and stability under alkaline conditions, and the activity was much higher than that of commercial Pt/C catalyst, with specific activity and mass activity 85 times and 267 times, respectively. Theoretical calculations showed that the (Co-Pt)@N8V4 structure has the lowest overpotential (0.30 V). The first protonation $O_2 \rightarrow OOH*$ step determines the initial potential. At equilibrium, the free energy changes the most, with a value of 0.3 eV. The trapped heteroatoms (Co and Pt) on N8V4 have strong binding forces with O. According to the state density analysis, the energy of Co 3d orbital is close to Fermi level in A-CoPt-NC, and the binding between Co 3d orbital and O is enhanced. In addition, according to the energy distribution diagram, the accumulation of strong electrons near Co atoms is due to the asymmetry between Co and Pt at the active site, which promotes the charge polarization around the active site. The accumulation of strong electrons around Co can accelerate the reduction of O_2 and accelerate the ORR kinetics. The A-CoPt-NC catalyst is a 4e⁻ pathway in the catalytic ORR, and it is easy to generate O* and OH* in the dissociative 4e⁻ pathway, instead of OOH*, because the O-O dissociation has an activation energy of 0.56 eV. The 4e⁻ pathway can occur on (Co-Pt)@N8V4 because of the existence of defects on the carbon base plane and the interaction between Co and Pt, which makes the d orbital move towards the Fermi level and the charge polarization around the active site, and changes the dissociation energy of O-O bond. Therefore, ORR is the 4e⁻ pathway on (Co-Pt)@N8V4. The
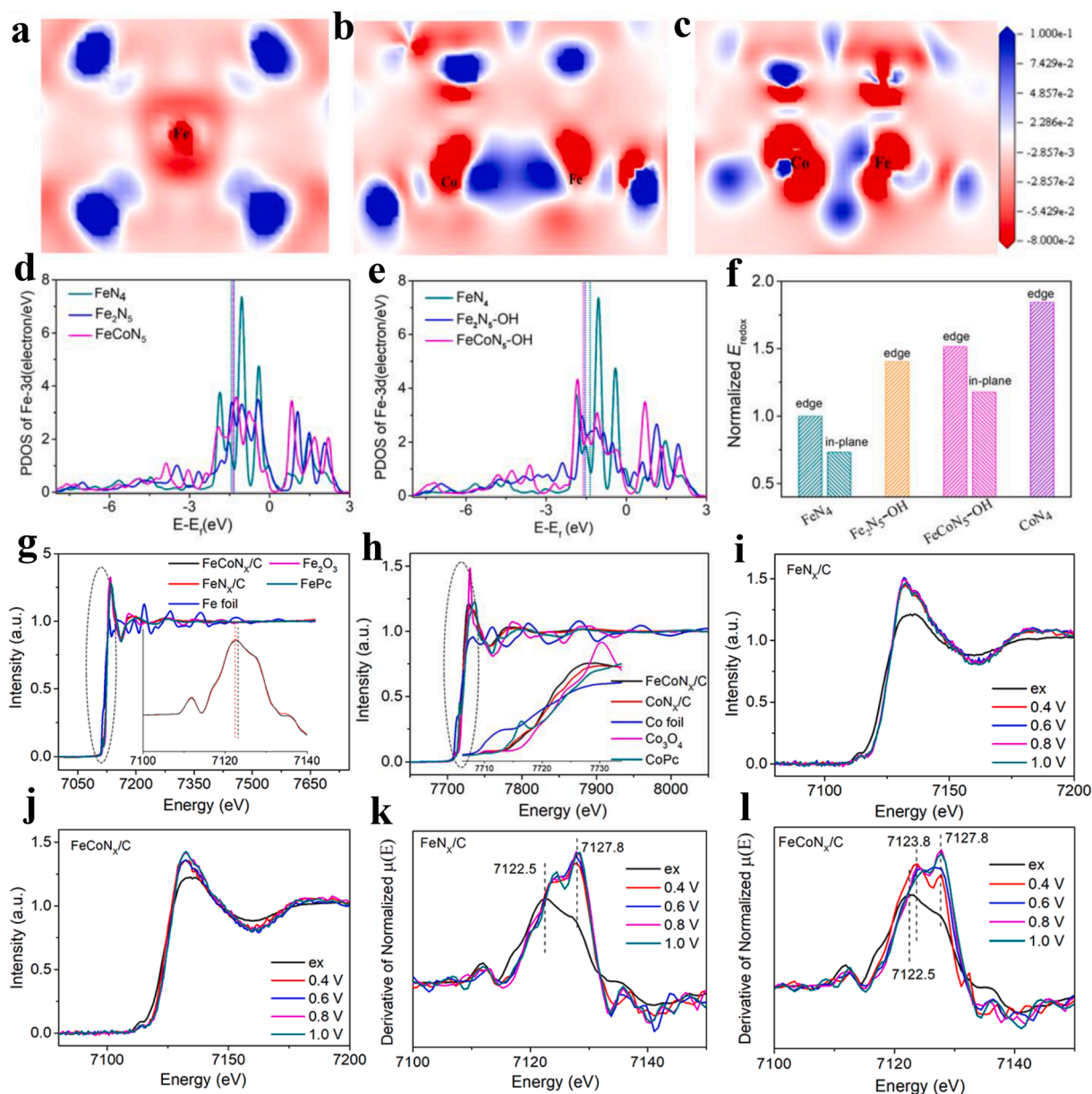
Fig. 17. (a) Calculated charge density differences for (a) FeN$_4$, (b) FeCoN$_5$, and (c) FeCoN$_5$-OH. Fe3d PDOS (d) before and (e) after absorption of OH*. (f) Calculated M(II/III) (M = Fe or Co) redox potential. Ex situ XANES spectra for the (g) Fe K-edge and (h) Co K-edge. Fe K-edge in situ XANES and the first-derivative of XANES spectra for (i, k) FeN$_x$/C and (j, l) FeCoN$_x$/C. Reproduced with permission.[121] Copyright 2019, American Chemical Society.

defect engineering of base modification and the adjustment of the co-ordination environment of metal atoms play an important role in the ORR. Fan et al. synthesized N-doped graphene (W$_1$Mo$_1$-NG) with O-coordination W-Mo heterodimer using controlled self-assembly and nitride techniques. In W$_1$Mo$_1$-NG, W and Mo are anchored to NG vacancy by bridging-O to form a W-O-Mo-O-C structure, which is very stable and well distributed. W$_1$Mo$_1$-NG catalysts showed high HER activity and stability under both acidic and basic conditions, which was comparable to Pt. Theoretical calculations showed that the W-O-Mo-O-C configuration can redistribute the electronic structure and provide an optimal electronic environment for HER. In addition, the W-O-Mo-O-C configuration has a Gibbs free energy close to 0 (0.065 eV) on an oxygen atom connected to Mo axially, which is lower than that of commercial Pt catalyst (0.10 eV). In addition, experimental results and theoretical calculations showed that the unique W-O-Mo-O-C configuration exhibited high HER activity at universal pH [51].

In addition, heteroatomic doping can be used to destroy the original

sp^2 carbon lattice of C to induce defects. Zhao et al. designed a three-dimensional dentate carbon catalyst with N and S co-doping of zinc and cobalt bimetals. The catalyst showed good ORR activity (E$_{1/2}$ = 0.893 V). Raman spectroscopy and theoretical calculations showed that the introduction of N and S causes many defects in the material, redistributing surface electrons and enhancing the interaction between the active site and the oxygen-containing intermediates. The O$_2$ dissociation energy adsorbed on the Zn-Co double site decreases, thus promoting the conversion from *OOH to *O [119].

5. Regulation strategies of carbon-based DACs

5.1. Improving stability

The stability of catalysts involves mechanical stability and reaction stability. Mechanical stability refers to the stability of the load on the working electrode during the catalytic process. To ensure the progress of
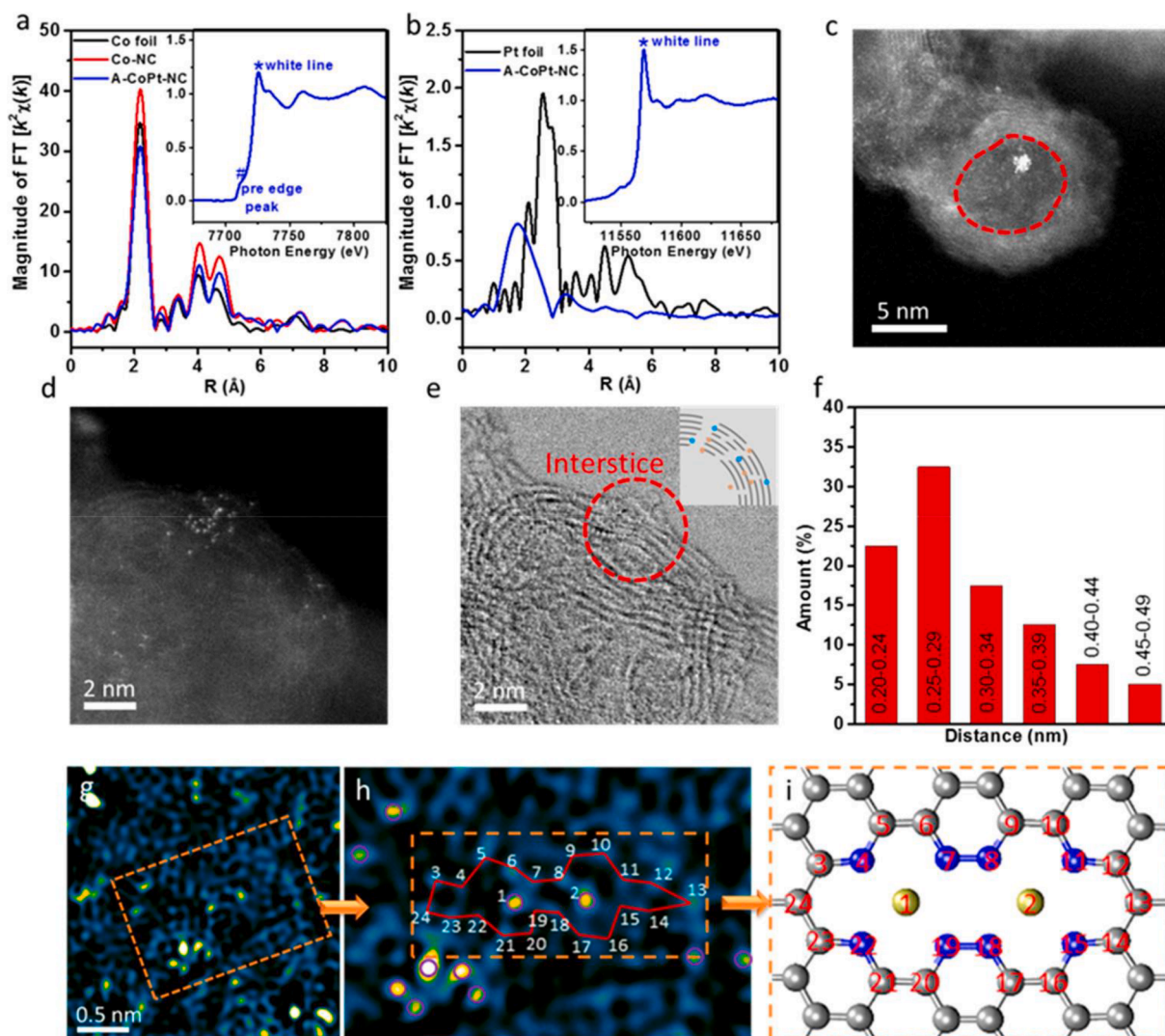
Fig. 18. (a, b) The k^2-weighted FT-EXAFS spectra. (c, d) Dark-field STEM images of the A-CoPt-NC. (e) Corresponding bright-field STEM image of (d) with the inset of the schematic diagram of the interstice zone. (f) Distribution of distances of adjacent metal atoms counted from 40 neighboring metal atom pairs. (g) HAADF image of A-CoPt-NC after fast Fourier transformation filtering. (h) Partially zoomed-in image of the area framed in (g). (i) Model of the configuration of the two metal atoms trapped in the defect, reconstructed from the observed atomic structure in (h). Reproduced with permission.[109] Copyright 2018, American Chemical Society.

the reaction, the catalyst needs a stable load on the working electrode. The commonly used working electrode is the glassy carbon electrode. In addition, the catalyst can be loaded, or in-situ synthesized on carbon sheet, carbon paper, nickel foam, copper foam and other substrates to reduce the mechanical fall off the catalyst and increase the mechanical stability. Reaction stability refers to the deactivation, corrosion, and irreversible structural transformation of active sites of the catalyst during the reaction process. Compared with SACs, the interaction between the metals and the metal and the support in DACs can reduce the migration of single atoms on the surface of the support and reduce the formation of clusters and nanoparticles. The stability of catalyst can be improved by selecting suitable bimetallic atoms and support to avoid deactivation during the reaction. Li et al. synthesized a nitrogen-doped porous carbon material (Fe, Co)/N-C with Fe-Co dual-center using a host–guest strategy. After long-term stability tests, the structure of Fe-Co dual-site remained unchanged, indicating that the dual-site Fe-Co has strong stability [112]. Chen et al. theoretically studied the catalytic CO_2RR performance of transition metal dimers ($M_2@C_2N$) loaded on C_2N and found that this type of catalyst has excellent catalytic activity and high stability due to the strong hybridization between the 3d orbital of the transition metal and the 2p orbital of N, which reduces the

diffusion of metal atoms on the support, avoids the aggregation of metal atoms, and improves the stability [84].

5.2. Increasing active sites

The number of effective metal active sites can be increased and the reaction kinetics can be accelerated by increasing the metal loading to obtain DACs with high uniform dispersion. At present, DACs are mainly synthesized through high temperature pyrolysis strategy, which cannot precisely control the anchoring sites of the metals. ALD can be used to precisely control the deposition process and obtain heteronuclear diatomic catalyst by depositing different metal atoms step by step. In addition, diatomic metal-embedded carbon supported catalysts can be obtained by packaging diatomic organometallic compounds into MOF cavities and then thermal decomposition. Yao et al. reported a Ni_2-site diatomic catalyst (Ni_2/NC) with uniform atomic accuracy by pyrolysis of $Ni_2(dppm)_2Cl_3$ binuclear clusters encapsulated by a MOF material, avoiding the aggregation of metal atoms, and effectively improving the metal load. The obtained Ni_2/NC showed excellent CO_2RR activity [57]. Xiong et al. obtained catalysts containing monatomic Fe_1, diatomic Fe_2 and triatomic Fe_3 clusters by using a spatial confined pyrolysis strategy

to precisely control the number of iron atoms in the obtained catalysts [78].

5.3. Improving the reactivity of dual-atom active sites

The reactivity of dual-atom active sites determines the thermodynamic and kinetic rates of catalytic reactions. There are synergistic, geometric, and electronic effects among adjacent metal atoms in DACs. The selection of appropriate metal atoms, coordination environment and carrier can effectively regulate the electron transfer of diatomic sites, the hybrid effect of d-d orbitals and d-p orbitals, and the spin coupling effect between them, to change the adsorption state and energy of substances in catalytic reactions, activate chemical bonds in catalytic reactions, reduce the reaction energy barrier, and optimize the reaction path. Xing et al. obtained a diatomic catalyst with asymmetric Co_2N_5 structure by precise control of the atomic scale structure of bimetallic organic skeleton, in which the Co-Co distance is 2.1–2.2 Å. The ORR activity on Co_2N_5 is 12 times that of CoN_4. Theoretical calculations showed that the OH adsorbed on the Co_2N_5 site can be used as the modified ligand to promote the conversion of *OH to H_2O. At 0.52 V, there is a thermodynamic barrier (0.115 eV) at CoN_4 site, which inhibits the spontaneous progress of ORR, while there is no thermodynamic barrier at Co_2N_5 site. This indicates that the interaction of dual-atom sites improves the intrinsic activity and effectively reduces the thermodynamic energy barrier during ORR process [82].

6. Conclusions and prospects

Carbon materials provide a large area of anchoring sites for DACs, which have been widely used in various catalytic reactions due to their high efficiency and high catalytic activity. DACs effectively overcome the disadvantages of low loading capacity and single active site of SACs, and DACs have higher loading capacity and more active centers of geometric configuration, which can provide adsorption sites such as top site and bridge site for reaction intermediates. The interaction between diatomic centers optimizes the thermodynamic energy barrier and kinetic velocity of catalytic reactions. It is hoped that the applications of atomic catalysts will be promoted to a new level. In this review, we systematically summarized the synthesis methods and characterization techniques of DACs, focused on the recent research progress of DACs in HER, OER, ORR, CO_2RR and NRR, and elaborated the structure–function relationships. In addition, efficient strategies to improve the catalytic activity of carbon-based DACs were proposed. Finally, the dilemma and future development direction of diatomic catalysts were analyzed.

Although carbon-based DACs have made great progress in the field of electrocatalysis, there are still problems to be solved. (i) It is still challenging for controllable synthesis of DACs. The uniformly distributed high-density active sites can significantly improve the catalytic activity. However, when the metal load is high, the agglomeration of metal atoms will inevitably occur in the synthesis process, and the uneven pores and defect sites on the support will affect the controllable synthesis of dual-atom sites, and the relationship between the structure and performance. At present, some researchers have adopted a space-confined domain pyrolysis strategy to synthesize DACs, which is applicable to partial carriers with cavities, but not to pore-free materials, e.g., two-dimensional materials. To reduce the migration of metal atoms during thermal decomposition, ultrafast heating and cooling techniques can be used to anchor bimetallic sites on the carrier in a controlled manner. To promote the application of DACs in energy storage and conversion, it is necessary to develop more convenient and rapid controllable synthesis strategies. (ii) It is feasible to design multiple active sites in a directional manner. Although DACs have more reactive intermediate-binding sites than SACs, there are still shortcomings in catalyzing bifunctional reactions, such as OER and ORR, which are the core reactions in rechargeable metal-air batteries. It will greatly promote the applications of DACs by regulating the coordination environment of metal active centers and substrate surface by combining theory and experiment. The development of multi-nuclear site synergistic catalysts will be a landmark design. (iii) The structure information of active sites can be obtained through HAADF-STEM and XAS, while the change of catalytic sites can be dynamically studied by in situ characterization techniques. The evolution of reactive intermediates in the reaction process plays a key role in understanding the nature of active centers. However, the real state of active centers is very complex, and the adsorption type and position of reactive intermediates will affect the change of electronic states. Therefore, static characterization alone is not enough, and in-situ characterization techniques should be further used to detect the dynamic changes of active sites in catalytic reactions, to better understand the complex mechanisms. Currently developed in-situ techniques mainly include in situ XAS, in situ infrared spectroscopy and in situ Raman spectroscopy, which can be used to investigate the relationship between the electronic structure and catalytic properties of diatomic active sites at the sub-nanometeric or atomic level. New in situ characterization techniques at the atomic level need to be developed in the future, which will pave the way for the study of "structure-activity relationships" of DACs in electrocatalytic reactions. (iv) In theory, except for some common transition metals and precious metals, other rarely used elements in the periodic table of elements also have the possibility in the fabrication of diatomic catalysts. However, it will take much time to prepare all possible diatomic catalysts in the experiment and to study their electrocatalytic performances. The establishment of a database of diatomic catalysts by digital simulation is convenient for guiding experiments more efficiently. In summary, carbon-based DACs have made great progress in the field of electrocatalysis, but there are still great challenges. With the development of various synthesis and characterization techniques, carbon-based DACs will become more efficient for electrocatalytic energy related applications.

Declaration of Competing Interest

The authors declare that they have no known competing financial interests or personal relationships that could have appeared to influence the work reported in this paper.

Data availability

Data will be made available on request.

Acknowledgments

References

[1] C.-C. Hou, H.-F. Wang, C. Li, Q. Xu, Energy Environ. Sci. 13 (2020) 1658–1693, https://doi.org/10.1039/C9EE04040D.

[2] J. Han, J. Guan, Nano Res. 16 (2023) 1913–1966, https://doi.org/10.1007/s12274-022-4874-7.

[3] J. Han, J. Guan, Chin. J. Catal. 47 (2023) 1–31, https://doi.org/10.1016/S1872-2067(22)64207-4.

[4] X. Liu, L. Liao, G. Xia, F. Yu, G. Zhang, M. Shu, H. Wang, J. Mater. Chem. A 10 (2022) 25047–25054, https://doi.org/10.1039/D2TA07135E.

[5] Y. Zhang, L. Tao, C. Xie, D. Wang, Y. Zou, R. Chen, Y. Wang, C. Jia, S. Wang, Adv. Mater. 32 (2020) 1905923, https://doi.org/10.1002/adma.201905923.

[6] Y. Li, S.L. Zhang, W. Cheng, Y. Chen, D. Luan, S. Gao, X.W. Lou, Adv. Mater. 34 (2022) 2105204, https://doi.org/10.1002/adma.202105204.

[7] Z.-F. Huang, S. Xi, J. Song, S. Dou, X. Li, Y. Du, C. Diao, Z.J. Xu, X. Wang, Nat. Commun. 12 (2021) 3992, https://doi.org/10.1038/s41467-021-24182-w.

[8] Q. Zhang, J. Guan, Adv. Funct. Mater. 30 (2020) 2000768, https://doi.org/10.1002/adfm.202000768.

[9] T. Tang, Y. Wang, J. Han, Q. Zhang, X. Bai, X. Niu, Z. Wang, J. Guan, Chin. J. Catal. 46 (2023) 48–55, https://doi.org/10.1016/S1872-2067(22)64189-5.

[10] T. Tang, Z. Wang, J. Guan, Acta Physico Chimica Sinica 39 (2022) 2208033, https://doi.org/10.3866/pku.Whxb202208033.

[11] L. Liao, G. Xia, Y. Wang, G. Ye, H. Wang, 121826, Appl. Catal., B 318 (2022), https://doi.org/10.1016/j.apcatb.2022.121826.

[12] L. Kong, M. Zhong, W. Shuang, Y. Xu, X.-H. Bu, Chem. Soc. Rev. 49 (2020) 2378–2407, https://doi.org/10.1039/C9CS00880B.

[13] Y. Guo, T. Park, J.W. Yi, J. Henzie, J. Kim, Z. Wang, B. Jiang, Y. Bando, Y. Sugahara, J. Tang, Y. Yamauchi, Adv. Mater. 31 (2019) 1807134, https://doi.org/10.1002/adma.201807134.

[14] W. Li, S. Xue, S. Watzele, S. Hou, J. Fichtner, A.L. Semrau, L. Zhou, A. Welle, A.S. Bandarenka, R.A. Fischer, Angew. Chem. Int. Ed. 59 (2020) 5837–5843, https://doi.org/10.1002/anie.201916507.

[15] J. Han, J. Guan, Chin. J. Catal. 44 (2023) 1–3, https://doi.org/10.1016/S1872-2067(22)64153-6.

[16] X. Bai, Z. Duan, B. Nan, L. Wang, T. Tang, J. Guan, Chin. J. Catal. 43 (2022) 2240–2248, https://doi.org/10.1016/S1872-2067(21)64033-0.

[17] F. Hu, L. Liao, B. Chi, H. Wang, Chem. Eng. J. 436 (2022), 135271, https://doi.org/10.1016/j.cej.2022.135271.

[18] L. Li, B. Huang, X. Tang, Y. Hong, W. Zhai, T. Hu, K. Yuan, Y. Chen, Adv. Funct. Mater. 31 (2021) 2103857, https://doi.org/10.1002/adfm.202103857.

[19] X. Bai, L. Wang, B. Nan, T. Tang, X. Niu, J. Guan, Nano Res. 15 (2022) 6019–6025, https://doi.org/10.1007/s12274-022-4293-7.

[20] T. Tang, Z. Wang, J. Guan, Adv. Funct. Mater. 32 (2022) 2111504, https://doi.org/10.1002/adfm.202111504.

[21] Y. Ouyang, L. Shi, X. Bai, Q. Li, J. Wang, Chem. Sci. 11 (2020) 1807–1813, https://doi.org/10.1039/c9sc05236d.

[22] X. Bai, J. Guan, Chin. J. Catal. 43 (2022) 2057–2090, https://doi.org/10.1016/S1872-2067(21)64030-5.

[23] T. Tang, Z. Wang, J. Guan, Chin. J. Catal. 43 (2022) 636–678, https://doi.org/10.1016/S1872-2067(21)63945-1.

[24] H. Jeong, S. Shin, H. Lee, ACS Nano 14 (2020) 14355–14374, https://doi.org/10.1021/acsnano.0c06610.

[25] L. Hong, X. Liu, B. Chi, G. Xia, H. Wang, J. Mater. Chem. A 11 (2023) 6321–6328, https://doi.org/10.1039/D2TA09831H.

[26] W.-H. Li, J. Yang, D. Wang, Angew. Chem. Int. Ed. 61 (2022), https://doi.org/10.1002/anie.202213318 e202213318.

[27] T. Tang, Z. Duan, D. Baimanov, X. Bai, X. Liu, L. Wang, Z. Wang, J. Guan, Nano Res. 16 (2023) 2218–2223, https://doi.org/10.1007/s12274-022-5001-3.

[28] L. Zhang, R. Si, H. Liu, N. Chen, Q. Wang, K. Adair, Z. Wang, J. Chen, Z. Song, J. Li, M.N. Banis, R. Li, T.-K. Sham, M. Gu, L.-M. Liu, G.A. Botton, X. Sun, Nat. Commun. 10 (2019) 4936, https://doi.org/10.1038/s41467-019-12887-y.

[29] X. Zheng, B. Li, Q. Wang, D. Wang, Y. Li, Nano Res. 15 (2022) 7806–7839, https://doi.org/10.1007/s12274-022-4429-9.

[30] H. Zhang, X. Jin, J.-M. Lee, X. Wang, ACS Nano 16 (2022) 17572–17592, https://doi.org/10.1021/acsnano.2c06827.

[31] J.P. Collman, P. Denisevich, Y. Konai, M. Marrocco, C. Koval, F.C. Anson, J. Am. Chem. Soc. 102 (1980) 6027–6036, https://doi.org/10.1021/ja00539a009.

[32] N.R. Sahraie, U.I. Kramm, J. Steinberg, Y. Zhang, A. Thomas, T. Reier, J.-P. Paraknowitsch, P. Strasser, Nat. Commun. 6 (2015) 8618, https://doi.org/10.1038/ncomms9618.

[33] Z. Lu, B. Wang, Y. Hu, W. Liu, Y. Zhao, R. Yang, Z. Li, J. Luo, B. Chi, Z. Jiang, M. Li, S. Mu, S. Liao, J. Zhang, X. Sun, Angew. Chem. Int. Ed. 58 (2019) 2622–2626, https://doi.org/10.1002/anie.201810175.

[34] Y. Song, B. Xu, T. Liao, J. Guo, Y. Wu, Z. Sun, Small 17 (2021) 2002240, https://doi.org/10.1002/smll.202002240.

[35] J. Su, S. Zhang, Q. Liu, G. Hu, L. Zhang, J. Mater. Chem. A 9 (2021) 5276–5295, https://doi.org/10.1039/D0TA12447H.

[36] Y. Lei, Y. Wang, Y. Liu, C. Song, Q. Li, D. Wang, Y. Li, Angew. Chem. Int. Ed. 59 (2020) 20794–20812, https://doi.org/10.1002/anie.201914647.

[37] J.A. Oke, T.-C. Jen, J. Mater. Res. Technol. 21 (2022) 2481–2514, https://doi.org/10.1016/j.jmrt.2022.10.064.

[38] L. Zhang, M.N. Banis, X. Sun, Natl. Sci. Rev. 5 (2018) 628–630, https://doi.org/10.1093/nsr/nwy054 %J.

[39] N. Cheng, X. Sun, Chin. J. Catal. 38 (2017) 1508–1514, https://doi.org/10.1016/S1872-2067(17)62903-6.

[40] H. Zhang, C.L. Marshall, Chin. J. Catal. 40 (2019) 1311–1323, https://doi.org/10.1016/S1872-2067(19)63321-8.

[41] J.A. Singh, N. Yang, S.F. Bent, Annu. Rev. Chem. Biomol. Eng. 8 (2017) 41–62, https://doi.org/10.1146/annurev-chembioeng-060816-101547.

[42] R.W. Johnson, A. Hultqvist, S.F. Bent, Mater. Today 17 (2014) 236–246, https://doi.org/10.1016/j.mattod.2014.04.026.

[43] N. Sobel, C. Hess, Angew. Chem. Int. Ed. 54 (2015) 15014–15021, https://doi.org/10.1002/anie.201503680.

[44] J. Fonseca, J. Lu, ACS Catal. 11 (2021) 7018–7059, https://doi.org/10.1021/acscatal.1c01200.

[45] L. Zou, Y.-S. Wei, C.-C. Hou, C. Li, Q. Xu, Small 17 (2021) 2004809, https://doi.org/10.1002/smll.202004809.

[46] L. Jiao, H.-L. Jiang, Chem 5 (2019) 786–804, https://doi.org/10.1016/j.chempr.2018.12.011.

[47] Z. Song, L. Zhang, K. Doyle-Davis, X. Fu, J.-L. Luo, X. Sun, Adv. Energy Mater. 10 (2020) 2001561, https://doi.org/10.1002/aenm.202001561.

[48] T. Tang, S. Li, J. Sun, Z. Wang, J. Guan, Nano Res. 15 (2022) 8714–8750, https://doi.org/10.1007/s12274-022-4575-0.

[49] J. Guan, X. Bai, T. Tang, Nano Res. 15 (2022) 818–837, https://doi.org/10.1007/s12274-021-3680-9.

[50] Y. Da, Z. Tian, R. Jiang, Y. Liu, X. Lian, S. Xi, Y. Shi, Y. Wang, H. Lu, B. Cui, J. Zhang, X. Han, W. Chen, W. Hu, Sci. China Mater. 66 (2023) 1389–1397, https://doi.org/10.1007/s40843-022-2249-9.

[51] Y. Yang, Y. Qian, H. Li, Z. Zhang, Y. Mu, D. Do, B. Zhou, J. Dong, W. Yan, Y. Qin, L. Fang, R. Feng, J. Zhou, P. Zhang, J. Dong, G. Yu, Y. Liu, X. Zhang, X. Fan, Sci. Adv. 6 (2020) eaba6586, https://doi.org/10.1126/sciadv.aba6586.

[52] Y. Chen, S. Qiao, Y. Tang, Y. Du, D. Zhang, W. Wang, H. Xie, C. Liu, J. Mater. Chem. A 10 (2022) 25307–25318, https://doi.org/10.1039/D2TA06091D.

[53] Q. Gong, Y. Wang, X. Ren, C. He, J. Liu, Q. Zhang, ChemSusChem 14 (2021) 4499–4506, https://doi.org/10.1002/cssc.202101302.

[54] X.-M. Liang, H.-J. Wang, C. Zhang, D.-C. Zhong, T.-B. Lu, 122073, Appl. Catal., B 322 (2023), https://doi.org/10.1016/j.apcatb.2022.122073.

[55] Y. Li, C. Chen, R. Cao, Z. Pan, H. He, K. Zhou, 118747, Appl. Catal., B 268 (2020), https://doi.org/10.1016/j.apcatb.2020.118747.

[56] N. Zhang, X. Zhang, Y. Kang, C. Ye, R. Jin, H. Yan, R. Lin, J. Yang, Q. Xu, Y. Wang, Q. Zhang, L. Gu, L. Liu, W. Song, J. Liu, D. Wang, Y. Li, Angew. Chem. Int. Ed. 60 (2021) 13388–13393, https://doi.org/10.1002/anie.202101559.

[57] T. Ding, X. Liu, Z. Tao, T. Liu, T. Chen, W. Zhang, X. Shen, D. Liu, S. Wang, B. Pang, D. Wu, L. Cao, L. Wang, T. Liu, Y. Li, H. Sheng, M. Zhu, T. Yao, J. Am. Chem. Soc. 143 (2021) 11317–11324, https://doi.org/10.1021/jacs.1c05754.

[58] F. Kong, M. Wang, Y. Huang, G. Meng, M. Chen, H. Tian, Y. Chen, C. Chen, Z. Chang, X. Cui, J. Shi, Energy Storage Mater. 54 (2023) 533–542, https://doi.org/10.1016/j.ensm.2022.11.003.

[59] K. Song, Y. Feng, X. Zhou, T. Qin, X. Zou, Y. Qi, Z. Chen, J. Rao, Z. Wang, N. Yue, X. Ge, W. Zhang, W. Zheng, 121591, Appl. Catal., B 316 (2022), https://doi.org/10.1016/j.apcatb.2022.121591.

[60] X. Zhou, K. Song, Y. Feng, C. Jiang, Z. Chen, Z. Wang, N. Yue, X. Ge, W. Zhang, W. Zheng, Nano Res. (2022) 1–9, https://doi.org/10.1007/s12274-022-5091-y.

[61] M. Liu, H. Chun, T.-C. Yang, S.J. Hong, C.-M. Yang, B. Han, L.Y.S. Lee, ACS Nano 16 (2022) 10657–10666, https://doi.org/10.1021/acsnano.2c02324.

[62] S. Huang, Z. Qiao, P. Sun, K. Qiao, K. Pei, L. Yang, H. Xu, S. Wang, Y. Huang, Y. Yan, D. Cao, 121770, Appl. Catal., B 317 (2022), https://doi.org/10.1016/j.apcatb.2022.121770.

[63] M.-J. Sun, Z.-W. Gong, J.-D. Yi, T. Zhang, X. Chen, R. Cao, Chem. Commun. 56 (2020) 8798–8801, https://doi.org/10.1039/D0CC03410J.

[64] Y.-X. Zhang, S. Zhang, H. Huang, X. Liu, B. Li, Y. Lee, X. Wang, Y. Bai, M. Sun, Y. Wu, S. Gong, X. Liu, Z. Zhuang, T. Tan, Z. Niu, J. Am. Chem. Soc. 145 (2023) 4819–4827, https://doi.org/10.1021/jacs.2c13886.

[65] S. Wei, A. Li, J.-C. Liu, Z. Li, W. Chen, Y. Gong, Q. Zhang, W.-C. Cheong, Y. Wang, L. Zheng, H. Xiao, C. Chen, D. Wang, Q. Peng, L. Gu, X. Han, J. Li, Y. Li, Nat. Nanotechnol. 13 (2018) 856–861, https://doi.org/10.1038/s41565-018-0197-9.

[66] J. Liu, ChemCatChem 3 (2011) 934–948, https://doi.org/10.1002/cctc.201100090.

[67] C. Genovese, M.E. Schuster, E.K. Gibson, D. Gianolio, V. Posligua, R. Grau-Crespo, G. Cibin, P.P. Wells, D. Garai, V. Solokha, S. Krick Calderon, J.J. Velasco-Velez, C. Ampelli, S. Perathoner, G. Held, G. Centi, R. Arrigo, Nat. Commun. 935 (9) (2018), https://doi.org/10.1038/s41467-018-03138-7.

[68] D. Yao, C. Tang, X. Zhi, B. Johannessen, A. Slattery, S. Chern, S.-Z. Qiao, Adv. Mater. 35 (2022) 2209386, https://doi.org/10.1002/adma.202209386.

[69] J.-D. Yi, X. Gao, H. Zhou, W. Chen, Y. Wu, Angew. Chem. Int. Ed. 61 (2022), https://doi.org/10.1002/anie.202212329.

[70] Z. Fan, R. Luo, Y. Zhang, B. Zhang, P. Zhai, Y. Zhang, C. Wang, J. Gao, W. Zhou, L. Sun, J. Hou, Angew. Chem. Int. Ed. 62 (2023), https://doi.org/10.1002/anie.202216326.

[71] J. Hao, Z. Zhuang, J. Hao, C. Wang, S. Lu, F. Duan, F. Xu, M. Du, H. Zhu, Adv. Energy Mater. 12 (2022) 2200579, https://doi.org/10.1002/aenm.202200579.

[72] D.-S. Bin, Y.-S. Xu, S.-J. Guo, Y.-G. Sun, A.-M. Cao, L.-J. Wan, Acc. Chem. Res. 54 (2021) 221–231, https://doi.org/10.1021/acs.accounts.0c00613.

[73] S. Zhang, Y. Wu, Y.-X. Zhang, Z. Niu, Sci. China: Chem. 64 (2021) 1908–1922, https://doi.org/10.1007/s11426-021-1106-9.

[74] Y. Lou, F. Jiang, W. Zhu, L. Wang, T. Yao, S. Wang, B. Yang, B. Yang, Y. Zhu, X. Liu, 120122, Appl. Catal., B 291 (2021), https://doi.org/10.1016/j.apcatb.2021.120122.

[75] H. Li, L. Wang, Y. Dai, Z. Pu, Z. Lao, Y. Chen, M. Wang, X. Zheng, J. Zhu, W. Zhang, R. Si, C. Ma, J. Zeng, Nat. Nanotechnol. 13 (2018) 411–417, https://doi.org/10.1038/s41565-018-0089-z.

[76] X. Lv, W. Wei, B. Huang, Y. Dai, T. Frauenheim, Nano Lett. 21 (2021) 1871–1878, https://doi.org/10.1021/acs.nanolett.0c05080.

[77] H. Yan, Y. Lin, H. Wu, W. Zhang, Z. Sun, H. Cheng, W. Liu, C. Wang, J. Li, X. Huang, T. Yao, J. Yang, S. Wei, J. Lu, Nat. Commun. 8 (2017) 1070, https://doi.org/10.1038/s41467-017-01259-z.

[78] W. Ye, S. Chen, Y. Lin, L. Yang, S. Chen, X. Zheng, Z. Qi, C. Wang, R. Long, M. Chen, J. Zhu, P. Gao, L. Song, J. Jiang, Y. Xiong, Chem 5 (2019) 2865–2878, https://doi.org/10.1016/j.chempr.2019.07.020.

[79] N. Zhang, T. Zhou, J. Ge, Y. Lin, Z. Du, C.A. Zhong, W. Wang, Q. Jiao, R. Yuan, Y. Tian, W. Chu, C. Wu, Y. Xie, Matter 3 (2020) 509–521, https://doi.org/10.1016/j.matt.2020.06.026.

[80] Y. Zhao, S. Zhou, J. Zhao, 101051, iScience 23 (2020), https://doi.org/10.1016/j.isci.2020.101051.

[81] Y. Wang, B.J. Park, V.K. Paidi, R. Huang, Y. Lee, K.-J. Noh, K.-S. Lee, J.W. Han, ACS Energy Lett. 7 (2022) 640–649, https://doi.org/10.1021/acsenergylett.1c02446.

[82] M. Xiao, H. Zhang, Y. Chen, J. Zhu, L. Gao, Z. Jin, J. Ge, Z. Jiang, S. Chen, C. Liu, W. Xing, Nano Energy 46 (2018) 396–403, https://doi.org/10.1016/j.nanoen.2018.02.025.

[83] H. Shen, Y. Li, Q. Sun, J. Phys. Chem. C 121 (2017) 3963–3969, https://doi.org/10.1021/acs.jpcc.7b00317.

[84] J. Zhao, J. Zhao, F. Li, Z. Chen, J. Phys. Chem. C 122 (2018) 19712–19721, https://doi.org/10.1021/acs.jpcc.8b06494.

[85] Z.W. Chen, J.-M. Yan, Q. Jiang, Small Methods 3 (2019) 1800291, https://doi.org/10.1002/smtd.201800291.

[86] X. Zhang, A. Chen, Z. Zhang, Z. Zhou, J. Mater. Chem. A 6 (2018) 18599–18604, https://doi.org/10.1039/C8TA07683A.

[87] X. Guo, J. Gu, S. Lin, S. Zhang, Z. Chen, S. Huang, J. Am. Chem. Soc. 142 (2020) 5709–5721, https://doi.org/10.1021/jacs.9b13349.

[88] L. Tian, Z. Li, X. Xu, C. Zhang, J. Mater. Chem. A 9 (2021) 13459–13470, https://doi.org/10.1039/D1TA01108A.

[89] B. Zhang, Y. Zheng, T. Ma, C. Yang, Y. Peng, Z. Zhou, M. Zhou, S. Li, Y. Wang, C. Cheng, Adv. Mater. 33 (2021) 2006042, https://doi.org/10.1002/adma.202006042.

[90] A.P. Tiwari, K. Kim, S. Jeon, Curr. Opin. Electrochem. 34 (2022), 100982, https://doi.org/10.1016/j.coelec.2022.100982.

[91] W. Li, C. Wang, X. Lu, Coord. Chem. Rev. 464 (2022), 214555, https://doi.org/10.1016/j.ccr.2022.214555.

[92] L. Sun, Q. Luo, Z. Dai, F. Ma, Coord. Chem. Rev. 444 (2021), 214049, https://doi.org/10.1016/j.ccr.2021.214049.

[93] X. Zeng, J. Shui, X. Liu, Q. Liu, Y. Li, J. Shang, L. Zheng, R. Yu, Adv. Energy Mater. 8 (2018) 1701345, https://doi.org/10.1002/aenm.201701345.

[94] X. Zhang, C. Shi, B. Chen, A.N. Kuhn, D. Ma, H. Yang, Curr. Opin. Chem. Eng. 20 (2018) 68–77, https://doi.org/10.1016/j.coche.2018.02.010.

[95] F. Zeng, C. Mebrahtu, L. Liao, A.K. Beine, R. Palkovits, J. Energy Chem. 69 (2022) 301–329, https://doi.org/10.1016/j.jechem.2022.01.025.

[96] K. Zhang, R. Zou, Small 17 (2021) 2100129, https://doi.org/10.1002/smll.202100129.

[97] M.S. Burke, M.G. Kast, L. Trotochaud, A.M. Smith, S.W. Boettcher, J. Am. Chem. Soc. 137 (2015) 3638–3648, https://doi.org/10.1021/jacs.5b00281.

[98] L. Bai, C.-S. Hsu, D.T.L. Alexander, H.M. Chen, X. Hu, J. Am. Chem. Soc. 141 (2019) 14190–14199, https://doi.org/10.1021/jacs.9b05268.

[99] F. Pan, T. Jin, W. Yang, H. Li, Y. Cao, J. Hu, X. Zhou, H. Liu, X. Duan, Chem Catalysis 1 (2021) 734–745, https://doi.org/10.1016/j.checat.2021.06.017.

[100] M. Xiao, J. Zhu, S. Li, G. Li, W. Liu, Y.-P. Deng, Z. Bai, L. Ma, M. Feng, T. Wu, D. Su, J. Lu, A. Yu, Z. Chen, ACS Catal. 11 (2021) 8837–8846, https://doi.org/10.1021/acscatal.1c02165.

[101] X. Zhu, D. Zhang, C.-J. Chen, Q. Zhang, R.-S. Liu, Z. Xia, L. Dai, R. Amal, X. Lu, Nano Energy 71 (2020), 104597, https://doi.org/10.1016/j.nanoen.2020.104597.

[102] X. Han, X. Ling, D. Yu, D. Xie, L. Li, S. Peng, C. Zhong, N. Zhao, Y. Deng, W. Hu, Adv. Mater. 31 (2019) 1905622, https://doi.org/10.1002/adma.201905622.

[103] Y. Wang, A. Kumar, M. Ma, Y. Jia, Y. Wang, Y. Zhang, G. Zhang, Z. Yan, Nano Res. 13 (2020) 1090–1099, https://doi.org/10.1007/s12274-020-2751-7.

[104] Y. Ma, W. Zang, A. Sumboja, L. Mao, X. Liu, M. Tan, S.J. Pennycook, Z. Kou, Z. Liu, X. Li, J. Wang, Sustain. Energ. Fuels 4 (2020) 1747–1753, https://doi.org/10.1039/C9SE01058K.

[105] J. Pan, Y.Y. Xu, H. Yang, Z. Dong, H. Liu, B.Y. Xia, Adv. Sci. 5 (2018) 1700691, https://doi.org/10.1002/advs.201700691.

[106] Y. Wang, Q. Li, L.-C. Zhang, Y. Wu, H. Chen, T. Li, M. Xu, S.-J. Bao, J. Mater. Chem. A 9 (2021) 7137–7142, https://doi.org/10.1039/D0TA09228B.

[107] S.K. Singh, K. Takeyasu, J. Nakamura, Adv. Mater. 31 (2019) 1804297, https://doi.org/10.1002/adma.201804297.

[108] J. Liu, M. Jiao, L. Lu, H.M. Barkholtz, Y. Li, Y. Wang, L. Jiang, Z. Wu, D.-J. Liu, L. Zhuang, C. Ma, J. Zeng, B. Zhang, D. Su, P. Song, W. Xing, W. Xu, Y. Wang, Z. Jiang, G. Sun, Nat. Commun. 8 (2017) 15938, https://doi.org/10.1038/ncomms15938.

[109] L. Zhang, J.M.T.A. Fischer, Y. Jia, X. Yan, W. Xu, X. Wang, J. Chen, D. Yang, H. Liu, L. Zhuang, M. Hankel, D.J. Searles, K. Huang, S. Feng, C.L. Brown, X. Yao, J. Am. Chem. Soc. 140 (2018) 10757–10763, https://doi.org/10.1021/jacs.8b04647.

[110] F. Kong, R. Si, N. Chen, Q. Wang, J. Li, G. Yin, M. Gu, J. Wang, L.-M. Liu, X. Sun, 120782, Appl. Catal., B 301 (2022), https://doi.org/10.1016/j.apcatb.2021.120782.

[111] A.J. Medford, A. Vojvodic, J.S. Hummelshøj, J. Voss, F. Abild-Pedersen, F. Studt, T. Bligaard, A. Nilsson, J.K. Nørskov, J. Catal. 328 (2015) 36–42, https://doi.org/10.1016/j.jcat.2014.12.033.

[112] J. Wang, Z. Huang, W. Liu, C. Chang, H. Tang, Z. Li, W. Chen, C. Jia, T. Yao, S. Wei, Y. Wu, Y. Li, J. Am. Chem. Soc. 139 (2017) 17281–17284, https://doi.org/10.1021/jacs.7b10385.

[113] J. Wang, W. Liu, G. Luo, Z. Li, C. Zhao, H. Zhang, M. Zhu, Q. Xu, X. Wang, C. Zhao, Y. Qu, Z. Yang, T. Yao, Y. Li, Y. Lin, Y. Wu, Y. Li, Energy Environ. Sci. 11 (2018) 3375–3379, https://doi.org/10.1039/C8EE02656D.

[114] K. Wang, J. Liu, Z. Tang, L. Li, Z. Wang, M. Zubair, F. Ciucci, L. Thomsen, J. Wright, N.M. Bedford, J. Mater. Chem. A 9 (2021) 13044–13055, https://doi.org/10.1039/D1TA02925H.

[115] G. Zhang, Y. Jia, C. Zhang, X. Xiong, K. Sun, R. Chen, W. Chen, Y. Kuang, L. Zheng, H. Tang, W. Liu, J. Liu, X. Sun, W.-F. Lin, H. Dai, Energy Environ. Sci. 12 (2019) 1317–1325, https://doi.org/10.1039/C9EE00162J.

[116] Y. Zhou, W. Yang, W. Utetiwabo, Y.-M. Lian, X. Yin, L. Zhou, P. Yu, R. Chen, S. Sun, J. Phys. Chem. Lett. 11 (2020) 1404–1410, https://doi.org/10.1021/acs.jpclett.9b03771.

[117] J. Xu, S. Lai, D. Qi, M. Hu, X. Peng, Y. Liu, W. Liu, G. Hu, H. Xu, F. Li, C. Li, J. He, L. Zhuo, J. Sun, Y. Qiu, S. Zhang, J. Luo, X. Liu, Nano Res. 14 (2021) 1374–1381, https://doi.org/10.1007/s12274-020-3186-x.

[118] Y. Wang, J. Wu, S. Tang, J. Yang, C. Ye, J. Chen, Y. Lei, D. Wang, Angew. Chem. Int. Ed. 62 (2023), https://doi.org/10.1002/anie.202219191.

[119] D. Liu, B. Wang, H. Li, S. Huang, M. Liu, J. Wang, Q. Wang, J. Zhang, Y. Zhao, Nano Energy 58 (2019) 277–283, https://doi.org/10.1016/j.nanoen.2019.01.011.

[120] J. Luangchaiyaporn, D. Wielend, D. Solonenko, H. Seelajaroen, J. Gasiorowski, M. Monecke, G. Salvan, D.R.T. Zahn, N.S. Sariciftci, P. Thamyongkit, Electrochim. Acta 367 (2021), 137506, https://doi.org/10.1016/j.electacta.2020.137506.

[121] M. Xiao, Y. Chen, J. Zhu, H. Zhang, X. Zhao, L. Gao, X. Wang, J. Zhao, J. Ge, Z. Jiang, S. Chen, C. Liu, W. Xing, J. Am. Chem. Soc. 141 (2019) 17763–17770, https://doi.org/10.1021/jacs.9b08362.

[122] L. Huang, W. Li, M. Zeng, G. He, P.R. Shearing, I.P. Parkin, D.J.L. Brett, Composites, Part B 220 (2021), 108986, https://doi.org/10.1016/j.compositesb.2021.108986.

[123] Y. Zhu, X. Yang, C. Peng, C. Priest, Y. Mei, G. Wu, Small 17 (2021) 2005148, https://doi.org/10.1002/smll.202005148.

[124] F. Lyu, W. Hua, H. Wu, H. Sun, Z. Deng, Y. Peng, Chin. J. Catal. 43 (2022) 1417–1432, https://doi.org/10.1016/S1872-2067(21)63980-3.

[125] S.-G. Han, D.-D. Ma, Q.-L. Zhu, Small Methods 5 (2021) 2100102, https://doi.org/10.1002/smtd.202100102.

[126] M. Wang, M. Li, Y. Liu, C. Zhang, Y. Pan, Nano Res. 15 (2022) 4925–4941, https://doi.org/10.1007/s12274-022-4175-z.

[127] S. Cao, S. Zhou, H. Chen, S. Wei, S. Liu, X. Lin, X. Chen, Z. Wang, W. Guo, X. Lu, Energy Environ. Mater. 6 (2021), https://doi.org/10.1002/eem2.12287.

[128] S. Zhu, K. Wan, H. Wang, L.-J. Guo, X. Shi, Nanotechnology 32 (2021), 385404, https://doi.org/10.1088/1361-6528/ac0be5.

[129] X. Wei, S. Wei, C. Cao, Y. Hu, S. Zhou, S. Liu, Z. Wang, X. Lu, Appl. Surf. Sci. 564 (2021), 150423, https://doi.org/10.1016/j.apsusc.2021.150423.

[130] D. Chen, Z. Chen, Z. Lu, J. Tang, X. Zhang, C.V. Singh, J. Mater. Chem. A 8 (2020) 21241–21254, https://doi.org/10.1039/D0TA05212D.

[131] H. Liu, Q. Huang, W. An, Y. Wang, Y. Men, S. Liu, J. Energy Chem. 61 (2021) 507–516, https://doi.org/10.1016/j.jechem.2021.02.007.

[132] L. Jiao, J. Zhu, Y. Zhang, W. Yang, S. Zhou, A. Li, C. Xie, X. Zheng, W. Zhou, S.-H. Yu, H.-L. Jiang, J. Am. Chem. Soc. 143 (2021) 19417–19424, https://doi.org/10.1021/jacs.1c08050.

[133] W. Ren, X. Tan, W. Yang, C. Jia, S. Xu, K. Wang, S.C. Smith, C. Zhao, Angew. Chem. Int. Ed. 58 (2019) 6972–6976, https://doi.org/10.1002/anie.201901575.

[134] H. Cheng, X. Wu, M. Feng, X. Li, G. Lei, Z. Fan, D. Pan, F. Cui, G. He, ACS Catal. 11 (2021) 12673–12681, https://doi.org/10.1021/acscatal.1c02319.

[135] Y. Li, B. Wei, M. Zhu, J. Chen, Q. Jiang, B. Yang, Y. Hou, L. Lei, Z. Li, R. Zhang, Y. Lu, Adv. Mater. 33 (2021) 2102212, https://doi.org/10.1002/adma.202102212.

[136] M. Feng, X. Wu, H. Cheng, Z. Fan, X. Li, F. Cui, S. Fan, Y. Dai, G. Lei, G. He, J. Mater. Chem. A 9 (2021) 23817–23827, https://doi.org/10.1039/D1TA02833B.

[137] Z. Geng, Y. Liu, X. Kong, P. Li, K. Li, Z. Liu, J. Du, M. Shu, R. Si, J. Zeng, Adv. Mater. 30 (2018) 1803498, https://doi.org/10.1002/adma.201803498.

[138] H. Tao, C. Choi, L.-X. Ding, Z. Jiang, Z. Han, M. Jia, Q. Fan, Y. Gao, H. Wang, A. W. Robertson, S. Hong, Y. Jung, S. Liu, Z. Sun, Chem 5 (2019) 204–214, https://doi.org/10.1016/j.chempr.2018.10.007.

[139] L. Han, X. Liu, J. Chen, R. Lin, H. Liu, F. Lü, S. Bak, Z. Liang, S. Zhao, E. Stavitski, J. Luo, R.R. Adzic, H.L. Xin, Angew. Chem. Int. Ed. 58 (2019) 2321–2325, https://doi.org/10.1002/anie.201811728.

[140] R. Zhang, L. Jiao, W. Yang, G. Wan, H.-L. Jiang, J. Mater. Chem. A 7 (2019) 26371–26377, https://doi.org/10.1039/c9ta10206j.

[141] F. Lü, S. Zhao, R. Guo, J. He, X. Peng, H. Bao, J. Fu, L. Han, G. Qi, J. Luo, X. Tang, X. Liu, Nano Energy 61 (2019) 420–427, https://doi.org/10.1016/j.nanoen.2019.04.092.

[142] M. Wang, S. Liu, T. Qian, J. Liu, J. Zhou, H. Ji, J. Xiong, J. Zhong, C. Yan, Nat. Commun. 10 (2019) 341, https://doi.org/10.1038/s41467-018-08120-x.

[143] Q. Qin, T. Heil, M. Antonietti, M. Oschatz, Small Methods 2 (2018) 1800202, https://doi.org/10.1002/smtd.201800202.

[144] W. Zang, T. Yang, H. Zou, S. Xi, H. Zhang, X. Liu, Z. Kou, Y. Du, Y.P. Feng, L. Shen, L. Duan, J. Wang, S.J. Pennycook, ACS Catal. 9 (2019) 10166–10173, https://doi.org/10.1021/acscatal.9b02944.

[145] Y. Chen, R. Guo, X. Peng, X. Wang, X. Liu, J. Ren, J. He, L. Zhuo, J. Sun, Y. Liu, Y. Wu, J. Luo, ACS Nano 14 (2020) 6938–6946, https://doi.org/10.1021/acsnano.0c01340.

[146] W. Tong, B. Huang, P. Wang, L. Li, Q. Shao, X. Huang, Angew. Chem. Int. Ed. 59 (2020) 2649–2653, https://doi.org/10.1002/anie.201913122.

[147] X. Cui, C. Tang, Q. Zhang, Adv. Energy Mater. 8 (2018) 1800369, https://doi.org/10.1002/aenm.201800369.

[148] Y. Li, Q. Zhang, C. Li, H.-N. Fan, W.-B. Luo, H.-K. Liu, S.-X. Dou, J. Mater. Chem. A 7 (2019) 22242–22247, https://doi.org/10.1039/C9TA07845B.

[149] L. Zhang, G. Fan, W. Xu, M. Yu, L. Wang, Z. Yan, F. Cheng, Chem. Commun. 56 (2020) (1960) 11957–111951, https://doi.org/10.1039/D0CC04843G.

[150] S. Wang, L. Shi, X. Bai, Q. Li, C. Ling, J. Wang, A.C.S. Cent, Sci. 6 (2020) 1762–1771, https://doi.org/10.1021/acscentsci.0c00552.

[151] C.N. Sun, Z.L. Wang, X.-Y. Lang, Z. Wen, Q. Jiang, ChemSusChem 14 (2021) 4593–4600, https://doi.org/10.1002/cssc.202101507.

[152] T. He, A.R. Puente Santiago, A. Du, J. Catal. 388 (2020) 77–83, https://doi.org/10.1016/j.jcat.2020.05.009.

[153] D. Ma, Z. Zeng, L. Liu, Y. Jia, J. Energy Chem. 54 (2021) 501–509, https://doi.org/10.1016/j.jechem.2020.06.032.

[154] D. Ma, Y. Wang, L. Liu, Y. Jia, Phys. Chem. Chem. Phys. 23 (2021) 4018–4029, https://doi.org/10.1039/D0CP04843G.

[155] D. Ma, Z. Zeng, L. Liu, X. Huang, Y. Jia, J. Phys. Chem. C 123 (2019) 19066–19076, https://doi.org/10.1021/acs.jpcc.9b05250.

[156] F. He, Z. Wang, S. Wei, J. Zhao, Appl. Surf. Sci. 506 (2020), 144943, https://doi.org/10.1016/j.apsusc.2019.144943.

[157] H. Li, Z. Zhao, Q. Cai, L. Yin, J. Zhao, J. Mater. Chem. A 8 (2020) 4533–4543, https://doi.org/10.1039/C9TA13599E.

[158] R. Hu, Y. Li, Q. Zeng, F. Wang, J. Shang, ChemSusChem 13 (2020) 3636–3644, https://doi.org/10.1002/cssc.202000964.

[159] Y. Qian, Y. Liu, Y. Zhao, X. Zhang, G. Yu, EcoMat 2 (2020), https://doi.org/10.1002/eom2.12014.

[160] Z. Zhang, X. Huang, H. Xu, A.C.S. Appl, Mater. Interfaces 13 (2021) 43632–43640, https://doi.org/10.1021/acsami.1c11585.